

Antenna Array Processing: Autocalibration and Fast High-Resolution Methods for Automotive Radar

Vom Fachbereich 18
Elektrotechnik und Informationstechnik
der Technischen Universität Darmstadt
zur Erlangung der Würde eines
Doktor-Ingenieurs (Dr.-Ing.)
genehmigte Dissertation

von
Dipl.-Ing. Philipp Heidenreich
geboren am 27.12.1980 in Rüsselsheim

Referent:	Prof. Dr.-Ing. Abdelhak M. Zoubir
Korreferent:	Prof. Dr.-Ing. Bin Yang
Tag der Einreichung:	29.02.2012
Tag der mündlichen Prüfung:	06.06.2012

Danksagung

Die vorliegende Arbeit entstand im Rahmen meiner Tätigkeit als wissenschaftlicher Mitarbeiter am Fachgebiet Signalverarbeitung des Instituts für Nachrichtentechnik der Technischen Universität Darmstadt. An dieser Stelle gilt mein Dank allen, die das Entstehen der Arbeit direkt oder indirekt ermöglicht haben.

Besonders möchte ich mich bei Prof. Dr.-Ing. Abdelhak Zoubir für die wissenschaftliche Betreuung der Arbeit bedanken. Seine stete Bereitschaft zur Diskussion und die Förderung von Publikationen und Projekten, sowie das Ermöglichen von Konferenzen, haben maßgeblich zum Gelingen der Arbeit beigetragen. Des Weiteren bedanke ich mich bei Prof. Dr.-Ing Bin Yang für die freundliche Übernahme des Korreferats und sein Interesse an meiner Arbeit. Ebenso gilt mein Dank Prof. Dr.-Ing. Klaus Hofmann, Prof. Dr.-Ing. Rolf Jakoby und Prof. Dr.-Ing. habil. Tran Quoc Khanh für ihre Mitwirkung in der Prüfungskommission.

Für die Kooperation und Förderung meiner Promotion möchte ich mich bei der A.D.C. GmbH der Continental AG bedanken. Mein besonderer Dank gilt Florian Engels, Dr. Alexander Kaps, Dr. Peter Seydel und Dr. Markus Wintermantel, und später auch Markus Friebertshäuser und David Stenmanns, für die zahlreichen fachlichen Gespräche und wertvollen Anregungen, die Unterstützung bei der Aufnahme von Radarmessungen, sowie die Gastfreundlichkeit bei meinen regelmäßigen Besuchen in Lindau.

Ich bedanke mich bei Prof. em. Dr-Ing. Eberhard Hänsler und Prof. Dr.-Ing. Gerhard Schmidt für die vielen netten Mittagessen während meiner Anfangsphase. Mein Dank gilt auch Hauke Fath und Renate Koschella für die freundliche Unterstützung.

Vor allem möchte ich mich bei allen Kollegen am Fachgebiet Signalverarbeitung für die angenehme Arbeitsatmosphäre bedanken, die meine Zeit als wissenschaftlicher Mitarbeiter sehr bereichert hat. Ich bedanke mich insbesondere bei meinen Zimmerkollegen Michael Leigsnering und Dr. Marco Moebus, sowie bei Dr. Christian Debes, Nevine Demitri, Dr. Raquel Fandos, Dr. Ulrich Hammes, Stefan Leier, Michael Muma und Dr. Eric Wolstynski, die in der einen oder anderen Weise zum Gelingen meiner Arbeit beigetragen haben. Des Weiteren bedanke ich mich bei Dr. Holger Maune, Dr. Pouyan Parvazi, Dr. Marius Pesavento und Dr. Michael Rübsamen für die Zusammenarbeit und hilfreichen Anregungen.

Allen Studenten, deren Studien- und Diplomarbeiten ich betreut habe, danke ich für ihr Interesse an meiner Arbeit und die fachlichen Gespräche.

Schließlich möchte ich mich auch bei meiner Familie und meiner Frau Tanja für die Unterstützung und den Rückhalt bedanken.

Rüsselsheim, 27.06.2012

Kurzfassung

In dieser Dissertation werden fortgeschrittene Verfahren der Signalverarbeitung für Antennengruppen behandelt. Dabei wird das Problem der Autokalibrierung betrachtet und eine neue Technik für eine zweidimensionale Sensorgruppe vorgeschlagen. Zudem werden praktisch realisierbare Verfahren der hochauflösenden Winkelschätzung und Detektion für Kfz-Radar entwickelt.

Um die Leistungsfähigkeit von Verfahren der Winkelschätzung zu gewährleisten ist ein genaues Modell der Sensorgruppe notwendig. Wenn die Sensorumgebung zeitvariant ist kann dies nur mit Autokalibrierung gewährleistet werden. Das fundamentale Problem der Autokalibrierung einer unbekannter Phasenantwort wird für die gleichförmig rechteckige Sensorgruppe behandelt. Für den Fall einer Quelle wird ein einfaches und robustes Verfahren der kleinsten Quadrate für die gemeinsame Winkelschätzung und Phasenkalibrierung entwickelt. Ein Identifikationsproblem wird erkannt und eine geeignete Lösung vorgeschlagen. In Simulationen wird gezeigt, dass die Genauigkeit der Winkelschätzung und Phasenkalibrierung nahe an der approximativen Cramér-Rao Schranke ist. Darüber hinaus wird das entwickelte Verfahren für den Fall mit mehreren Quellen erweitert. Simulationsergebnisse belegen, dass der vorgeschlagene Algorithmus die Auflösungsfähigkeit erhöht wenn Phasenfehler vorhanden sind.

In Kfz-Anwendungen ist eine genaue Bestimmung der Fahrzeugumgebung für moderne Fahrerassistenzsysteme wie Abstandsregeltempomat oder Notbremsassistent erforderlich. Für eine Zielortung bezüglich Distanz, Relativgeschwindigkeit und Winkel wird ein gepulstes Radar-System mit Empfangssensorgruppe verwendet. Nach der Puls-Kompression und Doppler-Verarbeitung erhält man Verarbeitungszellen gemäß Distanz und Relativgeschwindigkeit mit jeweils einem Beobachtungsvektor. In den meisten Fällen können mehrere Ziele durch ihre Distanz und/oder Relativgeschwindigkeit unterschieden werden, so dass jede Verarbeitungszelle höchstens ein Ziel beinhaltet. Es gibt jedoch Situationen, in denen mehrere Ziele in einer Verarbeitungszelle überlagert sind. In den oben genannten Anwendungen kann dies bei horizontaler Mehrwegeausbreitung mit einer nahen Leitplanke geschehen, wobei ein Geisterziel resultiert. Wenn die Ausbreitungspfade nicht mit konventionellen Methoden getrennt werden können, wird das beobachtete Fahrzeug falsch lokalisiert und hochauflösende Verfahren der Winkelschätzung sind notwendig. Das potenzielle Zwei-Ziel-Modell in dem schwierigen Fall mit einem einzelnen Beobachtungsvektor wird betrachtet. Dabei wird ein optimaler verallgemeinerter Likelihood-Quotienten-Test angewendet, der den rechenintensiven Maximum-Likelihood (ML) Schätzer für zwei Ziele beinhaltet. Dieses Verfahren liefert gute Ergebnisse für echte Messdaten aus Experimenten mit einem und

zwei Winkelreflektoren. Um Echtzeitfähigkeit zu erreichen, muss der Rechenaufwand allerdings erheblich reduziert werden. Daher werden geeignete Kriterien vorgeschlagen, um die Verarbeitungszellen auszuwählen, für die der ML Schätzer für zwei Ziele notwendig ist. Wenn die Ziele im räumlichen Spektrum aufgelöst sind, sind die resultierenden Winkelschätzer in der Regel mit einem Bias behaftet. Für diesen Fall wird eine Bias-Korrektur mit geringer Rechenkomplexität entwickelt. Ergebnisse von Simulationen und echten Daten zeigen, dass das entwickelte Verfahren ähnliche Ergebnisse wie der optimale Schätzer liefert, wobei der Rechenaufwand signifikant reduziert ist. Wenn dagegen das räumliche Spektrum nur eine Leistungsspitze zeigt, sind entweder zwei Ziele nicht aufgelöst oder es ist nur ein Ziel vorhanden. Für diesen Fall wird ein Test entwickelt, um zu entscheiden, ob das Modell mit einem einzelnen Ziel angemessen ist. Folglich wird der ML Schätzer für zwei Ziele nur dann berechnet, wenn das Ein-Ziel-Modell abgelehnt wird. Diese Strategie kann den Rechenaufwand erheblich reduzieren, sofern Situationen mit mehr als einem Ziel pro Verarbeitungszelle unwahrscheinlich sind. Schließlich wird eine praktisch realisierbare Implementierung des ML Schätzers für zwei Ziele vorgeschlagen. Diese basiert auf einer vereinfachten Zielfunktion und einem begrenzten Suchbereich. Die erforderlichen Projektionsoperatoren sind datenunabhängig und können im Voraus berechnet werden, was einen Austausch von Rechenaufwand und Speicherbedarf ermöglicht. Das entwickelte Verfahren liefert gleichwertige Simulationsergebnisse wie ausgewählte rechengünstige Algorithmen, wobei es eine unkomplizierte und nicht-iterative Implementierung ermöglicht. Der praktische Wert des vorgeschlagenen Verfahrens wird mit echten Messdaten aus einer typischen Situation aus der Kfz-Radaranwendung belegt.

Abstract

In this thesis, advanced techniques for antenna array processing are addressed. The problem of autocalibration is considered and a novel method for a two-dimensional array is developed. Moreover, practicable methods for high-resolution direction-of-arrival (DOA) estimation and detection in automotive radar are proposed.

A precise model of the array response is required to maintain the performance of DOA estimation. When the sensor environment is time-varying, this can only be achieved with autocalibration. The fundamental problem of autocalibration of an unknown phase response for uniform rectangular arrays is considered. For the case with a single source, a simple and robust least squares algorithm for joint two-dimensional DOA estimation and phase calibration is developed. An identification problem is determined and a suitable constraint is proposed. Simulation results show that the performance of the proposed estimator is close to the approximate CRB for both DOA estimation and phase calibration. The proposed algorithm for phase autocalibration is extended for the case with multiple sources. Simulation results demonstrate that the proposed algorithm enhances the resolution performance in the presence of phase errors.

In automotive applications, modern driver assistance systems such as adaptive cruise control (ACC) or collision avoidance require an accurate description of the environment of a vehicle. For target localization in terms of range, relative velocity and DOA, a pulsed radar system with an array of receive antennas is considered. After pulse compression and Doppler processing, one obtains processing cells according to range and relative velocity, each represented by a single snapshot. In most cases, multiple targets can be distinguished by their range and/or relative velocity, so that each processing cell only contains a single target. However, there are situations, in which several targets are superposed in a processing cell. In the mentioned applications, this can occur in the presence of horizontal multipath with a close guardrail, which results in a ghost target. If the propagation paths cannot be resolved by conventional methods, this results in a false localization of the observed vehicle and high-resolution DOA estimation becomes necessary. The potential two-target model in the difficult case with a single snapshot is considered. An optimal generalized likelihood ratio test is applied, which involves the calculation of the computationally intensive maximum likelihood (ML) estimate of two targets. This approach provides good results with real data from experiments with a single and two corner reflectors. To achieve real-time capability, the computational cost has to be reduced substantially. Therefore, suitable criteria are presented to pre-select the processing cells, for which the ML estimator of two targets is necessary. When the targets are resolved in the spatial spectrum, the resulting DOA

estimates are generally biased. For this case, a strategy for bias correction with low computational complexity is proposed. Results obtained from simulations and real data show that the performance of the developed algorithm is close to ML estimation, but at a significantly lower computational cost. When the spatial spectrum only shows a single significant peak, either a single target is present or two targets are unresolved. For this case, a computationally simple test is developed to decide whether the model with a single target is appropriate. Consequently, ML estimation of two targets is carried out only if the single-target model is rejected. This strategy is able to substantially save computations, when situations with more than one target per processing cell are unlikely. Finally, a practicable implementation for the ML estimator of two targets is developed, which is based on a simplified objective function and a delimited search range. The required projection operators are data-independent and can be pre-calculated off-line, which enables a trade-off between computational complexity and storage space. In simulations, the developed approach is shown to perform similarly to selected computationally efficient algorithms, but allows a straightforward and non-iterative implementation. The practical value of the proposed approach is further demonstrated using real data from a typical situation of an ACC application.

Contents

1	Introduction	1
1.1	Motivation	1
1.2	Original contributions	2
1.3	Thesis overview	5
2	Array processing	7
2.1	General array signal model	7
2.1.1	Ideal data model	7
2.1.2	Real array modeling and calibration	10
2.2	Direction-of-arrival estimation	11
2.2.1	Beamformer	12
2.2.2	Nonlinear least squares	12
2.2.3	Subspace methods	13
2.2.4	Comparison	14
2.3	Source detection	15
2.4	Phase autocalibration for uniform rectangular arrays	16
2.4.1	Perturbed data model	18
2.4.1.1	Ambiguity	19
2.4.1.2	Cramér-Rao bound	20
2.4.2	Proposed autocalibration algorithm	21
2.4.3	Extension for multiple sources	25
2.4.4	Simulation results	26
2.4.4.1	Variance of the phase	27
2.4.4.2	Effect of SNR and array size	27
2.4.4.3	Comparison with BF matching and MAP-NSF	28
2.4.4.4	Resolution	30
2.4.5	Conclusion	33
2.A	Appendix	34
2.A.1	Statistical properties of the sample covariance matrix	34
2.A.2	MAP-NSF	36
3	Automotive radar	39
3.1	Background	39
3.2	Radar system	40
3.2.1	Radar measurement model	41
3.2.2	Radar pre-processing	44
3.2.3	Array processing problem: potential two-target case	46

3.3	Optimal single-snapshot array processing	48
3.3.1	Parameter estimation	49
3.3.1.1	Maximum likelihood	49
3.3.1.2	Accuracy and resolution	50
3.3.2	Detection with generalized likelihood ratio test	52
3.3.3	Experimental data example	53
3.4	Discussion	56
3.A	Appendix	58
3.A.1	Interpolation of maximum likelihood objective function	58
3.A.2	Interpolation of beamformer spectrum	58
4	Array processing for automotive radar with reduced complexity	61
4.1	Preliminaries	61
4.1.1	Beamformer for two targets	62
4.1.2	Beamformer resolution criterion	64
4.2	Proposed array processing	65
4.3	Bias correction for DOA estimation of two resolved targets	66
4.3.1	Proposed approach	67
4.3.1.1	Noise-free beamformer spectrum	67
4.3.1.2	Algorithm for bias correction	70
4.3.2	RELAX for two targets	71
4.3.3	Simulation results	72
4.3.4	Experimental data example	74
4.3.5	Conclusion	74
4.4	Multiple target detection	75
4.4.1	Proposed test statistic	76
4.4.1.1	Approximate distribution	76
4.4.1.2	Practical threshold setting	77
4.4.2	Simulation results	79
4.4.3	Experimental data example	80
4.4.4	Conclusion	81
5	Fast maximum likelihood DOA estimation of two targets	83
5.1	Background	83
5.2	Preliminaries	84
5.2.1	Direct objective function calculation	85
5.2.2	Global search	86
5.3	Proposed approach	87
5.3.1	Simplified objective function calculation	87
5.3.1.1	Unitary transformation	88

5.3.1.2	Single-snapshot alternative	90
5.3.1.3	Comparison	90
5.3.2	Delimited search range	91
5.3.2.1	Circular shift	91
5.3.2.2	Midpoint estimation	92
5.3.3	Example	93
5.4	Simulation results	94
5.4.1	Midpoint estimation	95
5.4.2	Angular separation	95
5.4.3	Effect of step size	96
5.4.4	Comparison with selected algorithms	97
5.5	Experimental data example	100
5.6	Conclusion	102
5.A	Appendix	104
5.A.1	IQML	104
5.A.2	Unitary ESPRIT	105
5.A.3	Beamspace maximum likelihood	107
6	Conclusions and outlook	109
6.1	Conclusions	109
6.2	Outlook	110
	List of Acronyms	113
	List of Symbols	115
	Bibliography	121
	Curriculum vitae	129

Chapter 1

Introduction

In this thesis, we consider advanced techniques for antenna array processing. In particular, we develop a novel autocalibration method for a two-dimensional array and propose practicable methods for high-resolution direction-of-arrival (DOA) estimation and detection for automotive radar. The introduction is structured as follows. In Section 1.1, we provide the motivation for this work. The original contributions are named in Section 1.2, in which also the publications, produced during the period of doctoral candidacy, are listed. Finally, an overview of the thesis is given in Section 1.3.

1.1 Motivation

In the following, we motivate the advanced techniques for antenna array processing, developed in this work. In a general framework, multiple sensors simultaneously measure a spatial field at several locations. The measurements are analyzed to obtain information about the sources, such as the DOA, the source waveform, etc. Array processing plays an important role in many application areas such as radar, sonar, wireless communications, radio astronomy, or medical diagnosis [JD93, KV96, God97, vT02]. Moreover, in many modern radar systems, antenna arrays represent an essential component [Hay07, RSH10].

Numerous methods for DOA estimation and imaging have been developed in array processing [vT02]. In the presence of model errors, high-resolution methods are known to degrade in performance [SK92, SK93, Fri90], and array calibration becomes necessary. In some applications, calibration measurements are difficult to obtain and/or the sensor environment is time-varying, so that the remaining model errors have to be corrected without calibration measurements. The challenging task of joint calibration and estimation task is referred to as autocalibration. In this thesis, we develop a simple and robust phase autocalibration technique for a two-dimensional array.

An increasing amount of advanced signal processing algorithms is used in various automotive applications [HBTA11], such as modern driver assistance systems [WHW09] or in-car communication systems [WLO⁺11]. An interesting concept for future automotive safety systems is to replace costly sensors with software algorithms [Gus09]. In

another example, the bootstrap is applied to determine the optimal locations of vibration sensors for knock detection of combustion engines [ZB95, ZI07]. In the following, we consider driver assistance systems, and typical applications such as adaptive cruise control (ACC) or collision avoidance. Driver assistance systems can use various sensors to determine the environment of the car. From an identified traffic situation, the driver assistance system regulates the behavior of the car, instructs the driver, or warns the driver in dangerous situations [Win10]. Often these systems use radar sensors, which work reliably even in bad weather conditions, and can provide accurate measurements of the distance, or range, and the radial relative velocity of multiple targets. To also measure the lateral position of a target, an array of antennas in horizontal direction with digital beamforming can be applied. For the described collision avoidance or ACC application, it is essential to accurately estimate the lateral position, and to be able to resolve multiple closely spaced targets. For array systems with limited aperture, this can be achieved with high-resolution processing. Generally, these methods are considered as computationally intensive and numerically complex, so that real-time implementation becomes a challenging task. In this thesis, we develop practicable methods for high-resolution DOA estimation and detection for automotive radar.

1.2 Original contributions

In the following, we summarize the original contributions in this thesis. First, we consider the problem of two-dimensional DOA estimation using a uniform rectangular array (URA) in the presence of phase errors.

- Phase autocalibration for URA geometries: We propose a simple and robust least squares (LS) algorithm for joint two-dimensional DOA estimation and phase calibration with a URA and a single source. The problem of rotational ambiguity between DOA and phase error parameters is studied and a suitable constraint is proposed. An approximate Cramér-Rao bound (CRB) and an analytical expression for the mean squared error performance of the proposed estimator is presented. Furthermore, we extend the proposed algorithm for phase autocalibration to the case with multiple sources.

Second, we consider the problem of high-resolution DOA estimation and detection of one or two targets with a single snapshot, which is practically relevant in automotive radar. We describe an optimal approach, based on maximum likelihood (ML) estimation and a generalized likelihood ratio test (GLRT), and present results with real data

in controlled experiments with one and two corner reflectors. Since this approach is computationally intensive and can become intractable in real-time, we develop a practicable approach with reduced complexity. The following novel techniques are part of the proposed processing chain.

- Bias correction for DOA estimation of two resolved targets: When the two targets are resolved in the beamformer (BF) spectrum, the resulting DOA estimates are generally biased due to leakage. For this case, we propose a strategy for bias correction with low computational complexity, which is based on the analysis of the noise-free BF spectrum and local approximations.
- Multiple target detection: When the BF spectrum shows only a single significant peak, either a single target is present or multiple targets are unresolved. For this case, we develop a computationally simple test to decide whether the model with a single target is appropriate. Consequently, the more complicated high-resolution DOA estimation of multiple targets is carried out only if the single-target model is rejected. This strategy can substantially save computations, when situations with more than one target per processing cell are unlikely.
- Fast ML DOA estimation of two targets: A practicable implementation of the ML estimator of two targets is developed, based on a simplified calculation of the objective function and a delimited search range. The required projection operators are data-independent and can be pre-calculated off-line, which enables a trade-off between computational complexity and storage space. The developed approach allows a straightforward and non-iterative implementation.

The following publications have been produced during the period of doctoral candidacy.

Book chapter

- P. Heidenreich and A. Zoubir, “Computational aspects of DOA estimation of two targets with applications to automotive radar,” in *Smart Mobile In-Vehicle Systems – Next Generation Advancements*. Springer, in preparation.

Internationally refereed journal articles

- P. Heidenreich, A. Zoubir, and M. RübSamen, “Joint 2-D DOA estimation and phase calibration for uniform rectangular arrays,” *IEEE Transactions on Signal Processing*, accepted.

- P. Heidenreich and A. Zoubir, “Fast maximum likelihood direction-of-arrival estimation in the two-target case with applications to automotive radar,” *Signal Processing*, in preparation.
- P. Heidenreich, L. Cirillo, and A. Zoubir, “Morphological image processing for FM source detection and localization,” *Signal Processing*, vol. 89, no. 6, pp. 1070–1080, 2009.

Internationally refereed conference papers

- P. Heidenreich and A. Zoubir, “Computationally simple DOA estimation of two resolved targets with a single snapshot,” *IEEE Int. Conf. on Acoustics, Speech and Sig. Proc. (ICASSP)*, Kyoto, Japan, March 2012.
- P. Heidenreich and A. Zoubir, “Computational aspects of maximum likelihood DOA estimation of two targets with applications to automotive radar,” *Proc. of the 5th Biennial Workshop on DSP for In-Vehicle Systems*, Kiel, Germany, September 2011 (won Best Student Paper Award).
- P. Heidenreich and A. Zoubir, “Gain and phase autocalibration for uniform rectangular arrays,” *IEEE Int. Conf. on Acoustics, Speech and Sig. Proc. (ICASSP)*, Prague, Czech Republic, May 2011.
- P. Heidenreich, D. Stenmanns, and A. Zoubir, “Computationally simple criteria for detecting a multi-target scenario in automotive radar array processing,” *European Sig. Proc. Conf. (EUSIPCO)*, Aalborg, Denmark, August 2010.
- Z. Lu, P. Heidenreich, and A. Zoubir, “Objective quality assessment of speech enhancement algorithms using bootstrap-based multiple hypotheses tests,” *IEEE Int. Conf. on Acoustics, Speech and Sig. Proc. (ICASSP)*, Dallas, USA, March 2010.
- W. Sharif, P. Heidenreich, and A. Zoubir, “Robust direction-of-arrival estimation for FM sources in the presence of impulsive noise,” *IEEE Int. Conf. on Acoustics, Speech and Sig. Proc. (ICASSP)*, Dallas, USA, March 2010.
- P. Heidenreich and A. Zoubir, “High-resolution direction finding of coherent sources in the presence of model errors using alternating projections,” *IEEE Workshop on Statistical Sig. Proc. (SSP)*, Cardiff, UK, September 2009.
- P. Heidenreich and A. Zoubir, “Goodness measure of speech reconstruction using the Bootstrap,” *Int. Symposium on Wireless Pervasive Computing (ISWPC)*, Santorini, Greece, May 2008.

- P. Heidenreich, L. Cirillo, and A. Zoubir, “Direction finding of nonstationary signals using spatial time-frequency distributions and morphological image processing,” *IEEE Int. Conf. on Acoustics, Speech and Sig. Proc. (ICASSP)*, Honolulu, USA, April 2007.

Filed patent applications

- M. Wintermantel, P. Heidenreich, and A. Zoubir (ContiTemic microelectronic GmbH and Technische Universität Darmstadt, Applicants), “Vereinfachte Berechnung zur hochauflösenden Winkelschätzung von mehreren Zielen mit Radarsystem für Kraftfahrzeuge,” Patent Application DE 10 2012/105 582.3.
- P. Heidenreich, F. Engels, and A. Zoubir (ContiTemic microelectronic GmbH and Technische Universität Darmstadt, Applicants), “Verfahren zur Winkelschätzung von Umgebungsobjekten mit einem Radarsystem insbesondere in einem Kraftfahrzeug,” Patent Application DE 10 2012/101 942.8.

1.3 Thesis overview

In this section, we provide an overview of this thesis. The structure is shown graphically in Figure 1.1. The gray boxes represent chapters and sections, which provide a review of state-of-the-art and introduce the context of the considered problems. The remaining chapters and sections contain original contributions.

In Chapter 2, we introduce the fundamentals of array processing which are necessary to understand the work in the following chapters. This includes the general array signal model and common methods for DOA estimation and detection. The novel phase autocalibration technique for the URA geometry is presented in Section 2.4. In Chapter 3, we consider the problem of high-resolution array processing in automotive radar for modern driver assistance systems. We provide a description of a typical automotive radar system, the measurement model and a possible pre-processing. Subsequently, we introduce the considered array processing problem of DOA estimation and detection of potentially two targets with a single snapshot. We describe an optimal approach, based on ML estimation and a GLRT, and present results with real data in controlled experiments with one and two corner reflectors. Since the described optimal approach is computationally intensive and intractable in real-time, we consider a practicable approach with reduced complexity in Chapter 4. The general idea is to pre-select

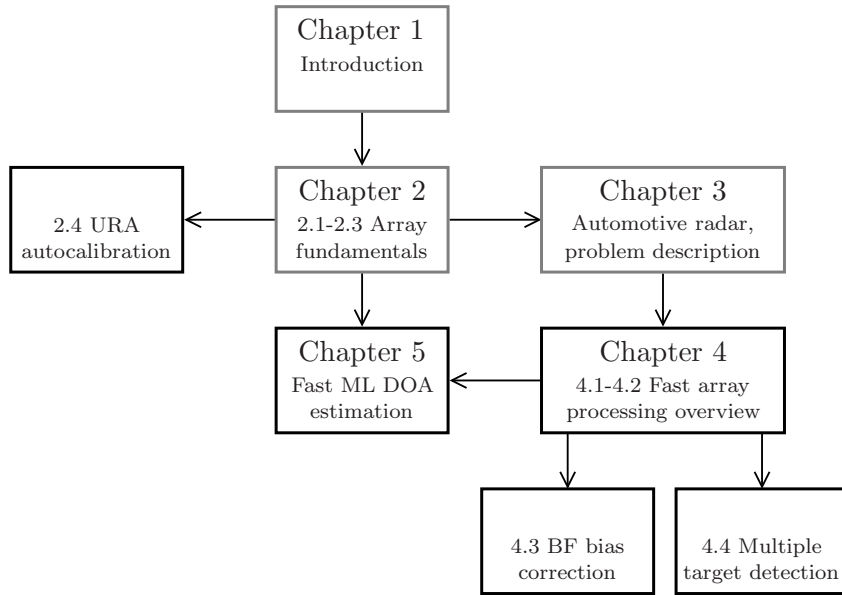


Figure 1.1. The structure of the thesis, gray boxes represent review and introductory parts, the remaining parts contain original contributions.

the cases, in which only a single target is present or two targets are well separated. Thus, the computationally intensive ML estimation of two targets is carried out only if its high-resolution performance is required. When two targets are resolved in the BF spectrum, the resulting DOA estimates are generally biased due to leakage. For this case, we propose a strategy for bias correction with low computational complexity in Section 4.3. When the BF spectrum shows only a single significant peak, either a single target is present or two targets are unresolved. For this case, in Section 4.4, we present a test with low computational complexity to decide whether the model with a single target is appropriate. The performance of the developed approaches is analyzed in simulations and with real data. In Chapter 5, we aim at further reducing complexity and develop a practicable implementation of the ML estimator of two targets. We address computational aspects of the required optimization of the two-dimensional ML objective function, and propose a simplified calculation of the objective function and a delimited search range. The performance of the developed implementation is analyzed in simulations, and compared with selected computationally efficient algorithms. Also, we present results with real data from a typical situation of an ACC application. Finally, conclusions are drawn in Chapter 6, and an outlook to possible future work is provided.

Chapter 2

Array processing

In this chapter, we introduce the fundamentals of array processing which are necessary to understand the work in the following chapters. The general array signal model, along with a common problem formulation and a brief outline on calibration, is provided in Section 2.1. Fundamental methods for DOA estimation are described in Section 2.2, and an outline on source detection is given in Section 2.3. In practical array processing, there can be model errors due to a time-varying sensor environment, and the DOA estimation performance may degrade significantly. For this case, we present a novel phase autocalibration technique for the URA geometry in Section 2.4.

2.1 General array signal model

2.1.1 Ideal data model

Consider an array of M isotropic sensors at positions \mathbf{p}_m , $m = 1, \dots, M$. Also consider a point source, located in the far-field of the array, at azimuth and elevation angle ϕ and θ , respectively. The source emits signal $s(t)e^{j2\pi f_c t}$ where $s(t)$ is the baseband signal at a reference sensor, and f_c is the carrier frequency. In the radar context, the reflected waveform at an ideal scatterer can be seen as being emitted from a point source. The corresponding geometry in a three-dimensional coordinate system is depicted in Figure 2.1 for the case with two antennas and a single source. In the far-field case, the wavefronts are planar at the array and can be described with the wavenumber vector [vT02]

$$\mathbf{k} = - \underbrace{\frac{2\pi}{\lambda}}_{\kappa} \begin{bmatrix} \sin(\theta) \sin(\phi) \\ \sin(\theta) \cos(\phi) \\ \cos(\theta) \end{bmatrix} \quad (2.1)$$

where λ is the wavelength. The received signals at the elements of the array are delayed versions of the emitted signal and can be collected into snapshot vector $\mathbf{x}_c(t) \in \mathbb{C}^{M \times 1}$ with elements

$$[\mathbf{x}_c]_m = s(t - \tau_m) e^{j2\pi f_c (t - \tau_m)}, \quad m = 1, \dots, M$$

where

$$\tau_m = \frac{1}{2\pi f_c} \mathbf{k}^T \mathbf{p}_m$$

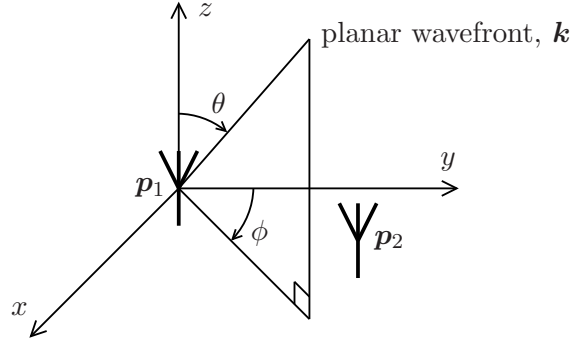


Figure 2.1. Three-dimensional coordinate system: planar wavefront from a far-field point source is impinging from spatial angles ϕ and θ with wavenumber \mathbf{k} on an array of antennas at positions \mathbf{p}_1 and \mathbf{p}_2 .

is the delay at sensor element m . Without loss of generality, the first sensor element can be taken as a reference such that we have $\tau_1 = 0$. When the bandwidth of $s(t)$ is significantly smaller than f_c divided by the array aperture, i.e. the largest extension of the array, it is common to approximate $s(t - \tau_m) \approx s(t)$. This is referred to as narrowband case, and assumed in the sequel. After demodulation with a known carrier frequency, we obtain the array output vector of received baseband signals, as

$$\mathbf{x}(t) = e^{-2\pi f_c t} \mathbf{x}_c(t) = s(t) \mathbf{a}(\phi, \theta) \quad (2.2)$$

where $\mathbf{a}(\phi, \theta)$ is the ideal array response, or steering vector, with elements

$$[\mathbf{a}(\phi, \theta)]_m = e^{-j\mathbf{k}^T \mathbf{p}_m}, \quad m = 1, \dots, M. \quad (2.3)$$

Note that (2.3) holds for arbitrary array geometries. Often in practical applications, the array geometry has a regular structure. Popular and well-known classes of arrays are the URA for azimuth and elevation DOA estimation, and the uniform linear array (ULA) for one-dimensional DOA estimation. Figure 2.2 shows the geometry of a URA with $M = M_x M_y$ antennas in the x/y -plane, where M_x and M_y are the number of elements in x - and y -direction, respectively, and d_x and d_y are the corresponding element spacings. Using electrical angles

$$\begin{aligned} \psi_x &= \kappa d_x \sin(\theta) \sin(\phi) \\ \psi_y &= \kappa d_y \sin(\theta) \cos(\phi) \end{aligned}$$

where κ is defined in (2.1), the ideal steering vector of a URA is given by

$$\mathbf{a}(\phi, \theta) = \mathbf{a}(\psi_x, \psi_y) = \mathbf{a}_y(\psi_y) \otimes \mathbf{a}_x(\psi_x) \quad (2.4)$$

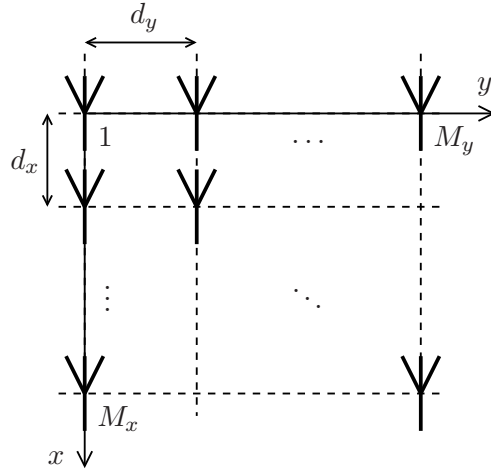


Figure 2.2. Geometry of a URA with $M = M_x M_y$ antennas in the x/y -plane. A ULA in x -direction is obtained for $M_y = 1$.

where \otimes denotes the Kronecker product, and

$$\begin{aligned}\mathbf{a}_x(\psi_x) &= [1, e^{j\psi_x}, \dots, e^{j(M_x-1)\psi_x}]^T \\ \mathbf{a}_y(\psi_y) &= [1, e^{j\psi_y}, \dots, e^{j(M_y-1)\psi_y}]^T.\end{aligned}\quad (2.5)$$

A ULA in x -direction can be obtained by setting $M_y = 1$. The ULA is a natural choice for applications in which one is only interested in one angle, e.g. the azimuth angle of objects in the x/y -plane, i.e. with $\theta = \pi/2$. Using electrical angle $\psi_x = \kappa d_x \sin(\phi)$, the ideal steering vector of a ULA is given by

$$\mathbf{a}(\phi) = \mathbf{a}(\psi_x) = \mathbf{a}_x(\psi_x) \quad (2.6)$$

where $\mathbf{a}_x(\psi_x)$ is defined in (2.5). We note that the regular structure of the described linear array geometries can be exploited for efficient implementations of array processing methods.

In digital signal processing applications, we assume that the demodulated array output vector in (2.2) is sampled at time instances t_i , $i = 1, \dots, N$. The obtained snapshots are denoted by $\mathbf{x}(i) = \mathbf{x}(t_i)$ for notational convenience. The general array signal model for a superposition of D sources in noise then reads

$$\mathbf{x}(i) = \sum_{k=1}^D s_k(i) \mathbf{a}(\phi_k, \theta_k) + \mathbf{e}(i) = \mathbf{A}(\boldsymbol{\phi}, \boldsymbol{\theta}) \mathbf{s}(i) + \mathbf{e}(i), \quad i = 1, \dots, N \quad (2.7)$$

where

$$\mathbf{A}(\boldsymbol{\phi}, \boldsymbol{\theta}) = [\mathbf{a}(\phi_1, \theta_1), \dots, \mathbf{a}(\phi_D, \theta_D)]$$

is the steering matrix, the azimuth and elevation angles of the D sources are contained in vectors $\boldsymbol{\phi}$ and $\boldsymbol{\theta}$, respectively, the source waveforms are contained in vector $\mathbf{s}(i)$, and $\mathbf{e}(i)$ is an additive noise term. The noise represents components in the actual array output, which are not well modeled by the relation in (2.2), such as external diffuse noise sources and thermal noise in the receiving hardware. Therefore, it appears reasonable to model the noise as a random process. Here, $\mathbf{e}(i)$ is assumed to be temporally and spatially white, circular complex, with zero mean and covariance matrix $\sigma^2 \mathbf{I}_M$, where \mathbf{I}_M denotes an identity matrix of dimension M . Depending on the application context, the source waveforms can be considered unknown deterministic or also modeled as random processes. In the latter case, when $\mathbf{s}(i)$ is assumed to be independent from $\mathbf{e}(i)$, temporally white, circular complex, with zero mean and positive definite covariance matrix \mathbf{P} , the spatial covariance matrix, corresponding to model (2.7), is given by

$$\mathbf{R} = \text{E}\{\mathbf{x}(i)\mathbf{x}(i)^H\} = \mathbf{A}(\boldsymbol{\phi}, \boldsymbol{\theta})\mathbf{P}\mathbf{A}(\boldsymbol{\phi}, \boldsymbol{\theta})^H + \sigma^2 \mathbf{I}_M \quad (2.8)$$

where $\text{E}\{\cdot\}$ denotes the expectation operator. \mathbf{R} can be estimated from the data using the sample covariance matrix

$$\hat{\mathbf{R}} = \frac{1}{N} \sum_{i=1}^N \mathbf{x}(i)\mathbf{x}(i)^H. \quad (2.9)$$

When the array response in (2.3) is known perfectly, the array processing task can be posed as follows: given snapshots $\mathbf{x}(i)$, $i = 1, \dots, N$ from model (2.7), decide on the number of sources D , and estimate parameters $\boldsymbol{\phi}$ and $\boldsymbol{\theta}$. This is commonly referred to as source detection and DOA estimation, respectively. Depending on the application context, one may also estimate $\mathbf{s}(i)$.

In practice, however, the array response may only be known imperfectly due to model errors. Since several studies have shown that high-resolution methods for DOA estimation are generally very sensitive to model errors [SK92, SK93, Fri90], we proceed by briefly describing possible imperfections of the array response.

2.1.2 Real array modeling and calibration

In practice, a sensor array implicates several systematic errors:

- The positions of sensor elements may deviate from the nominal ones. Moreover, the sensors may not be isotropic, but have a directional characteristic, which may be known only imperfectly.

- Mutual coupling may occur, i.e. the sensors do not only receive the direct field from the source, but also re-radiated energy from neighboring sensors [Sva99].
- Gain and phase errors may occur due to an imperfect receiving hardware.

A common model for the real array response, which summarizes various imperfections, is given by [NS96]

$$\tilde{\mathbf{a}}(\phi, \theta) = \mathbf{\Gamma} \mathbf{C} \mathbf{a}(\phi, \theta, \mathbf{\Delta}) \quad (2.10)$$

where $\mathbf{\Gamma}$ is a diagonal matrix containing the gain and phase error parameters, \mathbf{C} is a symmetric mutual coupling matrix, and $\mathbf{a}(\phi, \theta, \mathbf{\Delta})$ represents the ideal array response from (2.3) with position errors, which are contained in $\mathbf{\Delta}$.

A number of off-line calibration techniques have been developed to acquire an accurate model of the real array response. Such techniques involve the measurement of the array response for a finite set of known directions. Subsequently, the measured data is fitted to a presumed model. A maximum likelihood approach according to the model in (2.10) is considered in [NS96], whereas [LLV06] proposes a non-parametric approach based on local polynomial approximation. An experimental study is described in [PK91]. For a detailed overview of calibration methods, we refer to [TF09, Ch. 3].

The resulting model of the array response after calibration may still deviate from its true value due to unmodeled effects or a time-varying sensor environment. Therefore, multiple autocalibration techniques, which do not require off-line calibration measurements, have been proposed to mitigate the effect of remaining errors in the array response. A novel method for autocalibration of the unknown phase response of a URA is presented in Section 2.4.

2.2 Direction-of-arrival estimation

For the estimation problem, we assume that the number of sources is known. An outline on source detection is provided in Section 2.3. Similar to [TF09, Ch. 3], we proceed by briefly describing the principles of the conventional BF, nonlinear LS, and the popular MUSIC algorithm. We note that all described methods require a perfectly known array response, but can be used with an arbitrary array geometry. For convenience, we consider the estimation of azimuth angle ϕ only, although it is theoretically possible to estimate both azimuth and elevation angles.

2.2.1 Beamformer

An intuitive approach to DOA estimation is to coherently combine all sensor outputs using a spatial matched filter $\mathbf{a}(\phi)^H \mathbf{x}(i)$, matched to hypothetical angle ϕ , and to measure the resulting power. The field of view is scanned, and the DOA estimates are determined by the locations of the significant peaks of the spatial power spectrum, or BF spectrum,

$$P_{\text{BF}}(\phi) = \frac{1}{MN} \sum_{i=1}^N |\mathbf{a}(\phi)^H \mathbf{x}(i)|^2 \quad (2.11)$$

For the ULA, when using electrical angle ψ_x , the array response is given in (2.6). In this case, the inner vector product in (2.11) corresponds to a spatial Fourier transform, and can be calculated efficiently using a fast Fourier transform (FFT), e.g. [CT65]. Thus, the BF spectrum is the spatial equivalent of the periodogram [Sch98], averaged over N realizations [SM97]. DOA estimation with the BF is computationally simple, because only a one-dimensional spectral search is required. However, drawbacks are the limited resolution and dynamic range. In particular, for the ULA, the BF is unable to resolve sources, which are separated by less than the Rayleigh beamwidth (BW), which is defined by half the distance between the first zeros around the mainlobe of the beampattern [vT02], and is given by

$$\text{BW}_{\psi} = \frac{2\pi}{M}. \quad (2.12)$$

Note that this resolution limit only depends on the array aperture and is irrespective of the SNR. Moreover, weak sources may be masked by the sidelobes of stronger sources. To reduce the sidelobe level (SLL), windowing can be applied, at the cost of a reduced resolution.

2.2.2 Nonlinear least squares

Also an intuitive approach to parameter estimation is LS. Given model (2.7), the aim is to find unknown parameters ϕ and $\mathbf{s}(i)$, $i = 1, \dots, N$, which best match the observed array output in a LS sense, i.e. which minimize

$$\frac{1}{N} \sum_{i=1}^N \|\mathbf{x}(i) - \mathbf{A}(\phi)\mathbf{s}(i)\|^2 \quad (2.13)$$

where $\|\cdot\|$ denotes the Euclidian norm. Since ϕ enters nonlinearly into the above LS cost function, this approach is termed nonlinear LS. We note that if $\mathbf{e}(i)$ is assumed to

be spatially white, Gaussian distributed, and the source waveforms are considered as unknown deterministic, nonlinear LS coincides with the deterministic ML estimation [KV96]. (2.13) can be solved explicitly for

$$\mathbf{s}(i) = [\mathbf{A}(\boldsymbol{\phi})^H \mathbf{A}(\boldsymbol{\phi})]^{-1} \mathbf{A}(\boldsymbol{\phi})^H \mathbf{x}(i), \quad i = 1, \dots, N \quad (2.14)$$

Plugging this back into (2.13), we obtain a concentrated optimization problem

$$\hat{\boldsymbol{\phi}} = \arg \min_{\boldsymbol{\phi}} \frac{1}{N} \sum_{i=1}^N \|\mathbf{P}_{\mathbf{A}}^{\perp}(\boldsymbol{\phi}) \mathbf{x}(i)\|^2 \quad (2.15)$$

where

$$\begin{aligned} \mathbf{P}_{\mathbf{A}}^{\perp}(\boldsymbol{\phi}) &= \mathbf{I}_M - \mathbf{P}_{\mathbf{A}}(\boldsymbol{\phi}) \\ \mathbf{P}_{\mathbf{A}}(\boldsymbol{\phi}) &= \mathbf{A}(\boldsymbol{\phi}) [\mathbf{A}(\boldsymbol{\phi})^H \mathbf{A}(\boldsymbol{\phi})]^{-1} \mathbf{A}(\boldsymbol{\phi})^H \end{aligned}$$

are the orthogonal projection matrix, and corresponding projection matrix onto the column span of $\mathbf{A}(\boldsymbol{\phi})$, respectively. An alternative formulation is to maximize objective function

$$c(\boldsymbol{\phi}) = \frac{1}{N} \sum_{i=1}^N \|\mathbf{P}_{\mathbf{A}}(\boldsymbol{\phi}) \mathbf{x}(i)\|^2 = \text{Tr}\{\mathbf{P}_{\mathbf{A}}(\boldsymbol{\phi}) \hat{\mathbf{R}}\}$$

where $\text{Tr}\{\cdot\}$ denotes the matrix trace operator, and $\hat{\mathbf{R}}$ is the sample covariance matrix, as defined in (2.9). A useful geometric interpretation is that we seek for parameter $\boldsymbol{\phi}$, which maximizes the average projection of snapshots $\mathbf{x}(i)$, $i = 1, \dots, N$ onto the subspace spanned by the columns of $\mathbf{A}(\boldsymbol{\phi})$. For a single source, the above objective function reduces to the BF spectrum, as defined in (2.11).

Nonlinear LS and the equivalent deterministic ML can provide excellent statistical results, which is often considered as benchmark performance [SM97, AJM07]. In particular, the resolution does not only depend on M , but can be arbitrarily good, provided the SNR is sufficiently high and N is large [TF09]. However, this is achieved at a high computational cost. Solving (2.15) requires the optimization of a D -dimensional objective function [GP03], which generally has a complicated multimodal shape. Computationally efficient, but iterative, implementations are the iterative quadratic maximum likelihood (IQML) algorithm [BM86] for ULAs, the relaxation (RELAX) algorithm in [LS96, LZS97], or the method of alternating projections [ZW88b].

2.2.3 Subspace methods

To overcome the computationally demanding optimization, required for nonlinear LS of multiple sources, subspace methods have been proposed. Subspace methods are based

on an eigendecomposition of the covariance matrix

$$\mathbf{R} = \sum_{m=1}^M \lambda_m \mathbf{u}_m \mathbf{u}_m^H$$

where λ_m and \mathbf{u}_m , $m = 1, \dots, M$, respectively, are the eigenvalues ordered in decreasing magnitude, and corresponding eigenvectors of \mathbf{R} . From (2.8), and provided \mathbf{P} has full rank, one can see that the $M - D$ smallest eigenvalues are equal to σ^2 [KV96], whereas the D remaining eigenvalues are larger. Accordingly, the corresponding eigenvectors can be partitioned into signal and noise subspace \mathbf{U}_s and \mathbf{U}_n such that

$$\mathbf{R} = \mathbf{U}_s \mathbf{\Lambda}_s \mathbf{U}_s^H + \sigma^2 \mathbf{U}_n \mathbf{U}_n^H \quad (2.16)$$

where diagonal matrix $\mathbf{\Lambda}_s$ contains the D principal eigenvalues. It can be shown from (2.8) and (2.16) that

$$\text{span}\{\mathbf{A}(\phi)\} = \text{span}\{\mathbf{U}_s\} \perp \text{span}\{\mathbf{U}_n\}$$

where $\text{span}\{\cdot\}$ denotes the subspace spanned by the columns of a matrix. This observation can be directly exploited for DOA estimation. For instance, the popular MUSIC (multiple signal classification) algorithm [Sch86, Reprint from 1979] estimates the DOA parameters by the locations of the D largest peaks of pseudo spectrum

$$P_{\text{MUSIC}}(\phi) = \frac{1}{\|\hat{\mathbf{U}}_n^H \mathbf{a}(\phi)\|^2} \quad (2.17)$$

where $\hat{\mathbf{U}}_n$ is the estimated noise subspace, obtained from $\hat{\mathbf{R}}$ in (2.9). For spatially white Gaussian noise, the statistical performance of the MUSIC algorithm is asymptotically similar to nonlinear LS [SM97]. Yet, only a one-dimensional search is required. For particular array geometries, there are also analytic solutions, which do not require a spectral search, e.g. root-MUSIC [Bar83] or ESPRIT (estimation of signal parameters via rotational invariance techniques) [RK89]. A computationally efficient implementation of the required eigendecomposition of the sample covariance matrix, based on the Lanczos algorithm [GvL96], is the fast subspace decomposition in [XK94].

2.2.4 Comparison

For a single source, DOA estimation with the BF is computationally simple and equivalent with the nonlinear LS approach. In the presence of multiple sources, two cases can be distinguished. When the sources are well separated so that they are resolved in the BF spectrum, the corresponding estimates are generally biased. For large N , this

bias can be neglected and DOA estimation with the BF approximates the nonlinear LS solution [SM97]. When the sources are closely spaced, high-resolution DOA estimation is required. This can be the presented nonlinear LS or subspace methods, which have been compared in numerous studies including [SN89, SM97, vT02, AJM07].

A standard tool for performance assessment is the comparison with the CRB, which represents a lower bound on the error variance of unbiased estimators [vT68]. It has been derived in [SN89] for the deterministic signal model and spatially white Gaussian noise. In this case, the accuracy of nonlinear LS and MUSIC asymptotically approaches the CRB. For smaller SNR and N , however, the performance generally degrades due to the onset of estimation outliers. This performance breakdown is more severe for subspace methods and occurs earlier than for nonlinear LS [AJM07]. The assumption of spatially white noise is crucial for subspace methods. Their performance may degrade significantly otherwise. Nonlinear LS does not critically depend on this assumption and can be shown to provide asymptotically accurate results even for spatially correlated noise [SM97, SN88]. Subspace methods require multiple snapshots from non-coherent sources such that the signal subspace is fully represented. For a single snapshot or coherent sources, a suboptimal pre-processing can be applied for ULAs, which involves the formation of a spatially smoothed, forward/backward (FB) averaged sample covariance matrix [PK89]. In contrast, nonlinear LS is directly applicable with a single snapshot or coherent sources.

Regarding computational cost, subspace methods are based on an eigendecomposition and a one-dimensional search, whereas nonlinear LS is based on a computationally intensive optimization of a D -dimensional objective function. Depending on the situation, one has to decide which approach is more appropriate. For instance, when operating with high SNR and large N , subspace methods should be preferred for DOA estimation of multiple sources. However, for smaller SNR and N , nonlinear LS may represent a better choice, and one has to develop practicable implementations.

2.3 Source detection

The described methods for high-resolution DOA estimation assume that the number of sources D is known. This is generally not the case in practice and algorithms for source detection are required. There are non-parametric methods, which are based on the eigenvalues of the sample covariance matrix, and parametric methods, which are based on a joint detection/estimation approach.

The structure of the eigenvalues of the spatial covariance matrix has been described in Section 2.2.3. In practice, the sample covariance matrix is employed, and the described ideal structure is not valid. However, for large N , the $M - D$ smallest eigenvalues cluster around σ^2 . Hence, source detection is possible by determining the multiplicity of the smallest eigenvalues. Approaches based on sequential statistical hypothesis tests have been considered in [And63, WJ90, XRK94], whereas [WK85] is based on information theoretic criteria. Recent results of random matrix theory have been employed, e.g. in [KN09]. Another approach, which is especially suited for smaller N , is to model the noise eigenvalues using an exponential profile [GLC96, DHRD07].

A systematic parametric approach for source detection is to use a sequence of GLRTs [OVSN93, Eri01, AN10]. This requires ML estimation of unknown parameters for an increasing hypothetical source number until a decision is made. The performance is generally superior when compared to non-parametric approaches, especially for smaller SNR and N [KV96]. However, this is achieved at a high computational cost.

2.4 Phase autocalibration for uniform rectangular arrays

We consider the case, when the array has been initially calibrated with off-line calibration measurements. Due to unmodeled effects or a time-varying sensor environment, the resulting model of the array response may still deviate from its true value. The proposed autocalibration method aims at mitigating the effect of the remaining errors in the array response.

Several autocalibration techniques have been developed to correct gain and phase estimation errors [PK85, FW88, WRM94, SL00, LE06]. Such errors may result from sensor imperfections or from coherent local scattering effects [GM98]. In other applications, phase errors dominate gain errors. Therefore, the localization performance in the presence of phase errors has been analyzed [RMS88], and autocalibration techniques have been developed, which take into account only phase errors [WRM94, RGB00]. Apart from sensor imperfections, such errors may be caused, e.g. by wavefront distortions due to medium inhomogeneities [RGB00, WTNV10], errors in the presumed array geometry, or an imperfectly known carrier frequency. Although the deviation of the presumed array response from its true value often is direction-dependent, a number of autocalibration techniques assume that the gain and phase error are the same for several sources. The latter assumption is valid if the sources are closely spaced so

that the directional dependency of the error in the presumed array response can be neglected. This is practically relevant, e.g. for active radar systems, if narrow transmit beams are used, or in radio astronomy, if the individual antennas have a narrow field-of-view [WTNV10]. We remark that the method proposed in this section is conceptually related to the redundancy averaging used in radio astronomy [NWAH09].

Autocalibration with arbitrary array geometries can be done using a maximum a posteriori (MAP) approach [WOV91, VS94, JSO98]. In this case, the joint optimization with respect to DOA and array error parameters can be regularized by considering the array errors as random nuisance parameters, leading to a DOA estimator which is robust against array perturbations. In general, the MAP approach requires a computationally intensive non-convex optimization procedure. Moreover, only small deviations from the nominal model can be corrected, as it is based on a local first-order approximation of the error in the presumed array response.

When performing autocalibration with a ULA, it is possible to exploit the structure of the ideal array response. In [PK85], an LS approach has been proposed to estimate gain and phase error parameters, based on the Toeplitz structure of the spatial covariance matrix of the unperturbed array. More specifically, the equality of the elements on the diagonals of the spatial covariance matrix is exploited to construct a set of equations, which is then solved by means of the LS principle. The described principle of gain and phase autocalibration for a ULA can also be applied by only utilizing the information on the main diagonal for gain estimation, and on the first super-diagonal for phase estimation [SL00]. This simplification has been analyzed in [LE06], where it was found that interestingly the best simulative results are achieved when only the first super-diagonal is considered for phase estimation. For joint DOA and phase error estimation with ULAs, there is an unidentifiable rotation factor. This ambiguity can be resolved by using a known phase error difference at two reference sensors, or the DOA of a reference source. Since this additional information is rarely available in practice, the phase errors can be constrained to have zero mean [WRM94]. An alternative approach to resolve the rotational ambiguity is to determine the phase errors with minimum norm [LE06].

All mentioned references have considered one-dimensional DOA estimation. However, in many applications both azimuth and elevation angles are of interest. For this reason, we present an extension of the work in [WRM94] and [LE06] to two-dimensional DOA estimation with phase autocalibration for a URA. The remaining section is structured as follows. In Section 2.4.1, the perturbed data model is described along with the associated ambiguity problem, and an approximate CRB is provided. The proposed algorithm for phase autocalibration with single source is presented in Section 2.4.2, and

its mean squared error (MSE) performance is derived. In Section 2.4.3, an extension for the case with multiple sources is proposed. Simulation results are presented in Section 2.4.4. Finally, conclusions are drawn in Section 2.4.5.

2.4.1 Perturbed data model

Consider a URA, as depicted in Figure 2.2, with $M = M_x M_y$ elements, and a steering vector, given in (2.4). For convenience, electrical angles ψ_x and ψ_y are used as DOA parameters. We first consider the case with a single source, which is practically relevant in various applications. For instance, in many radar systems, there is at most one target per range-Doppler processing cell. In the presence of phase errors, the perturbed signal model is

$$\tilde{\mathbf{x}}(i) = \mathbf{\Phi} \mathbf{a}(\psi_x, \psi_y) s(i) + \mathbf{e}(i), \quad i = 1, \dots, N \quad (2.18)$$

where

$$\mathbf{\Phi} = \text{diag}\{e^{j\varphi_1}, \dots, e^{j\varphi_M}\}$$

is a phase error matrix, $\text{diag}\{\cdot\}$ denotes the diagonal matrix operator, and $\varphi_1, \dots, \varphi_M$ are the phase error parameters. The corresponding spatial covariance matrix is

$$\tilde{\mathbf{R}} = \text{E}\{\tilde{\mathbf{x}}(i)\tilde{\mathbf{x}}(i)^H\} = P \mathbf{\Phi} \mathbf{a}(\psi_x, \psi_y) \mathbf{a}(\psi_x, \psi_y)^H \mathbf{\Phi}^H + \sigma^2 \mathbf{I}_M. \quad (2.19)$$

where P is the variance of waveform $s(i)$. To describe the element structure of a URA covariance matrix, in particular of the outer product of the steering vectors, we employ indexing variables

$$m = m_x + (m_y - 1)M_x, \quad n = n_x + (n_y - 1)M_x \quad (2.20)$$

for $m_x, n_x = 1, \dots, M_x$ and $m_y, n_y = 1, \dots, M_y$, so that we have

$$[\mathbf{a}(\psi_x, \psi_y) \mathbf{a}(\psi_x, \psi_y)^H]_{m,n} = e^{j[(m_x - n_x)\psi_x + (m_y - n_y)\psi_y]} \quad (2.21)$$

where, according to (2.20), variables m and n are functions of m_x and m_y , and n_x and n_y , respectively. Consequently, the elements of $\tilde{\mathbf{R}}$ can be expressed as

$$[\tilde{\mathbf{R}}]_{m,n} = P e^{j[\varphi_m - \varphi_n + (m_x - n_x)\psi_x + (m_y - n_y)\psi_y]} + \sigma^2 \delta_{m,n}. \quad (2.22)$$

where $\delta_{m,n}$ denotes the Kronecker delta function, which is unity for $m = n$ and zero otherwise.

The autocalibration problem is posed as follows: given snapshots $\tilde{\mathbf{x}}(i)$, $i = 1, \dots, N$ from model (2.18), jointly estimate parameters ψ_x , ψ_y and $\varphi_1, \dots, \varphi_M$.

2.4.1.1 Ambiguity

Without the knowledge of $s(i)$, it is only possible to determine the array response up to a complex scalar. Consequently, we set $\varphi_1 = 0$, and only search for the remaining parameters

$$\boldsymbol{\rho} = [\psi_x, \psi_y, \boldsymbol{\varphi}^T]^T \quad (2.23)$$

with $\boldsymbol{\varphi} = [\varphi_2, \dots, \varphi_M]^T$.

Another identification problem occurs when the phase errors in $\boldsymbol{\varphi}$ exhibits a structure which resembles the phases of steering vector $\mathbf{a}(\psi_x, \psi_y)$, as defined in (2.4). Note that the phases of the nominal steering vector can be interpreted as a two-dimensional linear function of the sensor positions. If $\varphi_2, \dots, \varphi_M$ have a similar structure, they cannot be distinguished from the phases of a steering vector, which leads to a pointing ambiguity. Hence, we can rewrite the perturbed steering vector as

$$\boldsymbol{\Phi}(\boldsymbol{\varphi})\mathbf{a}(\psi_x, \psi_y) = \boldsymbol{\Phi}(\boldsymbol{\varphi} + \mathbf{M}_\varphi\boldsymbol{\beta})\mathbf{a}(\psi_x - \beta_x, \psi_y - \beta_y) \quad (2.24)$$

with $\boldsymbol{\beta} = [\beta_x, \beta_y]^T$ and

$$\mathbf{M}_\varphi = \mathbf{L}_1[\mathbf{1}_{M_y} \otimes \boldsymbol{\delta}_x, \boldsymbol{\delta}_y \otimes \mathbf{1}_{M_x}] \in \mathbb{Z}^{(M-1) \times 2} \quad (2.25)$$

where $\mathbf{L}_1 = [\mathbf{0}, \mathbf{I}_{M-1}]$ is a selection matrix, which selects the second to last row from a matrix with M rows, $\mathbf{0}$ is a column vector of zeros with conformable dimensions, $\mathbf{1}_n$ is a column vector of n ones, and

$$\begin{aligned} \boldsymbol{\delta}_x &= [0, 1, \dots, M_x - 1]^T \\ \boldsymbol{\delta}_y &= [0, 1, \dots, M_y - 1]^T. \end{aligned}$$

Consequently, for all $\boldsymbol{\beta} \in \mathbb{R}^{2 \times 1}$, parameters

$$\boldsymbol{\rho} = \boldsymbol{\rho}_0 + \mathbf{M}_\rho\boldsymbol{\beta} \quad (2.26)$$

with

$$\mathbf{M}_\rho = [-\mathbf{I}_2, \mathbf{M}_\varphi^T]^T \in \mathbb{Z}^{(M+1) \times M} \quad (2.27)$$

lead to the same perturbed steering vector. In other words, $\boldsymbol{\rho}$ is not uniquely identifiable. We define $\boldsymbol{\rho}_0$ such that the corresponding $\boldsymbol{\varphi}_0 = \mathbf{L}_2\boldsymbol{\rho}_0$, where $\mathbf{L}_2 = [\mathbf{0}, \mathbf{0}, \mathbf{I}_{M-1}]$, satisfies

$$\mathbf{M}_\varphi^T\boldsymbol{\varphi}_0 = \mathbf{0}.$$

It appears reasonable to assume the phase errors to be i.i.d. such that asymptotically, for large M_x and M_y , there is no linear structure across the x - and y -direction of the URA and we have $\mathbf{M}_\varphi^T\boldsymbol{\varphi} = \mathbf{0}$. To obtain a unique solution, we therefore propose to choose $\boldsymbol{\rho}$ such that this condition is fulfilled. If the phase errors are not i.i.d., a modified condition can be obtained by taking into account a known correlation structure.

2.4.1.2 Cramér-Rao bound

To determine the CRB for the described joint estimation problem, we assume $\boldsymbol{\varphi}$ to be a Gaussian random variable with zero mean and known covariance $\sigma_\varphi^2 \mathbf{I}_{M-1}$. The full parameter set, denoted with $\boldsymbol{\Theta}$, then contains deterministic parameters ψ_x , ψ_y , P , and σ^2 , and stochastic parameter $\boldsymbol{\varphi}$. Therefore, the Fisher information matrix (FIM) is of the form [vT68]

$$\mathbf{J} = \mathbf{J}_D + \mathbf{J}_P$$

where \mathbf{J}_D represents information obtained from the data in $\mathbf{X} = [\tilde{\mathbf{x}}(1), \dots, \tilde{\mathbf{x}}(N)]$, and \mathbf{J}_P represents a priori information. Its respective elements are given by

$$\begin{aligned} [\mathbf{J}_D]_{m,n} &= -\mathbb{E} \left\{ \frac{\partial^2}{\partial \Theta_m \partial \Theta_n} \ln p_{\mathbf{X}|\boldsymbol{\Theta}}(\mathbf{X}|\boldsymbol{\Theta}) \right\} \\ [\mathbf{J}_P]_{m,n} &= -\mathbb{E} \left\{ \frac{\partial^2}{\partial \Theta_m \partial \Theta_n} \ln p_\varphi(\boldsymbol{\varphi}) \right\} \end{aligned}$$

where $p_{\mathbf{X}|\boldsymbol{\Theta}}(\mathbf{X}|\boldsymbol{\Theta})$ is the likelihood function and $p_\varphi(\boldsymbol{\varphi})$ is the assumed prior distribution. However, \mathbf{J}_D cannot be easily evaluated because of the expectation with respect to $\boldsymbol{\varphi}$, and because of nuisance parameters P and σ^2 . It has been proposed in [ZW88a] to obtain an approximate FIM by evaluating \mathbf{J}_D at $\boldsymbol{\varphi}$. By following similar steps as in [WOV91], the block of this approximate CRB matrix corresponding to parameters ψ_x , ψ_y , and $\boldsymbol{\varphi}$ is given by

$$\mathbf{ACRB}^{-1} = \frac{2N}{\sigma^2} \text{Re} \left\{ \begin{bmatrix} h_{xx} & h_{xy} & \mathbf{h}_{x\varphi} \\ h_{yx} & h_{yy} & \mathbf{h}_{y\varphi} \\ \mathbf{h}_{\varphi x} & \mathbf{h}_{\varphi y} & \mathbf{H}_{\varphi\varphi} \end{bmatrix} \right\} + \begin{bmatrix} 0 & 0 & \mathbf{0}^T \\ 0 & 0 & \mathbf{0}^T \\ \mathbf{0} & \mathbf{0} & \frac{1}{\sigma_\varphi^2} \mathbf{I}_{M-1} \end{bmatrix} \quad (2.28)$$

with elements

$$\begin{aligned} h_{xx} &= \mathbf{d}_x^H \mathbf{P}_{\tilde{\mathbf{a}}}^\perp \mathbf{d}_x \Sigma \\ h_{xy} &= \mathbf{d}_x^H \mathbf{P}_{\tilde{\mathbf{a}}}^\perp \mathbf{d}_y \Sigma \\ h_{yx} &= \mathbf{d}_y^H \mathbf{P}_{\tilde{\mathbf{a}}}^\perp \mathbf{d}_x \Sigma \\ h_{yy} &= \mathbf{d}_y^H \mathbf{P}_{\tilde{\mathbf{a}}}^\perp \mathbf{d}_y \Sigma \\ \mathbf{h}_{x\varphi} &= (\mathbf{d}_x^H \mathbf{P}_{\tilde{\mathbf{a}}}^\perp \mathbf{L}_1^T) \odot \mathbf{d}_\varphi^T \Sigma \\ \mathbf{h}_{y\varphi} &= (\mathbf{d}_y^H \mathbf{P}_{\tilde{\mathbf{a}}}^\perp \mathbf{L}_1^T) \odot \mathbf{d}_\varphi^T \Sigma \\ \mathbf{h}_{\varphi x} &= \Sigma \mathbf{d}_\varphi \odot (\mathbf{L}_1 \mathbf{P}_{\tilde{\mathbf{a}}}^\perp \mathbf{d}_x^*) \\ \mathbf{h}_{\varphi y} &= \Sigma \mathbf{d}_\varphi \odot (\mathbf{L}_1 \mathbf{P}_{\tilde{\mathbf{a}}}^\perp \mathbf{d}_y^*) \\ \mathbf{H}_{\varphi\varphi} &= \Sigma (\mathbf{d}_\varphi \mathbf{d}_\varphi^H) \odot (\mathbf{L}_1 \mathbf{P}_{\tilde{\mathbf{a}}}^\perp \mathbf{L}_1^T) \end{aligned}$$

where \odot denotes the element-wise matrix product,

$$\mathbf{P}_{\tilde{\mathbf{a}}}^\perp = \mathbf{I}_M - \tilde{\mathbf{a}}(\tilde{\mathbf{a}}^H \tilde{\mathbf{a}})^{-1} \tilde{\mathbf{a}}^H$$

is the orthogonal projection matrix of perturbed steering vector $\tilde{\mathbf{a}} = \mathbf{\Phi}(\boldsymbol{\varphi})\mathbf{a}(\psi_x, \psi_y)$, $\Sigma = P^2\tilde{\mathbf{a}}^H\tilde{\mathbf{R}}^{-1}\tilde{\mathbf{a}}$, and

$$\begin{aligned}\mathbf{d}_x &= \frac{\partial\tilde{\mathbf{a}}}{\partial\psi_x} = \mathbf{\Phi}(\boldsymbol{\varphi})[\mathbf{a}_y(\psi_y) \otimes j\text{diag}\{\boldsymbol{\delta}_x\}\mathbf{a}_x(\psi_x)] \\ \mathbf{d}_y &= \frac{\partial\tilde{\mathbf{a}}}{\partial\psi_y} = \mathbf{\Phi}(\boldsymbol{\varphi})[j\text{diag}\{\boldsymbol{\delta}_y\}\mathbf{a}_y(\psi_y) \otimes \mathbf{a}_x(\psi_x)] \\ \mathbf{d}_\varphi &= \left[\frac{\partial[\tilde{\mathbf{a}}]_2}{\partial\varphi_2}, \dots, \frac{\partial[\tilde{\mathbf{a}}]_M}{\partial\varphi_M} \right]^T = j\mathbf{L}_1\tilde{\mathbf{a}}\end{aligned}$$

are partial derivatives of $\tilde{\mathbf{a}}$ with respect to ψ_x , ψ_y , and $\boldsymbol{\varphi}$, respectively. $\boldsymbol{\delta}_x$, $\boldsymbol{\delta}_y$, and \mathbf{L}_1 have been defined in Section 2.4.1.1.

In summary, the diagonal elements of the approximate CRB matrix, defined in (2.28), $[\mathbf{ACRB}]_{1,1}$, $[\mathbf{ACRB}]_{2,2}$ and $[\mathbf{ACRB}]_{i,i}$, $i = 3, \dots, M+1$ represent approximate lower bounds on the error variances of jointly estimating ψ_x, ψ_y , and the elements of $\boldsymbol{\varphi}$, respectively.

2.4.2 Proposed autocalibration algorithm

In the following, the proposed algorithm for phase autocalibration is presented and an analytical expression for its MSE performance is derived. We use the phase relations of elements of the perturbed spatial covariance matrix $\tilde{\mathbf{R}}$, as defined in (2.22). Due to the Hermitian symmetry, we only consider elements on the super-diagonals, i.e. $[\tilde{\mathbf{R}}]_{m,n}$ with $m < n$. The perturbed spatial covariance matrix is estimated using the sample covariance matrix of perturbed snapshots $\tilde{\mathbf{x}}(i)$,

$$\hat{\mathbf{R}} = \frac{1}{N} \sum_{i=1}^N \tilde{\mathbf{x}}(i)\tilde{\mathbf{x}}(i)^H. \quad (2.29)$$

For constructing equations from the phase measurements of the elements of $\hat{\mathbf{R}}$, we follow the general idea in [WRM94]. Using indexing variables m and n , as defined in (2.20), we have

$$\angle[\hat{\mathbf{R}}]_{m,n} = \varphi_m - \varphi_n + (m_x - n_x)\psi_x + (m_y - n_y)\psi_y + \epsilon_{m,n} \quad (2.30)$$

for $m_x, n_x = 1, \dots, M_x$ and $m_y, n_y = 1, \dots, M_y$, where $\epsilon_{m,n}$ are the phase estimation errors of the sample covariance matrix.

In Appendix 2.A.1, it is shown that, for sufficiently high SNR and/or large N , phase error term $\epsilon_{m,n}$ has zero mean and covariance

$$\mathbb{E}\{\epsilon_{m,n}\epsilon_{k,l}\} \approx \begin{cases} \frac{\sigma^2}{2PN} & \text{if } n = l \cap m \neq k \\ \frac{\sigma^2}{2PN} & \text{if } n \neq l \cap m = k \\ \frac{\sigma^2}{PN} + \frac{\sigma^4}{2P^2N} & \text{if } n = l \cap m = k \\ -\frac{\sigma^2}{2PN} & \text{if } n = k \cap m \neq l \\ -\frac{\sigma^2}{2PN} & \text{if } n \neq k \cap m = l \\ -\frac{\sigma^2}{PN} - \frac{\sigma^4}{2P^2N} & \text{if } n = k \cap m = l \\ 0 & \text{otherwise.} \end{cases} \quad (2.31)$$

Based on (2.30), we form two groups of equations, for which either $m_x - n_x$ or $m_y - n_y$ equals zero, and the other equals one. Note that these elements are least likely to require phase unwrapping [WRM94], and hence lead to an estimator which is more robust.

Group 1: Phase measurements from elements on the first super-diagonal, for $m_x = 1, \dots, M_x - 1$ and $m_y = 1, \dots, M_y$

$$\angle[\hat{\mathbf{R}}]_{m,m+1} = \varphi_m - \varphi_{m+1} - \psi_x + \epsilon_{m,m+1}. \quad (2.32)$$

Group 2: Phase measurements from elements on super-diagonal M_x , for $m_x = 1, \dots, M_x$ and $m_y = 1, \dots, M_y - 1$

$$\angle[\hat{\mathbf{R}}]_{m,m+M_x} = \varphi_m - \varphi_{m+M_x} - \psi_y + \epsilon_{m,m+M_x}. \quad (2.33)$$

Generally more elements of $\hat{\mathbf{R}}$ can be considered. These have larger lag values $m_x - n_x$ or $m_y - n_y$, so that a phase unwrapping procedure, depending on $\boldsymbol{\rho}$, may be necessary. It is possible to use the proposed method to determine $\hat{\boldsymbol{\rho}}$ in a first stage. In a second stage, $\hat{\boldsymbol{\rho}}$ is used for phase unwrapping of the covariance matrix elements, which have not been used in the first stage, and a refined estimate is obtained. Note that when the proposed method fails in the first stage, then a subsequent phase unwrapping is likely to fail as well. Therefore, this approach can only improve the result in the asymptotic region, and is not addressed here.

In total, (2.32) and (2.33) contain

$$N_F = (M_x - 1)M_y + M_x(M_y - 1)$$

equations. These can be summarized by

$$\hat{\boldsymbol{\vartheta}} = \mathbf{F}\boldsymbol{\rho} + \boldsymbol{\epsilon} \quad (2.34)$$

where $\hat{\boldsymbol{\vartheta}} \in \mathbb{R}^{N_F \times 1}$ consists of the phase measurements of the elements of the sample covariance matrix according to Groups 1 and 2, $\mathbf{F} \in \mathbb{Z}^{N_F \times (M+1)}$ is the corresponding system matrix, and $\boldsymbol{\epsilon}$ is a vector of measurement errors.

Proposition: The rank of \mathbf{F} is $M - 1$.

Proof: Let us consider the case without measurement errors. We have $\boldsymbol{\vartheta} = \mathbf{F}\boldsymbol{\rho}$, which corresponds to N_F equations and $M + 1$ unknowns. Due to the non-identifiability of $\boldsymbol{\rho}$, as described in Section 2.4.1.1, the rank of \mathbf{F} must be less or equal $M - 1$.

Now assume ψ_x and ψ_y are given. In this case, (2.32) and (2.33) allow to recursively compute $\varphi_2, \dots, \varphi_M$ by

$$\varphi_2 = -\angle[\tilde{\mathbf{R}}]_{1,2} - \psi_x$$

and, for $m = 2, \dots, M - 1$

$$\varphi_{m+1} = \begin{cases} \varphi_m - \angle[\tilde{\mathbf{R}}]_{m,m+1} - \psi_x & \text{if } \text{mod}\{m, M_x\} \neq 0 \\ \varphi_{m-M_x+1} - \angle[\tilde{\mathbf{R}}]_{m-M_x+1,m+1} - \psi_y & \text{otherwise.} \end{cases}$$

Thus, the rank of \mathbf{F} cannot be less than $M - 1$, which concludes the proof. \square

As a consequence of the non-identifiability of $\boldsymbol{\rho}$ and the above proposition, we must have $\mathbf{F}\mathbf{M}_\rho = \mathbf{0}$. Thus, the optimum points of the LS optimization problem

$$\min_{\boldsymbol{\rho}} \|\mathbf{F}\boldsymbol{\rho} - \hat{\boldsymbol{\vartheta}}\|^2 \quad (2.35)$$

can be expressed as

$$\hat{\boldsymbol{\rho}} = \hat{\boldsymbol{\rho}}_{\text{MN}} + \mathbf{M}_\rho\boldsymbol{\beta} \quad (2.36)$$

where

$$\hat{\boldsymbol{\rho}}_{\text{MN}} = \mathbf{F}^+ \hat{\boldsymbol{\vartheta}}$$

represents the minimum norm solution of (2.35) [Dem97], and \mathbf{F}^+ is the Moore-Penrose pseudo-inverse of \mathbf{F} . We note that, given a truncated singular value decomposition $\mathbf{F} = \mathbf{U}_F \boldsymbol{\Lambda}_F \mathbf{V}_F^T$, where $\boldsymbol{\Lambda}_F$ is a positive definite diagonal matrix of dimension $M - 1$, this pseudo-inverse is given by $\mathbf{F}^+ = \mathbf{V}_F \boldsymbol{\Lambda}_F^{-1} \mathbf{U}_F^T$.

As discussed in Section 2.4.1.1, to obtain a unique solution, we constrain $\boldsymbol{\rho}$, or more specifically $\boldsymbol{\varphi} = \mathbf{L}_2\boldsymbol{\rho}$, such that $\mathbf{M}_\varphi^T \boldsymbol{\varphi} = \mathbf{0}$. Thus, we have

$$\mathbf{M}_\varphi^T \mathbf{L}_2 \hat{\boldsymbol{\rho}} = \mathbf{M}_\varphi^T \mathbf{L}_2 (\hat{\boldsymbol{\rho}}_{\text{MN}} + \mathbf{M}_\rho \boldsymbol{\beta}) = \mathbf{0}$$

which can be solved for

$$\boldsymbol{\beta} = -(\mathbf{M}_\varphi^T \mathbf{M}_\varphi)^{-1} \mathbf{M}_\varphi^T \mathbf{L}_2 \hat{\boldsymbol{\rho}}_{\text{MN}}$$

Insertion into (2.36) yields

$$\hat{\boldsymbol{\rho}}_0 = \mathbf{Q} \hat{\boldsymbol{\vartheta}} \quad (2.37)$$

with

$$\mathbf{Q} = [\mathbf{I}_{M+1} - \mathbf{M}_\rho (\mathbf{M}_\varphi^T \mathbf{M}_\varphi)^{-1} \mathbf{M}_\varphi^T \mathbf{L}_2] \mathbf{F}^+ \quad (2.38)$$

where matrices \mathbf{M}_ρ , \mathbf{M}_φ , and \mathbf{L}_2 have been defined in Section 2.4.1.1. Note that the latter solution can also be interpreted as the vector $\hat{\boldsymbol{\rho}}$ of (2.36) with the minimum norm of φ .

Regarding computational complexity, the construction of $\hat{\boldsymbol{\vartheta}}$ involves the computation of $\hat{\mathbf{R}}$, and the phase calculation of selected elements. When measurement vector $\hat{\boldsymbol{\vartheta}}$ is available and \mathbf{Q} is computed off-line, $\hat{\boldsymbol{\rho}}_0$ is determined by a real-valued matrix vector product with $(M+1)N_F$ operations. Therefore, the proposed estimator in (2.37) can be regarded as computationally simple.

To analyze the estimation performance in terms of MSE, we first consider the bias, which can be evaluated as

$$\text{bias}\{\hat{\boldsymbol{\rho}}_0\} = \text{E}\{\hat{\boldsymbol{\rho}}_0\} - \boldsymbol{\rho} = \mathbf{Q}(\mathbf{F}\boldsymbol{\rho} + \text{E}\{\boldsymbol{\epsilon}\}) - \boldsymbol{\rho} = \mathbf{P}_\varphi \boldsymbol{\rho} \quad (2.39)$$

where $\mathbf{P}_\varphi = \mathbf{Q}\mathbf{F} - \mathbf{I}_{M+1}$, and we have used that $\boldsymbol{\epsilon}$ has zero mean. The bias depends on the parameter itself and how much $\mathbf{Q}\mathbf{F}$ differs from an identity matrix. One can interpret \mathbf{P}_φ as a projection-like operator onto the unidentifiable components of φ . The MSE is given by

$$\begin{aligned} \text{MSE}\{\hat{\boldsymbol{\rho}}_0\} &= \text{E}\{(\hat{\boldsymbol{\rho}}_0 - \boldsymbol{\rho})(\hat{\boldsymbol{\rho}}_0 - \boldsymbol{\rho})^T\} \\ &= \text{E}\{(\mathbf{Q}[\mathbf{F}\boldsymbol{\rho} + \boldsymbol{\epsilon}] - \boldsymbol{\rho})(\mathbf{Q}[\mathbf{F}\boldsymbol{\rho} + \boldsymbol{\epsilon}] - \boldsymbol{\rho})^T\} \\ &= \text{E}\{(\mathbf{P}_\varphi \boldsymbol{\rho} + \mathbf{Q}\boldsymbol{\epsilon})(\mathbf{P}_\varphi \boldsymbol{\rho} + \mathbf{Q}\boldsymbol{\epsilon})^T\} \\ &= \mathbf{P}_\varphi \boldsymbol{\rho} \boldsymbol{\rho}^T \mathbf{P}_\varphi^T + \mathbf{Q} \text{E}\{\boldsymbol{\epsilon} \boldsymbol{\epsilon}^T\} \mathbf{Q}^T \end{aligned} \quad (2.40)$$

where $\text{E}\{\boldsymbol{\epsilon} \boldsymbol{\epsilon}^T\}$ can be evaluated using (2.31). The MSE consists of a squared bias term and a variance term due to the additive phase errors.

We remark that the proposed estimator can be generalized straightforwardly to array geometries, which satisfy the outer product structure from (2.4).

2.4.3 Extension for multiple sources

The perturbed signal model for a superposition of D uncorrelated sources, where we assume D to be known, is

$$\tilde{\mathbf{x}}(i) = \sum_{k=1}^D \mathbf{\Phi} \mathbf{a}(\psi_{x,k}, \psi_{y,k}) s_k(i) + \mathbf{e}(i), \quad i = 1, \dots, N \quad (2.41)$$

where $\psi_{x,k}$, $\psi_{y,k}$, and $s_k(i)$ are the DOA parameters and waveform of source k , respectively. The corresponding spatial covariance matrix is

$$\tilde{\mathbf{R}} = \mathbb{E}\{\tilde{\mathbf{x}}(i)\tilde{\mathbf{x}}(i)^H\} = \sum_{k=1}^D P_k \mathbf{\Phi} \mathbf{a}(\psi_{x,k}, \psi_{y,k}) \mathbf{a}(\psi_{x,k}, \psi_{y,k})^H \mathbf{\Phi}^H + \sigma^2 \mathbf{I}_M \quad (2.42)$$

where P_k is the variance of waveform $s_k(i)$. When using indexing variables m and n , as defined in (2.20), one can observe that the outer product of steering vectors in (2.21) is a Toeplitz-block Toeplitz matrix, since the elements are only a function of $m_x - n_x$ and $m_y - n_y$. In the unperturbed case with $\mathbf{\Phi} = \mathbf{I}_M$, the spatial covariance matrix in (2.42) is a sum of D Toeplitz-block Toeplitz matrices and a diagonal matrix, and therefore also satisfies the Toeplitz-block Toeplitz structure. This structure can be exploited for phase calibration [HZ11b]. In particular, we use the fact that elements of the unperturbed covariance matrix, which are on the same super-diagonal within blocks, and at the same position from block to block, are equal. So by selecting corresponding elements, the phases differences will only depend on the phase error parameters.

We follow the idea in [SL00] and [LE06], and select only elements from $\angle \hat{\mathbf{R}}$, for which either $m_x - n_x$ or $m_y - n_y$ equals zero, and the other equals one. Four groups of relations have been identified, and are described below. $\xi_m^{(l)}$, $l = 1, 2, 3, 4$ denote the additive phase errors of respective groups.

Group 1: Relations within blocks, on first super-diagonal, for $m_x = 1, \dots, M_x - 2$ and $m_y = 1, \dots, M_y$

$$\begin{aligned} \angle[\hat{\mathbf{R}}]_{m+1, m+2} - \angle[\hat{\mathbf{R}}]_{m, m+1} \\ = \varphi_m - 2\varphi_{m+1} + \varphi_{m+2} + \xi_m^{(1)}. \end{aligned} \quad (2.43)$$

Group 2: Relations from block to block, on first super-diagonal, for $m_x = 1$ and $m_y = 1, \dots, M_y - 1$

$$\begin{aligned} \angle[\hat{\mathbf{R}}]_{m+M_x, m+M_x+1} - \angle[\hat{\mathbf{R}}]_{m, m+1} \\ = \varphi_m - \varphi_{m+1} - \varphi_{m+M_x} + \varphi_{m+M_x+1} + \xi_m^{(2)}. \end{aligned} \quad (2.44)$$

Group 3: Relations within blocks, on super-diagonal M_x , for $m_x = 1, \dots, M_x - 1$ and $m_y = 1, \dots, M_y - 1$

$$\begin{aligned} & \angle[\hat{\mathbf{R}}]_{m+1, m+M_x+1} - \angle[\hat{\mathbf{R}}]_{m, m+M_x} \\ &= \varphi_m - \varphi_{m+M_x} - \varphi_{m+1} + \varphi_{m+M_x+1} + \xi_m^{(3)}. \end{aligned} \quad (2.45)$$

Group 4: Relations from block to block, on super-diagonal M_x , for $m_x = 1$ and $m_y = 1, \dots, M_y - 2$

$$\begin{aligned} & \angle[\hat{\mathbf{R}}]_{m+M_x, m+2M_x} - \angle[\hat{\mathbf{R}}]_{m, m+M_x} \\ &= \varphi_m - 2\varphi_{m+M_x} + \varphi_{m+2M_x} + \xi_m^{(4)}. \end{aligned} \quad (2.46)$$

In total, (2.43)-(2.46) contain

$$N_G = (M_x - 2)M_y + M_x(M_y - 1) + (M_y - 2) \quad (2.47)$$

equations. These can be summarized by

$$\hat{\boldsymbol{\vartheta}}_\Delta = \mathbf{G}\boldsymbol{\varphi} + \boldsymbol{\xi} \quad (2.48)$$

where $\hat{\boldsymbol{\vartheta}}_\Delta \in \mathbb{R}^{N_G \times 1}$ consists of the phase measurement differences of elements of the sample covariance matrix according to Groups 1-4, $\mathbf{G} \in \mathbb{Z}^{N_G \times (M-1)}$ is the corresponding system matrix, and $\boldsymbol{\xi}$ is a vector of measurement errors.

The number of independent relations, and so the rank of \mathbf{G} , is at most $M - 3$, which results from the unidentifiable linear components of $\boldsymbol{\varphi}$, as indicated in Section 2.4.1.1. Hence, the LS approach

$$\min_{\boldsymbol{\varphi}} \|\mathbf{G}\boldsymbol{\varphi} - \hat{\boldsymbol{\vartheta}}_\Delta\|^2 \quad (2.49)$$

leads to a non-unique solution. Following a similar approach as above, (2.49) is solved with the smallest norm of $\boldsymbol{\varphi}$, leading to the minimum norm solution

$$\hat{\boldsymbol{\varphi}}_{\text{MN}} = \mathbf{G}^+ \hat{\boldsymbol{\vartheta}}_\Delta \quad (2.50)$$

where \mathbf{G}^+ is the Moore-Penrose pseudo-inverse of \mathbf{G} , obtained similarly as described in Section 2.4.2 for \mathbf{F} .

2.4.4 Simulation results

We first present simulation results using the proposed algorithm for joint DOA estimation and phase calibration in the single source case. If not otherwise stated, $N = 4M$

snapshots are simulated according to model (2.18), using a square 16-element URA, and DOA parameters $\psi_x = -0.5$ and $\psi_y = 0.25$. The phase error parameters in $\boldsymbol{\varphi}$ are generated from a Gaussian distribution with zero mean and variance σ_φ^2 .

In all simulations, we compare the performance of the proposed algorithm with the analytically found MSE from (2.40) and the approximate CRB from (2.28). As performance metrics for DOA estimation and phase calibration, we consider the averaged root mean squared error (RMSE), defined by

$$\begin{aligned} \text{RMSE}_\psi^2 &= \frac{1}{\text{MC}} \sum_{k=1}^{\text{MC}} \frac{1}{2} [(\hat{\psi}_{x,k} - \psi_x)^2 + (\hat{\psi}_{y,k} - \psi_y)^2] \\ \text{RMSE}_\varphi^2 &= \frac{1}{\text{MC}} \sum_{k=1}^{\text{MC}} \frac{1}{M-1} \|\hat{\boldsymbol{\varphi}}_k - \boldsymbol{\varphi}\|^2 \end{aligned}$$

where $\hat{\psi}_{x,k}$, $\hat{\psi}_{y,k}$ and $\hat{\boldsymbol{\varphi}}_k$ are the DOA and phase error estimates in run k , and $\text{MC} = 10^4$ is the number of Monte-Carlo runs. Later, we also present simulation results using the proposed algorithm for multiple sources.

2.4.4.1 Variance of the phase

Since the derived result for the phase error covariance in (2.31) differs from the results obtained in [LE06] or [WRM94], we present a simulation example for validation. In four scenarios with different source variance P and number of snapshots N , the noise standard deviation σ is varied. We calculate the empirical standard deviation of $\angle[\hat{\mathbf{R}}]_{1,2}$ and compare it with (2.31), in particular the square root of $\text{E}\{\epsilon_{1,2}^2\}$. The result is shown in Figure 2.3. One can observe that our derivation, shown in Appendix 2.A.1, represents a good match with the empirical results. Note that the scenarios with the same product PN are asymptotically equivalent for small σ . For large σ , the phase measurements of the sample covariance matrix become arbitrary and are limited from above by the standard deviation of a uniform distribution between 0 and 2π .

2.4.4.2 Effect of SNR and array size

We simulate DOA estimation and the phase calibration performance of the proposed algorithm from (2.37) versus SNR, for square URAs with $M_x = 4, 8, \text{ and } 16$, and with $\sigma_\varphi = 0.05\pi$. The results are shown in Figure 2.4. One can observe, that the performance of the proposed approach is accurately predicted by the analytically found

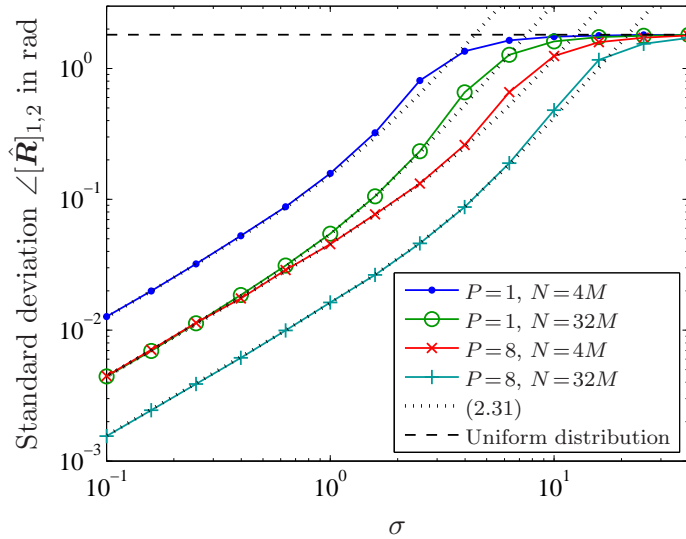


Figure 2.3. Simulation results. Empirical standard deviation for the phase of the elements of the sample covariance matrix versus noise standard deviation σ , in several scenarios, compared with the derived expression from (2.31).

MSE. For sufficiently high SNR, the performance is close to the approximate CRB for both DOA estimation and phase calibration. Note that this is even possible by considering only selected elements from $\hat{\mathbf{R}}$. From considering more elements, the threshold performance can be improved, but this would require a non-trivial technique to deal with the phase unwrapping problem. Also, one can observe that the convergence error is inversely proportional to the URA size. This convergence level is due to the unidentifiable components of $\boldsymbol{\rho}$, and corresponds to a remaining uncertainty. This behavior seems to be captured by the approximate CRB, so that it can be considered as a valid performance bound.

2.4.4.3 Comparison with BF matching and MAP-NSF

The proposed algorithm is compared with two other methods. First, we use the simple and intuitive approach described in [HZ11b], based on the conventional BF. Second, we use an MAP approach, in which distributional information of the random parameter is employed. In particular, we consider the implementation in [VS94] with noise subspace fitting (NSF), which is describes in detail in Appendix 2.A.2.

The idea of the BF matching approach is to estimate the unknown phase errors by matching the ideal steering vector with an unstructured estimate of the array response

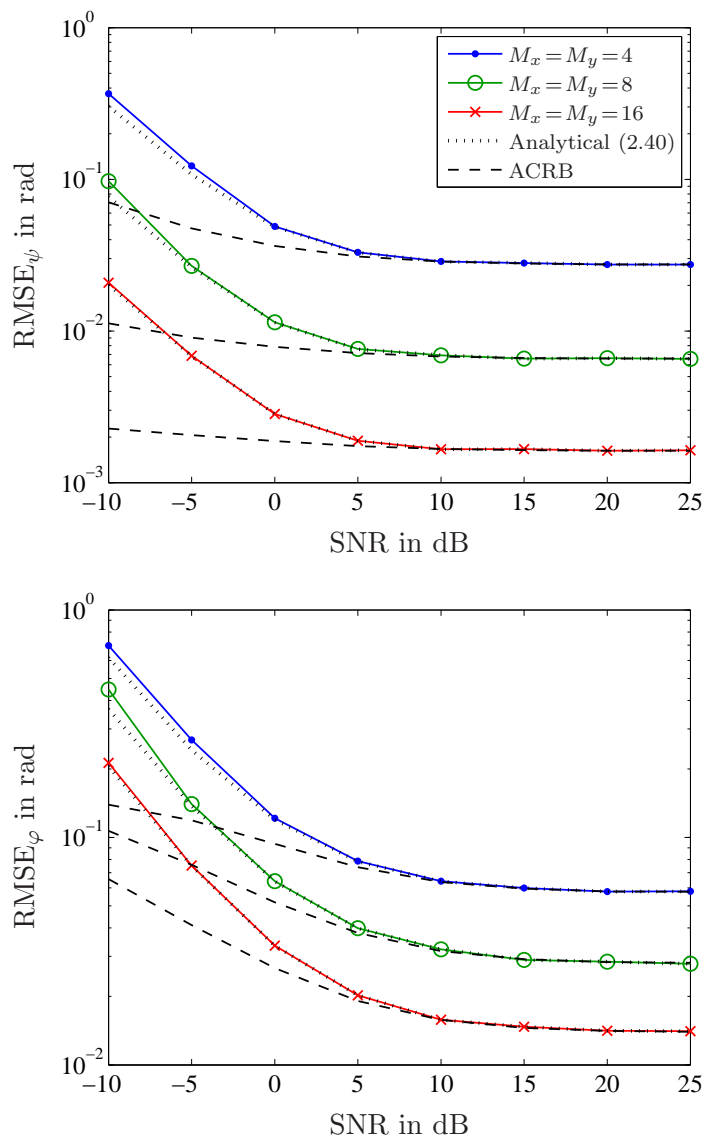


Figure 2.4. Simulation results. RMSE of the proposed approach for DOA estimation (top) and phase calibration (bottom) versus SNR, for $\sigma_\varphi = 0.05\pi$ and several URA sizes, compared with the analytical MSE from (2.40) and the approximate CRB.

[HZ11b]. Towards this end, first, estimate the source waveform using

$$\hat{s}(i) = \frac{1}{M} \mathbf{a}(\hat{\psi}_x, \hat{\psi}_y)^H \mathbf{x}(i), \quad i = 1, \dots, N \quad (2.51)$$

where $\hat{\psi}_x$ and $\hat{\psi}_y$ are the locations of the global maximum of the two-dimensional BF spectrum, given by

$$P_{\text{BF}}(\psi_x, \psi_y) = \mathbf{a}(\psi_x, \psi_y)^H \hat{\mathbf{R}} \mathbf{a}(\psi_x, \psi_y). \quad (2.52)$$

Second, find an unstructured estimate of the array response as

$$\hat{\boldsymbol{\alpha}} = \frac{\sum_{i=1}^N \hat{s}(i)^* \mathbf{x}(i)}{\sum_{i=1}^N |\hat{s}(i)|^2}. \quad (2.53)$$

Third, estimate the desired phase error parameters as

$$\hat{\varphi}_m = \angle[\hat{\boldsymbol{\alpha}}]_m - \angle[\mathbf{a}(\hat{\psi}_x, \hat{\psi}_y)]_m - \angle[\hat{\boldsymbol{\alpha}}]_1, \quad m = 2, \dots, M. \quad (2.54)$$

We remark that this approach assumes the phase errors to be sufficiently small such that the two-dimensional BF spectrum is not perturbed significantly.

To compare the proposed algorithm with the described methods, we simulate DOA estimation and the phase calibration performance versus σ_φ . We consider $M_x = M_y = 4$ and SNR = 15 dB. Figure 2.5 shows the obtained results. Regarding DOA estimation performance, the BF matching and MAP-NSF method prove to be robust against small phase errors. Both achieve the approximate CRB and should therefore be preferred over the proposed algorithm. However, for larger phase errors, the proposed algorithm is able to achieve optimum phase calibration and results in slightly improved DOA estimation performance. The same can be observed regarding phase calibration performance, except that the BF matching approach provides suboptimal results. We note that all methods break down when the phase errors are larger than $\pi/4$.

Regarding computational cost, the BF matching and MAP-NSF method are both based on a two-dimensional spectral search, and are therefore more complicated than the proposed algorithm, which only requires a matrix vector multiplication.

2.4.4.4 Resolution

Finally, we demonstrate that the proposed algorithm for the case with multiple sources, as described in Section 2.4.3, is able to improve the resolution performance. Towards this end, consider a scenario with two uncorrelated sources of equal power, and DOA

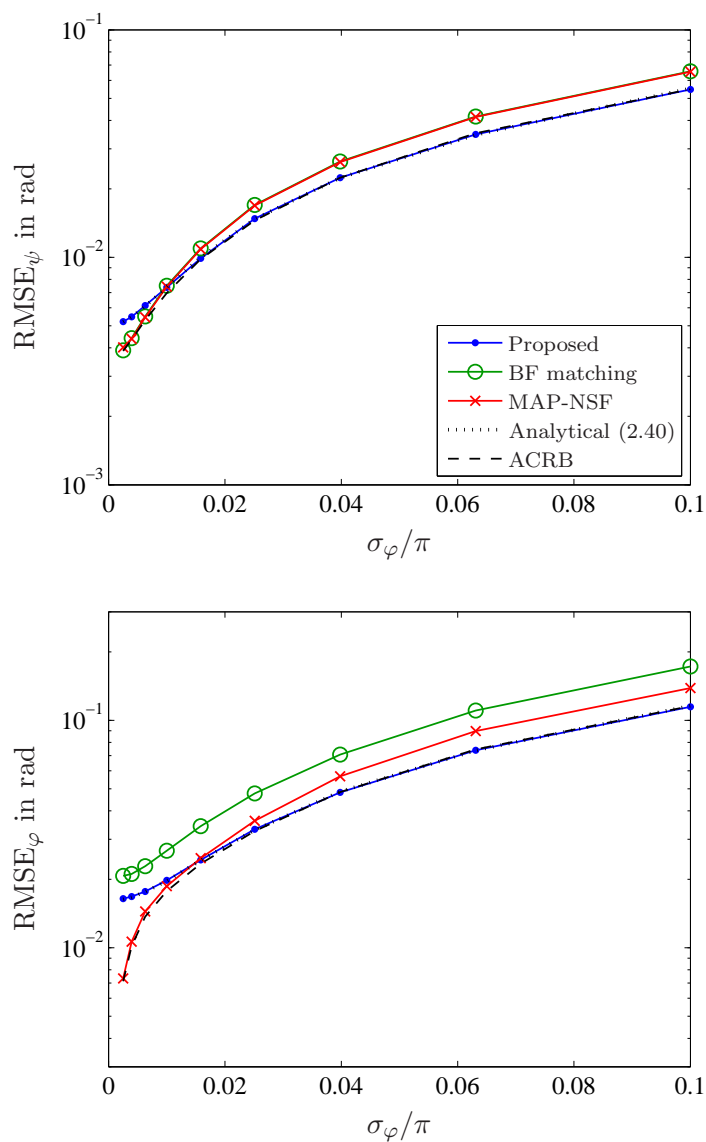


Figure 2.5. Simulation results and performance comparison. RMSE of DOA estimation (top) and phase calibration (bottom) versus phase error magnitude σ_φ , for $M_x = M_y = 4$ at SNR = 15 dB.

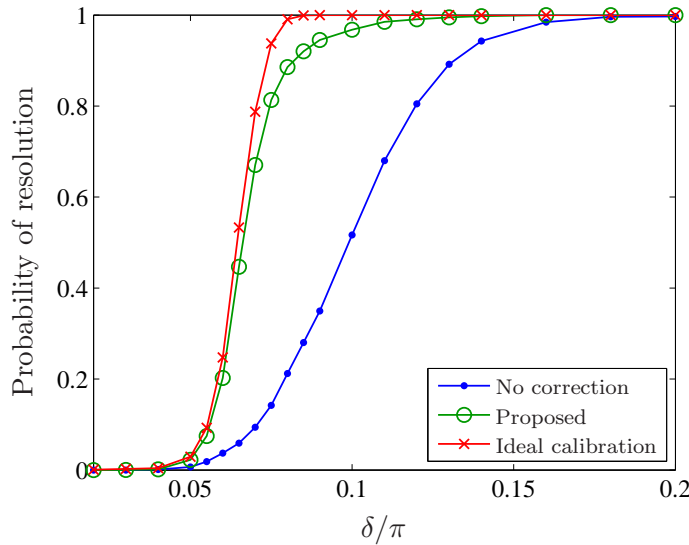


Figure 2.6. Simulation results. Empirical probability of resolution of two-dimensional MUSIC with no correction, proposed phase calibration and ideal calibration, versus angular separation δ , for $\sigma_\varphi = 0.05\pi$, $M_x = M_y = 4$ at SNR = 20 dB.

parameters $\psi_{x,1} = \psi_{y,1} = -\delta/(2\sqrt{2})$ and $\psi_{x,2} = \psi_{y,2} = \delta/(2\sqrt{2})$, such that the angular source separation is parameterized by

$$\delta = \sqrt{(\psi_{x,1} - \psi_{x,2})^2 + (\psi_{y,1} - \psi_{y,2})^2}.$$

We consider spectral two-dimensional MUSIC [vT02] for high-resolution DOA estimation. The corresponding pseudo spectrum is given by

$$P_{\text{MUSIC}}(\psi_x, \psi_y) = \frac{1}{\|\hat{\mathbf{U}}_n^H \hat{\mathbf{\Phi}} \mathbf{a}(\psi_x, \psi_y)\|^2}$$

where $\hat{\mathbf{U}}_n$ is the noise subspace, estimated from $\hat{\mathbf{R}}$ in (2.29) and $\hat{\mathbf{\Phi}}$ can be estimated using the proposed algorithm in Section 2.4.3. The two sources are considered as resolved if the locations of the two largest local maxima of the MUSIC pseudo spectrum are close to the true DOA parameters, i.e.

$$(\hat{\psi}_{x,1} - \psi_{x,1})^2 + (\hat{\psi}_{y,1} - \psi_{y,1})^2 < \left(\frac{\delta}{2}\right)^2 \quad \cap \quad (\hat{\psi}_{x,2} - \psi_{x,2})^2 + (\hat{\psi}_{y,2} - \psi_{y,2})^2 < \left(\frac{\delta}{2}\right)^2.$$

We simulate the empirical probability of resolution of two-dimensional MUSIC with no correction, the proposed phase calibration algorithm, and the ideal phase calibration, versus angular separation δ . We consider a square 16-element URA, SNR = 20 dB, and $\sigma_\varphi = 0.05\pi$. Figure 2.6 shows the obtained results. One can observe that the proposed method for phase calibration is able to substantially enhance the resolution performance

when compared with no correction. Note that the Friedlander-Weiss method [FW88] is not considered here, since it requires the two sources to be resolved in the uncalibrated state, and consequently cannot be used to enhance the resolution ability.

2.4.5 Conclusion

For the single source case, we have presented an algorithm for joint two-dimensional DOA estimation and phase calibration for URAs. The proposed algorithm results in a linear LS problem, which can be solved efficiently. An accurate analytical expression for the asymptotic MSE performance has been determined. Our simulation results suggest that the proposed algorithm achieves the approximate CRB under moderate conditions. We remark that the problem of phase autocalibration with URAs generally results in unidentifiable estimation due to an ambiguity problem. This has been described adequately, and a remedy in terms of a suitable constraint on the phase error parameters has been proposed.

Furthermore, an extension of the proposed algorithm to the case with multiple sources has been presented. This algorithm exploits the Toeplitz-block Toeplitz structure of the unperturbed covariance matrix. Note that the phase calibration method is decoupled from the DOA estimation and can be applied as a pre-processing step. The proposed algorithm allows to substantially enhance the resolution performance of high-resolution two-dimensional DOA estimation in the presence of phase errors.

For both cases, with a single source and multiple sources, the proposed autocalibration method can be straightforwardly reduced to the ULA geometry by using $M_y = 1$. In this case, only the corresponding first groups remain, and the resulting algorithms are equivalent with a special case of [WRM94], and [SL00], respectively.

2.A Appendix

2.A.1 Statistical properties of the sample covariance matrix

The sample covariance matrix of the perturbed data has been defined in (2.29). Its mean and a first-order approximation of the covariance between the phases of matrix elements are determined next.

In the following, the elements of vectors $\tilde{\mathbf{x}}(i)$, $\tilde{\mathbf{a}}$, and $\mathbf{e}(i)$ are denoted with $\tilde{x}_m(i)$, \tilde{a}_m , and $e_m(i)$, respectively. Plugging in $\tilde{x}_m(i)$ and $\tilde{x}_n(i)^*$, the elements of $\hat{\mathbf{R}}$ are

$$\begin{aligned}\hat{r}_{m,n} &= \frac{1}{N} \sum_{i=1}^N \tilde{x}_m(i) \tilde{x}_n(i)^* \\ &= \frac{1}{N} \sum_{i=1}^N |s(i)|^2 \tilde{a}_m \tilde{a}_n^* + s(i) \tilde{a}_m e_n(i)^* + s(i)^* \tilde{a}_n^* e_m(i) + e_m(i) e_n(i)^*.\end{aligned}\quad (2.55)$$

It can be easily seen that

$$\mathbb{E}\{\hat{r}_{m,n}\} = P \tilde{a}_m \tilde{a}_n^* + \sigma^2 \delta_{m,n} = \tilde{r}_{m,n} \quad (2.56)$$

which corresponds to (2.19), so $\hat{\mathbf{R}}$ is unbiased. Hence, also the phases of the elements are unbiased.

When the SNR is high and/or the number of snapshots is large such that the estimation error of $\hat{\mathbf{R}}$ is small [Tre85], we can employ a first-order approximation of

$$\begin{aligned}\frac{\hat{r}_{m,n}}{r_{m,n}} &= \frac{|\hat{r}_{m,n}|}{|r_{m,n}|} e^{j(\angle \hat{r}_{m,n} - \angle r_{m,n})} \\ &= (1 + \zeta_{m,n}) e^{j\epsilon_{m,n}} \\ &\approx (1 + \zeta_{m,n})(1 + j\epsilon_{m,n}) \approx 1 + \zeta_{m,n} + j\epsilon_{m,n}\end{aligned}$$

where $\zeta_{m,n} = |\hat{r}_{m,n}|/|r_{m,n}| - 1$ and

$$\epsilon_{m,n} = \angle \hat{r}_{m,n} - \angle r_{m,n} \approx \text{Im} \left\{ \frac{\hat{r}_{m,n}}{r_{m,n}} \right\} \quad (2.57)$$

represents the phase estimation error. It can be easily seen that $\epsilon_{m,n} = 0$ for $m = n$. Hence, we focus on the case $m \neq n$ in the following. Using (2.55) and (2.56), we have

$$\text{Im} \left\{ \frac{\hat{r}_{m,n}}{r_{m,n}} \right\} = \frac{1}{PN} \sum_{i=1}^N \text{Im} \{ s(i) \tilde{a}_n e_n(i)^* + s(i)^* \tilde{a}_m^* e_m(i) + \tilde{a}_m^* \tilde{a}_n e_m(i) e_n(i)^* \}.\quad (2.58)$$

Let us define

$$\gamma_{m,n} = \frac{1}{PN} \sum_{i=1}^N s(i) \tilde{a}_n e_n(i)^* + s(i)^* \tilde{a}_m^* e_m(i) + \tilde{a}_m^* \tilde{a}_n e_m(i) e_n(i)^*. \quad (2.59)$$

Then, for $m \neq n$ and $k \neq l$, we can calculate

$$\begin{aligned} \mathbb{E}\{\gamma_{m,n} \gamma_{k,l}^*\} &= \frac{1}{(PN)^2} \sum_{i=1}^N \sum_{q=1}^N \{P\delta_{i,q} \tilde{a}_n \tilde{a}_l^* \sigma^2 \delta_{n,l} + P\delta_{i,q} \tilde{a}_m^* \tilde{a}_k \sigma^2 \delta_{m,k} \\ &\quad + \tilde{a}_m^* \tilde{a}_n \tilde{a}_k \tilde{a}_l^* \sigma^4 \delta_{n,l} \delta_{m,k} \delta_{i,q}\} \\ &= \frac{1}{P^2 N} \{P\sigma^2 (\delta_{n,l} + \delta_{m,k}) + \sigma^4 \delta_{n,l} \delta_{m,k}\} \end{aligned} \quad (2.60)$$

where we have used that for white circular complex Gaussian random processes with zero mean [And03], we have

$$\mathbb{E}\{e_m(i) e_n(q)^*\} = \sigma^2 \delta_{i,q} \delta_{m,n}, \quad \mathbb{E}\{e_m(i) e_n(q)\} = 0$$

any third-order terms are zero, and

$$\mathbb{E}\{e_m(i) e_n(i)^* e_k(q)^* e_l(q)\} = \sigma^4 (\delta_{m,n} \delta_{k,l} + \delta_{i,q} \delta_{m,k} \delta_{n,l}).$$

Note that (2.60) is non-zero only for $l = n$ or $k = m$.

Likewise, we can calculate

$$\begin{aligned} \mathbb{E}\{\gamma_{m,n} \gamma_{k,l}\} &= \frac{1}{(PN)^2} \sum_{i=1}^N \sum_{q=1}^N \{P\delta_{i,q} \tilde{a}_n \tilde{a}_k^* \sigma^2 \delta_{n,k} + P\delta_{i,q} \tilde{a}_m^* \tilde{a}_l \sigma^2 \delta_{m,l} \\ &\quad + \tilde{a}_m^* \tilde{a}_n \tilde{a}_k^* \tilde{a}_l \sigma^4 \delta_{n,k} \delta_{m,l} \delta_{i,q}\} \\ &= \frac{1}{P^2 N} \{P\sigma^2 (\delta_{n,k} + \delta_{m,l}) + \sigma^4 \delta_{n,k} \delta_{m,l}\} \end{aligned} \quad (2.61)$$

which is non-zero only for $n = k$ or $m = l$.

Note that (2.60) and (2.61) cannot be simultaneously non-zero for $m \neq n$ and $k \neq l$. Moreover, since the expressions in (2.60) and (2.61) are real-valued, it can be easily seen that

$$\begin{aligned} \mathbb{E}\{\gamma_{m,n} \gamma_{k,l}^*\} &= \mathbb{E}\{\text{Re}[\gamma_{m,n}] \text{Re}[\gamma_{k,l}]\} + \mathbb{E}\{\text{Im}[\gamma_{m,n}] \text{Im}[\gamma_{k,l}]\} \\ \mathbb{E}\{\gamma_{m,n} \gamma_{k,l}\} &= \mathbb{E}\{\text{Re}[\gamma_{m,n}] \text{Re}[\gamma_{k,l}]\} - \mathbb{E}\{\text{Im}[\gamma_{m,n}] \text{Im}[\gamma_{k,l}]\} \end{aligned}$$

which, by subtracting the latter two equations, yields

$$\mathbb{E}\{\text{Im}[\gamma_{m,n}] \text{Im}[\gamma_{k,l}]\} = \frac{1}{2} (\mathbb{E}\{\gamma_{m,n} \gamma_{k,l}^*\} - \mathbb{E}\{\gamma_{m,n} \gamma_{k,l}\}). \quad (2.62)$$

From (2.57) and (2.59), we have $\epsilon_{m,n} \approx \text{Im}\{\gamma_{m,n}\}$. Consequently, (2.62) approximately equals $\text{E}\{\epsilon_{m,n}\epsilon_{k,l}\}$.

In summary, since $\hat{\mathbf{R}}$ is unbiased, $\epsilon_{m,n}$ has zero mean. Moreover, when the SNR is high and/or the number of snapshots is large, the covariance between the phases of matrix elements is

$$\text{E}\{\epsilon_{m,n}\epsilon_{k,l}\} \approx \begin{cases} \frac{\sigma^2}{2PN} & \text{if } n = l \cap m \neq k \\ \frac{\sigma^2}{2PN} & \text{if } n \neq l \cap m = k \\ \frac{\sigma^2}{PN} + \frac{\sigma^4}{2P^2N} & \text{if } n = l \cap m = k \\ -\frac{\sigma^2}{2PN} & \text{if } n = k \cap m \neq l \\ -\frac{\sigma^2}{2PN} & \text{if } n \neq k \cap m = l \\ -\frac{\sigma^2}{PN} - \frac{\sigma^4}{2P^2N} & \text{if } n = k \cap m = l \\ 0 & \text{otherwise.} \end{cases}$$

2.A.2 MAP-NSF

This approach uses the fact that the ML criterion, required for MAP estimation, is asymptotically, for large N , equivalent to the NSF criterion [VS94]. For a single source, the latter is given by

$$V_{\text{NSF}}(\psi_x, \psi_y, \boldsymbol{\varphi}) = N \tilde{\mathbf{a}}^H \hat{\mathbf{U}}_n \hat{\mathbf{U}}_n^H \tilde{\mathbf{a}} \hat{w}$$

where $\hat{\mathbf{U}}_n$ is the estimated noise subspace, obtained from an eigendecomposition of $\hat{\mathbf{R}}$, and

$$\hat{w} = \frac{1}{\hat{\sigma}^2} \frac{|\mathbf{a}(\hat{\psi}_x, \hat{\psi}_y)^H \hat{\mathbf{u}}_s|^2 (\hat{\lambda}_s - \hat{\sigma}^2)^2}{M^2 \hat{\lambda}_s}$$

where $\hat{\sigma}^2$ is the average of the $M - 1$ smallest eigenvalues, $\hat{\psi}_x$ and $\hat{\psi}_y$ are initial DOA estimates, e.g. obtained from the global maximum of (2.52), $\hat{\mathbf{u}}_s$ is the estimated signal eigenvector, and $\hat{\lambda}_s$ is its respective eigenvalue. In the considered case, the MAP-NSF criterion is given by

$$V(\psi_x, \psi_y, \boldsymbol{\varphi}) = V_{\text{NSF}}(\psi_x, \psi_y, \boldsymbol{\varphi}) + \frac{1}{2N\sigma_\varphi^2} \boldsymbol{\varphi}^T \boldsymbol{\varphi}. \quad (2.63)$$

Assuming $\boldsymbol{\varphi}$ is small, a local first-order approximation of $\tilde{\mathbf{a}}$ is possible around $\boldsymbol{\varphi} = \mathbf{0}$,

$$\tilde{\mathbf{a}} \approx \mathbf{a} + \mathbf{D}_\varphi \boldsymbol{\varphi}$$

with nominal steering vector $\mathbf{a} = \mathbf{a}(\psi_x, \psi_y)$, and

$$\mathbf{D}_\varphi = \left[\frac{\partial \tilde{\mathbf{a}}}{\partial \varphi_2}, \dots, \frac{\partial \tilde{\mathbf{a}}}{\partial \varphi_M} \right]_{\boldsymbol{\varphi}=\mathbf{0}} = j \text{diag}\{\mathbf{a}\} \mathbf{L}_1^T.$$

This approximation allows to concentrate the MAP-NSF criterion in (2.63) with respect to error parameter φ [VS94]. The DOA estimates are obtained from the global minimum of

$$V(\psi_x, \psi_y) = \mathbf{a}^H \hat{\mathbf{M}} \mathbf{a} - \hat{\mathbf{f}}^H \hat{\mathbf{\Gamma}} \hat{\mathbf{f}}$$

where $\hat{\mathbf{M}} = \hat{w} \hat{\mathbf{U}}_n \hat{\mathbf{U}}_n^H$, and

$$\begin{aligned} \hat{\mathbf{\Gamma}} &= \text{Re}\{\mathbf{D}_\varphi^H \hat{\mathbf{M}} \mathbf{D}_\varphi + \frac{1}{2N\sigma_\varphi^2} \mathbf{I}_{M-1}\} \\ \hat{\mathbf{f}} &= \text{Re}\{\mathbf{D}_\varphi^H \hat{\mathbf{M}} \mathbf{a}\}. \end{aligned}$$

The phase estimates are obtained by $\hat{\varphi} = -\hat{\mathbf{\Gamma}} \hat{\mathbf{f}}$.

Chapter 3

Automotive radar

In this chapter, we consider the problem of high-resolution DOA estimation in automotive radar. A brief background of automotive radar applications for modern driver assistance systems is given in Section 3.1. We provide a description of a typical automotive radar system in Section 3.2, along with the measurement model and a possible pre-processing, which results in processing cells according to range and relative velocity, each represented by a single snapshot. In many cases, multiple targets can be distinguished by their range and/or relative velocity, so that each processing cell only contains a single target. We focus on the case when two targets are superposed in a processing cell and describe practical use cases. For the potential two-target model, an optimal approach for DOA estimation and detection, based on ML estimation and a GLRT, is presented in Section 3.3. Results with real data in controlled experiments with one and two corner reflectors are presented. In Section 3.4, a discussion and outline of the remaining chapters is given.

3.1 Background

Some parts of the automotive radar background are taken from [Win10]. More and more cars are equipped with advanced driver assistance systems, which use various sensors to determine the environment of the car. From an identified traffic situation, a driver assistance system regulates the behavior of the car, instructs the driver, or warns the driver in dangerous situations. An overview is provided in [WHW09]; one can distinguish:

- Comfort applications, e.g. adaptive cruise control (ACC) or, more specifically, full speed range adaptive cruise control (FSRA) [ISO09, WHW09]. Here, the driver assistance system regulates the speed of the car to a desired level if this is allowed by the traffic situation. Otherwise, the speed is adapted to the traffic situation.
- Safety applications, e.g. collision avoidance systems [Jon01, Hof08], with the aim to reduce the stopping distance in a dangerous traffic situation. Means to achieve this can range from prefilling the brake to an autonomous emergency braking. Some other safety applications are lane departure warning, lane change assistant (LCA), or blind spot detection, to name a few [WHW09].

Often driver assistance systems use radar sensors to determine the environment. These work reliably even in bad weather conditions, and can provide accurate measurements of the range, or radial distance, and the radial relative velocity of multiple targets. Typical frequency bands for automotive radar are around 24 GHz and 77 GHz. To also measure the lateral position of a target, a mechanically scanning directional antenna, or an antenna array with digital beamforming can be applied. For the latter variant, planar microstrip antennas, or patch antennas, are an implementation with low costs and small installation size. By measuring the phases at an array of antennas in horizontal direction, one can determine the DOA of a target. For the described collision avoidance or FSRA application, it is essential to accurately estimate the lateral position, and to be able to resolve multiple closely spaced targets. For array systems with limited aperture, this can be achieved with high-resolution DOA estimation.

3.2 Radar system

Following [Win10], we consider the exemplary radar system as depicted in Figure 3.1.

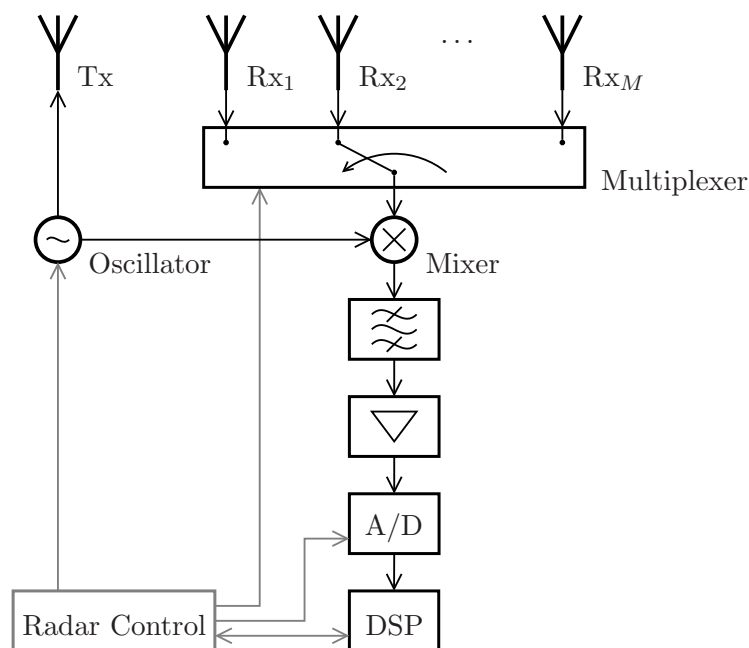


Figure 3.1. Hardware configuration of an exemplary radar system with a single transmit (Tx) antenna and multiple receive (Rx) antennas, with sequential antenna recording and stretch pulse compression [Win10].

It consists of a single transmit antenna and multiple receive antennas. All antennas are implemented as patch arrays with the same directivity in azimuth and elevation an-

gle. The M receive antennas form a ULA with element spacing d . To reduce hardware cost, a sequential antenna recording strategy is employed. This involves a single receive path and a high-frequency multiplexer, which can cyclically select the receive antennas. The receive path consists of a real-valued correlation mixer, a bandpass filter, an amplifier, and an analog-to-digital (A/D) converter. The sampled radar measurements are processed in the digital signal processing (DSP) unit. A radar control unit actuates the voltage-controlled oscillator for pulse waveform generation, the high-frequency multiplexer, and the A/D converter.

In contrast to digital pulse compression, the depicted radar system performs a stretch pulse compression, which is done partly in the analog domain by means of down-mixing with the transmitted waveform [Sko08, Ch. 8], [Ric05], and in the digital domain by means of spectrum analysis. For targets located within a relatively small range window, this allows to use a sampling frequency much smaller than the bandwidth, without loss of the range resolution.

3.2.1 Radar measurement model

The description of the radar measurement model is loosely based on [Win10], where some parts are also taken from [Win07, LKK04]. The transmitted waveform is a linear frequency modulated pulse, commonly referred to as chirp, generated from the voltage-controlled oscillator,

$$x_T(t) = \cos[2\pi\varphi_T(t)], \quad \varphi_T(t) = f_c t + \alpha t^2, \quad t \in [0, T]$$

where f_c is the carrier frequency, $\alpha = B/(2T)$, B is the pulse bandwidth, and T is the pulse duration. At a reference antenna, the received signal, which has been reflected by an object at range r with radial relative velocity v , is given by

$$x_R(t) = A_R \cos[2\pi\varphi_R(t)], \quad \varphi_R(t) = \varphi_T(t - \tau)$$

where A_R is an attenuation factor,

$$\tau = \frac{2}{c}(r + vt) \tag{3.1}$$

is the radar two-way propagation delay due to the reflection from of a moving target, and c is the speed-of-light. The real-valued correlation mixer acts as a multiplier with output $x_T(t)x_R(t)$, which can be evaluated using the identity

$$2 \cos(x) \cos(y) = \cos(x + y) + \cos(x - y).$$

Table 3.1. System parameters of exemplary mid-range radar (MRR) and short range radar (SRR) systems, of which experimental results are presented.

	MRR	SRR
Carrier frequency f_c	24.15 GHz	
Pulse duration T	7.68 μ s	
Pulse bandwidth B	100 MHz	
Fast time sampling interval T_S	25 ns	
Number of fast time samples N_S	256	
Pulse repetition interval T_P	10 μ s	
Number of pulses N_P	128	256
Number of antennas M	8 (provisional 7)	
Antenna spacing d	15 mm	6.2 mm
Antenna HPBW	40°	120°

The first term corresponds to the upper sideband of the mixer output, which is rejected by the bandpass filter. Thus, the intermediate frequency (IF) signal after bandpass filtering and amplification is

$$\begin{aligned}
 x_{\text{IF}}(t) &= A \cos[2\pi\varphi_{\text{IF}}(t)], & \varphi_{\text{IF}}(t) &= \varphi_{\text{T}}(t) - \varphi_{\text{R}}(t) \\
 & & &= f_c t + \alpha t^2 - f_c(t - \tau) - \alpha(t - \tau)^2 \\
 & & &= f_c \tau + 2\alpha\tau t - \alpha\tau^2
 \end{aligned}$$

where A is an amplitude factor. Since $\tau \ll T$, the last term of $\varphi_{\text{IF}}(t)$ can be neglected [Win07]. Plugging in τ from (3.1) yields

$$\varphi_{\text{IF}}(t) \approx \frac{2f_c r}{c} + \left(\frac{4\alpha r}{c} + \frac{2f_c v}{c} \right) t + \frac{4\alpha v}{c} t^2 \quad (3.2)$$

where the first term is a constant phase, the term in brackets is a frequency according to the propagation delay and the Doppler shift [Win07, Ric05], and the term with t^2 corresponds to a linear frequency variation and can also be neglected. For small pulse durations T , and thus large values of α , the frequency term is dominated by $4\alpha r/c$. For instance, given the system parameters of the exemplary radar systems in Table 3.1, one can calculate $4\alpha/(2f_c) \approx 10^3 \gg 1$.

Consequently, range r is determined from the frequency of $x_{\text{IF}}(t)$. In practice, one is also interested in relative velocity v and azimuth angle ϕ , as defined in Figure 2.1 for a ULA in x -direction. Towards this end, N_P pulses are repeated with pulse repetition interval T_P , for all M antennas. Before transmission, the multiplexer cyclically selects the corresponding receive antenna. In total, this results in MN_P pulses in a coherent measurement cycle. During this period, parameters r , v , and ϕ are assumed to be constant. In the considered case with multiple pulses and antennas, and when performing

fast time sampling, $t = T_S n_S$ at N_S instances, (3.2) can be extended to

$$\begin{aligned} \varphi_{\text{IF}}(n_S, n_S, m; r, v, \phi, \xi) & \quad (3.3) \\ \approx \underbrace{\frac{4\alpha r}{c} T_S}_{F_r} n_S + \underbrace{\frac{2f_c v}{c} M T_P}_{F_v} n_P + \left(\frac{2f_c v}{c} T_P + \underbrace{\frac{f_c d \sin(\phi)}{c}}_{F_\phi} \right) (m - 1) + \xi \end{aligned}$$

for

$$n_S = 0, \dots, N_S - 1, \quad n_P = 0, \dots, N_P - 1, \quad m = 1, \dots, M.$$

Non-dominant terms are neglected, the remaining phase terms correspond to harmonic oscillations with respect to sample, pulse and antenna variable n_S , n_P , and m , respectively. The corresponding normalized frequencies F_r , F_v , and F_ϕ directly depend on the parameters of interest [Win10], as indicated in (3.3). Due to the sequential antenna recording, one has to correct the frequency of the antenna variable by $-F_v/M$. Constant and almost constant phase terms are summarized by ξ .

Using the superposition principle and the expression from (3.3), the approximate signal model for K targets, with parameters r_k , v_k , ϕ_k , A_k and ξ_k , corresponding to range, relative velocity, DOA, amplitude and phase, respectively, is given by

$$x_{\text{IF}}(n_S, n_P, m) = \sum_{k=1}^K A_k \cos[2\pi\varphi_{\text{IF}}(n_S, n_P, m; r_k, v_k, \phi_k, \xi_k)] + e_{\text{IF}}(n_S, n_P, m) \quad (3.4)$$

with noise term $e_{\text{IF}}(n_S, n_P, m)$. The sampled radar data from a coherent measurement cycle can be arranged in a radar data cube, as depicted in Figure 3.2. From this data cube, the parameters of interest can be determined by three-dimensional spectrum analysis, e.g. based on the three-dimensional periodogram [Win10].

We note that phase parameter ξ_k is arbitrary and therefore not of interest. It can be modeled by a uniformly distributed random variable. In contrast, amplitude parameter A_k mainly depends on path loss attenuation $1/r_k^2$ and on the radar cross section (RCS) of the reflecting object, and can be used for a rough classification of the object type [WHW09]. Depending on the directivity of the antennas in elevation angle, vertical multipath with the ground can cause signal cancellation, which further affects the received amplitude [Büh08]. Due to the RCS fluctuations of objects composed of multiple scatterers, A_k can be modeled by a log-normal or chi-square (χ^2) distributed random variable [Sko08]. In automotive radar at 24 GHz carrier frequency, typical average RCS values can vary between 0.01 m^2 for pedestrians, and 100 m^2 for large trucks [WHW09].

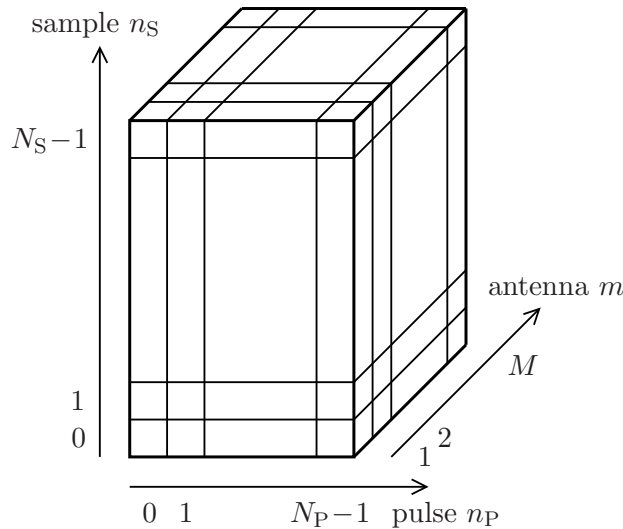


Figure 3.2. Coherent radar measurements from N_S samples, N_P pulses and M antennas, arranged in radar data cube.

3.2.2 Radar pre-processing

For every coherent measurement cycle, the aim of the radar signal processing is to generate a target list, which contains the estimated parameters of interest of all targets in the scene. After the parameter estimation, a tracking and data association procedure is applied to the target lists of consecutive cycles, in order to filter the estimates and combine connected targets to objects [Büh08, WHW09, RSH10]. Finally, relevant objects are selected for the realization of a certain driver assistance application. In this thesis, we focus on the parameter estimation part, especially DOA estimation based on extracted snapshots from detected processing cells according to range and relative velocity. This section deals with the radar pre-processing for extracting snapshots.

A practical approach for frequency estimation is spectrum analysis. Consider a discrete Fourier transform (DFT) of (3.4) with respect to the sample and pulse variable, which can be efficiently computed with an FFT,

$$X_{\text{IF}}(i_r, i_v, m) = \sum_{n_P=0}^{N_P-1} \sum_{n_S=0}^{N_S-1} w_P(n_P) w_S(n_S) x_{\text{IF}}(n_S, n_P, m) e^{-j2\pi i_r n_S / N_S} e^{-j2\pi i_v n_P / N_P} \quad (3.5)$$

for

$$i_r = 0, \dots, I_r - 1, \quad i_v = 0, \dots, I_v - 1$$

where $w_S(n)$ and $w_P(n)$ are window functions of lengths N_S and N_P , respectively, normalized such that their root mean square value is one. Windowing can be employed

for more sidelobe suppression at the cost of a wider mainlobe [Har78]. The DFT indices according to range and relative velocity are related to the normalized frequency variables, and the respective parameters of interest, by

$$i_r \simeq F_r N_S = \frac{4\alpha r}{c} T_S N_S, \quad i_v \simeq F_v N_P = \frac{2f_c v}{c} M T_P N_P$$

where \simeq means equivalent after rounding. Since the downconverted and sampled radar measurements are real-valued, and have been filtered by a bandpass filter with a finite transition region, it is practical to consider $I_r < N_S/2$. After the first Fourier transform, the result is complex-valued, so that the Doppler spectrum can be considered for all variables $I_v = N_P$. The widths of the processing cells according to range and relative velocity, respectively, are

$$\Delta_r = \frac{c}{4\alpha T_S N_S}, \quad \Delta_v = \frac{c}{2f_c M T_P N_P}.$$

For the SRR system from Table 3.1, we obtain $\Delta_r \approx 1.8$ m and $\Delta_v \approx 0.3$ m/s. When using $I_r = 100$, the maximum measurable range is 180 m, the width of the unambiguous interval for the relative velocity is 77.64 m/s, which corresponds to roughly 280 km/h. The radar data cube after the two DFTs is depicted in Figure 3.3.

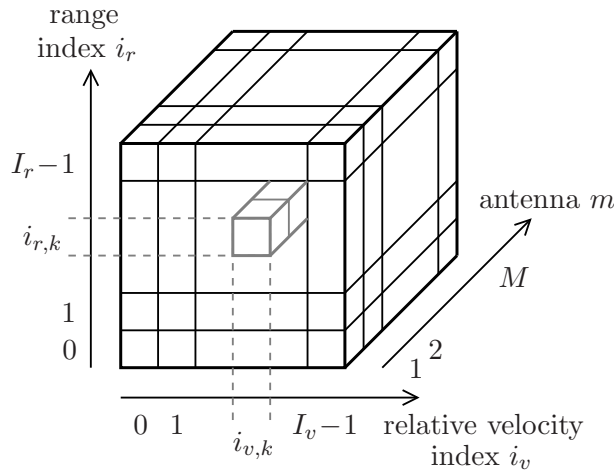


Figure 3.3. Radar data cube after DFTs with respect to sample and pulse variable, $X_{\text{IF}}(i_r, i_v, m)$. An extracted snapshot at range index $i_{r,k}$ and relative velocity index $i_{v,k}$ is indicated.

The squared magnitude of (3.5) shows peaks at indices i_r and i_v , corresponding to parameters r_k and v_k , respectively. Target detection involves a comparison with a threshold, which can be determined according to the constant false alarm rate principle [Roh83, Sko08]. In [Win06], an approach based on rank order filtering with low computational complexity is described. To determine estimates \hat{r}_k and \hat{v}_k , an interpolation strategy in the neighborhood of the respective peak can be applied.

When all targets in the scene can be resolved by their range and/or relative velocity, the resulting approximate model for the processing cell at indices $i_{r,k}$ and $i_{v,k}$, containing target k , is

$$X_{\text{IF}}(i_{r,k}, i_{v,k}, m) = \tilde{s}_k e^{j\psi_k(m-1)} + E_{\text{IF}}(i_{r,k}, i_{v,k}, m), \quad m = 1, \dots, M \quad (3.6)$$

where

$$|\tilde{s}_k| \approx N_s N_p A_k, \quad \psi_k = 2\pi F_\phi = \kappa d \sin(\phi_k)$$

are the amplitude after DFT pre-processing, and the electrical angle after correction by $-F_{v,k}/M$, respectively. Noise term $E_{\text{IF}}(i_{r,k}, i_{v,k}, m)$ comprises measurement noise and model approximation errors. For notational convenience in the following, model (3.6) is rewritten in vector notation. Omitting target index k , the resulting snapshot model is

$$\mathbf{x} = s_0 \mathbf{a}(\psi_0) + \mathbf{e} \quad (3.7)$$

where ψ_0 and s_0 , respectively, are the DOA parameter and complex-valued target response parameter of the corresponding processing cell with target k , $\mathbf{a}(\psi)$ is the steering vector, and \mathbf{e} is the noise vector. Without loss of generality, we define

$$\mathbf{a}(\psi) = e^{-j(M-1)\psi/2} [1, e^{j\psi}, \dots, e^{j(M-1)\psi}]^T \quad (3.8)$$

so that it is centro-Hermitian and we have $\mathbf{J}_M \mathbf{a}(\psi)^* = \mathbf{a}(\psi)$, where \mathbf{J}_M is an exchange matrix of size M , with ones on the anti-diagonal and zeros elsewhere. This property simplifies analysis and can be exploited for the derivation of fast algorithms. We assume a perfectly calibrated array, i.e. the imperfections after off-line calibration [TF09] are negligible when compared to the measurement noise. The application of autocalibration to automotive radar is left for future work.

3.2.3 Array processing problem: potential two-target case

In the considered radar pre-processing, the received data is divided into processing cells according to range and relative velocity, each represented by a single snapshot. In most situations, the targets in the scene can be resolved by their range and/or relative velocity. Thus, only a single target is present in each processing cell and model (3.7) applies. However, there are some situations, in which two targets have similar range and relative velocity, so that they fall into the same processing cell. In this case, the snapshot model is

$$\mathbf{x} = s_1 \mathbf{a}(\psi_1) + s_2 \mathbf{a}(\psi_2) + \mathbf{e} \quad (3.9)$$

where $\psi_1 < \psi_2$, s_1 , and s_2 , respectively, are the DOA parameters and complex-valued target response parameters of the two targets. These situations occur only rarely, however, when not detected and processed adequately such that the targets are resolved, the target localization can be false. Some practical scenarios are:

- Two vehicles of interest are driving parallelly, at similar range and relative velocity, possibly on the outer lanes of a motorway with three lanes. To track both objects individually in an ACC application, it is necessary to resolve them. This scenario was used as a motivation in [Sch10].
- The observed vehicle is driving on an outer lane of the motorway, possibly in a construction site, and close to a reflecting surface such as a metallic or concrete guardrail. In this case, the radar returns from the object consist of a direct path and an indirect specular path, which gives rise to a ghost target. If this horizontal multipath is not detected and resolved, the target seems to be pulled towards the guardrail. This scenario is relevant in ACC or LCA applications, it has been analyzed in [HY11a, HY11b] and considered with experimental data in [HZ11a].
- At close distances, one can observe multiple scattering centers of typical vehicles. This has been investigated in [BY06, BY07] and [Eng11]. If multiple scattering centers are resolved, orientation and elongation information can be extracted.

For practical reasons, we focus on the case with at most two targets per processing cell. Situations with three targets are considered as unlikely and are therefore not addressed here. Under the assumption that there are at most two targets in an unresolved cluster, an extension to the case with multiple targets is possible, e.g. using approaches in the spatial Fourier domain. This is left for future work.

The problem formulation is posed as follows: given snapshot \mathbf{x} from a detected processing cell, whose power is significantly above the noise level, decide between

$$\begin{aligned} D = 1 : \mathbf{x} &= s_0 \mathbf{a}(\psi_0) + \mathbf{e} \\ D = 2 : \mathbf{x} &= s_1 \mathbf{a}(\psi_1) + s_2 \mathbf{a}(\psi_2) + \mathbf{e} \end{aligned}$$

and estimate the respective parameters. In the single snapshot case, and particularly in the radar context, it is reasonable to assume a deterministic signal model, i.e. according to the respective model in (3.7) and (3.9), parameters

$$\begin{aligned} \boldsymbol{\eta}_1 &= [\psi_0, s_0] \\ \boldsymbol{\eta}_2 &= [\psi_1, \psi_2, s_1, s_2] \end{aligned}$$

are considered as unknown deterministic. For simplicity, \mathbf{e} is assumed to be spatially white, circular complex Gaussian distributed with zero mean and variance σ^2 , which is considered as a nuisance parameter. In this case, the probability density function (pdf) of \mathbf{x} given the unknown parameters is

$$p_k(\mathbf{x}|\boldsymbol{\eta}_k, \sigma^2) = \frac{1}{(\pi\sigma^2)^M} e^{-\|\mathbf{x}-\mathbf{x}_k(\boldsymbol{\eta}_k)\|^2/\sigma^2}, \quad k = 1, 2 \quad (3.10)$$

where

$$\begin{aligned} \mathbf{x}_1(\boldsymbol{\eta}_1) &= s_0 \mathbf{a}(\psi_0) \\ \mathbf{x}_2(\boldsymbol{\eta}_2) &= s_1 \mathbf{a}(\psi_1) + s_2 \mathbf{a}(\psi_2). \end{aligned}$$

We note that the assumption of additive and spatially white noise may be simplistic in practice. It may occur that targets from other processing cells leak into the processing cell under consideration, creating weak additional targets. Moreover, diffuse noise sources may create spatially correlated noise. A more realistic model can be considered by estimating the noise/clutter characteristics from neighboring processing cells. This approach is not considered here and left for future work.

In some instances, another parameterization of the model with two targets is appropriate. Instead of directly using the parameters in $\boldsymbol{\eta}_2$, we define angular separation, relative phase and power ratio, respectively, as

$$\delta = \psi_2 - \psi_1, \quad \varphi = \angle s_2 - \angle s_1, \quad \rho = \frac{|s_2|^2}{|s_1|^2}. \quad (3.11)$$

3.3 Optimal single-snapshot array processing

Unlike array processing with multiple snapshots, the single snapshot treatment has not received much attention in the literature. In the context of automotive radar, it is also studied in [HY10]. In [How99], an approach is proposed for two closely spaced targets, based on the knowledge of the DOA centroid and a first-order approximation of the MUSIC projector. A Bayesian framework is considered in [RB97]. An ESPRIT method is presented in [THG09] which effectively exploits the ULA structure. In this section, we present an optimal approach for DOA estimation and detection in the potential two-target case, based on ML estimation and a GLRT. The limitations in terms of accuracy and resolution are analyzed specifically for the single-snapshot case. Results with real data in controlled experiments with one and two corner reflectors are presented.

3.3.1 Parameter estimation

For DOA estimation, we follow an optimal ML approach. We do not consider the BF due to its limited resolution. We also do not consider subspace methods for the reasons, pointed out in Section 2.2.4.

3.3.1.1 Maximum likelihood

ML is an intuitive approach for parameter estimation. The estimates are obtained by maximizing the so-called likelihood function, which is equivalent to the pdf of the data, given the unknown parameters, as defined in (3.10). Thus, we have

$$[\hat{\boldsymbol{\eta}}_k, \hat{\sigma}_k^2] = \arg \max_{\boldsymbol{\eta}_k, \sigma^2} p_k(\mathbf{x}|\boldsymbol{\eta}_k, \sigma^2), \quad k = 1, 2. \quad (3.12)$$

In the deterministic signal case, and with Gaussian noise, ML estimation is equivalent to nonlinear LS, as described in Section 2.2.2. For convenience, we restate the corresponding estimators for the parameters in $\boldsymbol{\eta}_k$ and σ^2 . The optimization problem in (3.12) can be concentrated with respect to the noise variance and the target response parameters. Towards this end, when the first derivative of $p_k(\mathbf{x}|\boldsymbol{\eta}_k, \sigma^2)$ in (3.10) with respect to σ^2 is equated to zero, we obtain

$$\sigma^2 = \frac{1}{M} \|\mathbf{x} - \mathbf{x}_k(\boldsymbol{\eta}_k)\|^2. \quad (3.13)$$

Plugging (3.13) back into (3.12) yields the nonlinear LS criterion

$$\hat{\boldsymbol{\eta}}_k = \arg \min_{\boldsymbol{\eta}_k} \|\mathbf{x} - \mathbf{x}_k(\boldsymbol{\eta}_k)\|^2. \quad (3.14)$$

Since $\mathbf{x}_k(\boldsymbol{\eta}_k)$ is a linear function of the target response parameters, (3.14) can be solved explicitly for s_0 , or s_1 and s_2 . For $k = 2$, we have

$$\mathbf{s} = [s_1, s_2]^T = (\mathbf{A}^H \mathbf{A})^{-1} \mathbf{A}^H \mathbf{x}, \quad \mathbf{A} = [\mathbf{a}(\psi_1), \mathbf{a}(\psi_2)]. \quad (3.15)$$

Plugging (3.15) back into (3.14), and after some manipulations, we obtain

$$[\hat{\psi}_1, \hat{\psi}_2] = \arg \max_{\psi_1, \psi_2} \underbrace{\|\mathbf{P}_A(\psi_1, \psi_2) \mathbf{x}\|^2}_{c(\psi_1, \psi_2)} \quad (3.16)$$

where

$$\mathbf{P}_A(\psi_1, \psi_2) = \mathbf{A}(\mathbf{A}^H \mathbf{A})^{-1} \mathbf{A}^H.$$

The optimization of two-dimensional objective function $c(\psi_1, \psi_2)$ needs to be numerical and is generally computationally intensive. One can consider a brute force search over a selected grid of values for ψ_1 and ψ_2 , followed by an interpolation in the neighborhood of the optimum to obtain the final estimate [TF09, Ch. 1]. A possible interpolation strategy is described in Appendix 3.A.1. Moreover, a practicable implementation is proposed in Chapter 5, which additionally involves a simplified calculation of the objective function and a delimited search range. Having determined $\hat{\psi}_1$ and $\hat{\psi}_2$, one can calculate $\hat{\mathbf{s}}$ using (3.15), and $\hat{\sigma}_2^2$ using (3.13).

For $k = 1$, (3.15) reduces to

$$s_0 = \frac{1}{M} \mathbf{a}(\psi_0)^H \mathbf{x} \quad (3.17)$$

and (3.16) reduces to

$$\hat{\psi}_0 = \arg \max_{\psi} \underbrace{\frac{1}{M} |\mathbf{a}(\psi)^H \mathbf{x}|^2}_{P_{\text{BF}}(\psi)}. \quad (3.18)$$

The objective function $P_{\text{BF}}(\psi)$ is termed BF spectrum, and can be efficiently calculated using an FFT. Again, the final estimate can be obtained by an interpolation in the neighborhood of the optimum, as described in Appendix 3.A.2. Having determined $\hat{\psi}_0$, one can calculate \hat{s}_0 using (3.17), and $\hat{\sigma}_1^2$ using (3.13).

3.3.1.2 Accuracy and resolution

The estimation accuracy of an effectively implemented ML estimator is generally close to the CRB, provided the SNR is sufficiently high [TF09]. This even holds in the single-snapshot case, as demonstrated in the simulation results of Chapter 5. Thus, it appears reasonable to not only consider the CRB as a performance bound, but also as an optimistic indicator for the performance of an ML estimator.

In the case with a single snapshot, and for $k = 2$, the CRB matrix for parameters ψ_1 and ψ_2 from (3.9) is given by [SN89]

$$\mathbf{CRB} = \frac{\sigma^2}{2} \text{Re}\{(D^H [\mathbf{I}_M - \mathbf{P}_A] D) \odot (\mathbf{s} \mathbf{s}^H)^T\}^{-1} \quad (3.19)$$

where

$$D = [\mathbf{d}(\psi_1), \mathbf{d}(\psi_2)], \quad \mathbf{d}(\psi) = \frac{\partial \mathbf{a}(\psi)}{\partial \psi}$$

is a matrix of differential steering vectors, \mathbf{P}_A is the projection matrix onto the column span of \mathbf{A} , as defined in (3.15). The diagonal elements of \mathbf{CRB} represent lower bounds on the error variances of estimating ψ_1 and ψ_2 . Generally, these expressions depend

on the respective SNR, the number of array elements and the angular separation. Especially in the case with a single snapshot, they also critically depend on the relative phase between the target response parameters.

For $k = 1$, the CRB for parameter ψ_0 from (3.7) can be reduced to [SN89]

$$\text{CRB}_1 = \frac{\sigma^2}{|s_0|^2} \frac{6}{M(M^2 - 1)} \quad (3.20)$$

which only depends on the SNR and the number of array elements.

In the two-target case, a statistical resolution limit can be obtained by the following consideration. An intuitive requirement for two targets to be resolvable is that their angular separation δ is larger than the standard deviation of the estimation of ψ_1 and ψ_2 . When the estimation accuracy is determined using the CRB in (3.19), a statistical resolution limit is [Smi05]

$$\delta > \sqrt{[\mathbf{CRB}]_{1,1} + [\mathbf{CRB}]_{2,2}}. \quad (3.21)$$

In other words, two targets are resolvable, when their angular separation exceeds the standard deviation, according to the CRB, when estimating the difference between DOA parameters.

Before presenting an example, we comment on the considered error measure. In practice, one may be interested in DOA estimation errors in physical angle ϕ , in degrees. However, due to the nonlinear relation between electrical angle and physical angle $\psi = \kappa d \sin(\phi)$, the Rayleigh BW in physical angle depends on the true DOA parameters, and ULAs with different sensor spacings lead to different estimation errors in physical angle. Therefore, we consider an error measure in electrical angle, normalized by the respective Rayleigh BW. This can be directly converted to an approximate DOA estimation error in physical angle by multiplication with BW_ϕ . Using a first-order approximation, we have

$$\text{BW}_\phi \approx \frac{\text{BW}_\psi}{\kappa d \cos(\phi_0)}, \quad \text{BW}_\psi = \frac{2\pi}{M}. \quad (3.22)$$

where the true DOA parameters are assumed to lie around ϕ_0 .

An example is used to demonstrate the described limitations in terms of accuracy and resolution. We consider an 8-element ULA and targets of equal magnitude. First, in the single-target case, the CRB in (3.20) is calculated for varying SNR. Figure 3.4 (left) shows the obtained results. One can observe that the optimal average estimation error is below 5% of the Rayleigh BW already at 10 dB. Second, in the two-target

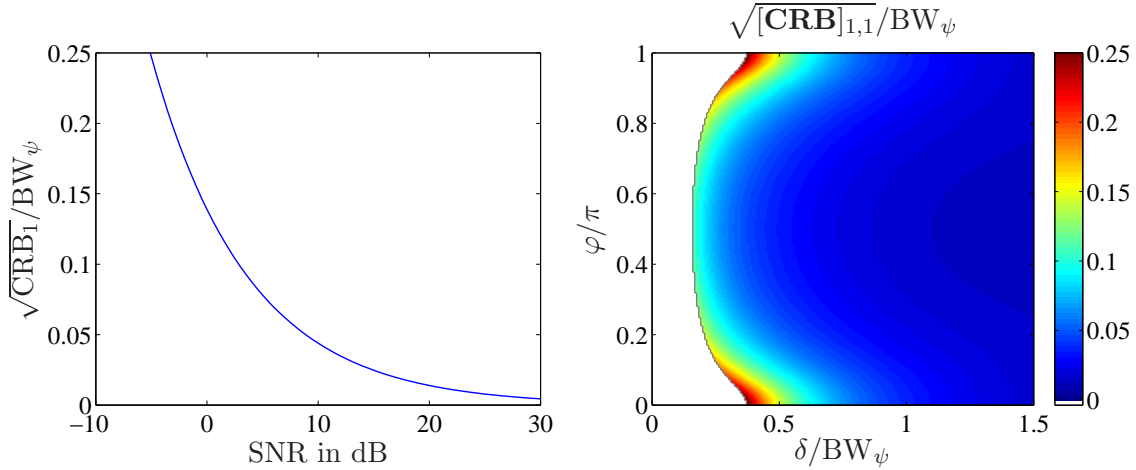


Figure 3.4. Limitations of DOA estimation with an 8-element ULA: CRB for a single target versus SNR (left), CRB for resolvable two-target cases at SNR = 20 dB versus angular separation δ and relative phase φ (right).

case and an SNR of 20 dB, the CRB matrix in (3.19) is calculated for varying angular separation δ and relative phase φ . For the first DOA parameter, Figure 3.4 (right) shows the obtained results, where the white area corresponds to the cases in which the targets are not resolvable according to (3.21). One can observe that above a certain angular separation, the targets are resolvable, and the optimal average estimation error decreases for increasing δ . Also, one can observe that when the relative phase is around 0 or π , the estimation accuracy is worse, and closely spaced targets are more difficult to resolve. These cases, respectively, correspond to the situations when there is perfectly constructive or destructive interference of wavefronts at the center of the ULA. We note that these situations generally depend on δ when the steering vector is not centered, i.e. defined differently as in (3.8).

3.3.2 Detection with generalized likelihood ratio test

The GLRT for deciding between the single-target and the two-target case, i.e. between models (3.7) and (3.9), is given by

$$T_{\text{GLRT}} = \frac{\max_{\boldsymbol{\eta}_2, \sigma^2} p_2(\mathbf{x}|\boldsymbol{\eta}_2, \sigma^2)}{\max_{\boldsymbol{\eta}_1, \sigma^2} p_1(\mathbf{x}|\boldsymbol{\eta}_1, \sigma^2)} > \gamma_{\text{GLRT}}$$

where $p_k(\mathbf{x}|\boldsymbol{\eta}_k, \sigma^2)$, $k = 1, 2$, as defined in (3.10), is equivalent to the likelihood function. When test statistic T_{GLRT} exceeds threshold γ_{GLRT} , the two-target case is considered more likely than the single-target case. The maximization is obtained by plugging in the respective ML estimates. By taking the logarithm, and after some manipulations,

the test can be simplified to

$$\log T_{\text{GLRT}} = \log p_2(\mathbf{x}|\hat{\boldsymbol{\eta}}_2, \hat{\sigma}_2^2) - \log p_1(\mathbf{x}|\hat{\boldsymbol{\eta}}_1, \hat{\sigma}_1^2) = M \log \hat{\sigma}_1^2 - M \log \hat{\sigma}_2^2 > \log \gamma_{\text{GLRT}} \quad (3.23)$$

where $\hat{\sigma}_1^2$ and $\hat{\sigma}_2^2$ are the noise variance estimates in the single-target and two-target cases, respectively, and can be determined using (3.13).

A suitable threshold can be obtained by fixing the false alarm rate to a certain level. Here, false alarm means the erroneous decision for the two-target case, when there is only a single target present. This generally requires the knowledge of the distribution of the test statistic under the hypothesis. Although there exist asymptotic expressions for the distribution of the log-likelihood ratio in the stochastic signal model [OVS93], there are no analytic expressions available for the considered case with a single snapshot. Consequently, the threshold has to be determined empirically with the help of simulations. Preferably, this is done in a conservative way, such that situations with two targets are only detected when reliable parameter estimation is possible.

A scheme for optimal parameter estimation and detection in the considered scenario, by means of a GLRT, is shown in Figure 3.5. This scheme is computationally intensive, since the ML estimate for two targets has to be computed for every snapshot.

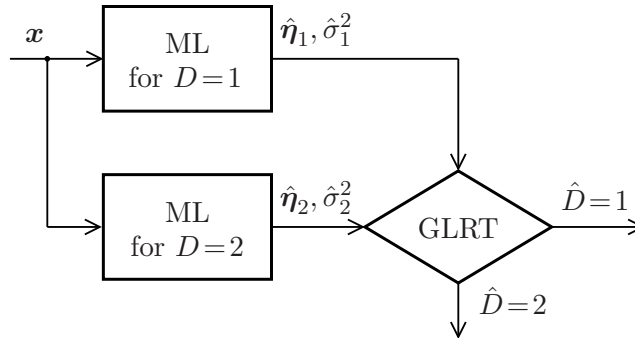


Figure 3.5. Optimal approach for DOA estimation and target detection in the identified potential two-target case with a single snapshot.

3.3.3 Experimental data example

To demonstrate the performance of the described optimal approach, we present results with real data in controlled experiments with one and two corner reflectors. We use an automotive radar system prototype for MRR applications, whose system parameters are given in Table 3.1. The experimental setup is depicted in Figure 3.6 and

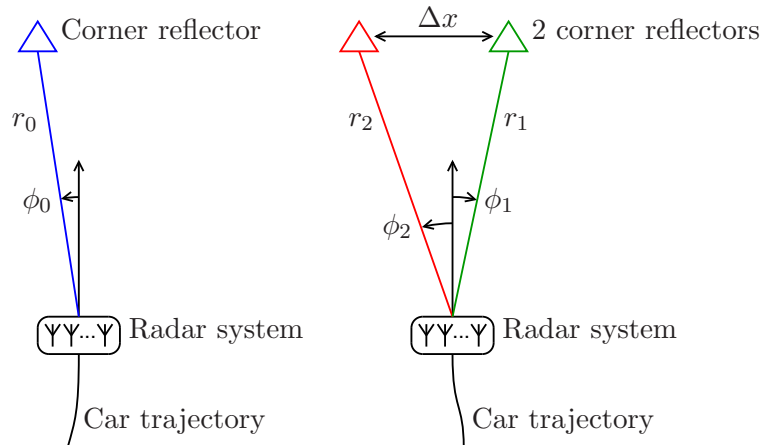


Figure 3.6. Experimental setup: radar system mounted on a vehicle, which is approaching a single corner reflector (left) and two corner reflectors (right).

described in the following. The radar system is mounted on an experimental vehicle, which is approaching corner reflectors of similar size. In a reference experiment, the car is approaching a single corner reflector. Then, the car is approaching two corner reflectors, which are at the same range r and appear in the same processing cell. In two experiments, the corner reflectors are spaced by $\Delta x = 4$ m and 1.7 m, respectively. In a centered and symmetric configuration, the angles would be

$$\phi_1 = \sin^{-1}\left(\frac{+\Delta x}{2r}\right)$$

$$\phi_2 = \sin^{-1}\left(\frac{-\Delta x}{2r}\right)$$

This simple approximation gives a general idea: the observed spatial angles vary with cycle index n , the angular separation $\phi_2 - \phi_1$ increases for decreasing range r . However, this model does not take into account a non-centered geometric configuration or a non-ideal trajectory of the car. Hence, there is no ground truth for the DOA estimates, and we can only analyze statistical variations.

The relevant processing cells are extracted and the described optimal approach is applied. For DOA estimation of one and two targets, we use a ML grid search, uniformly spaced in electrical angle by $\pi/128$, followed by a quadratic interpolation, as described in Appendices 3.A.2 and 3.A.1. To decide between one and two targets, we use a GLRT with a relatively conservative threshold, $\log \gamma_{\text{GLRT}} = 1.5M$.

First, we present the results when approaching a single corner reflector. For ranges between 45 m and 7.2 m, we obtain 221 correct and 43 presumably incorrect decisions

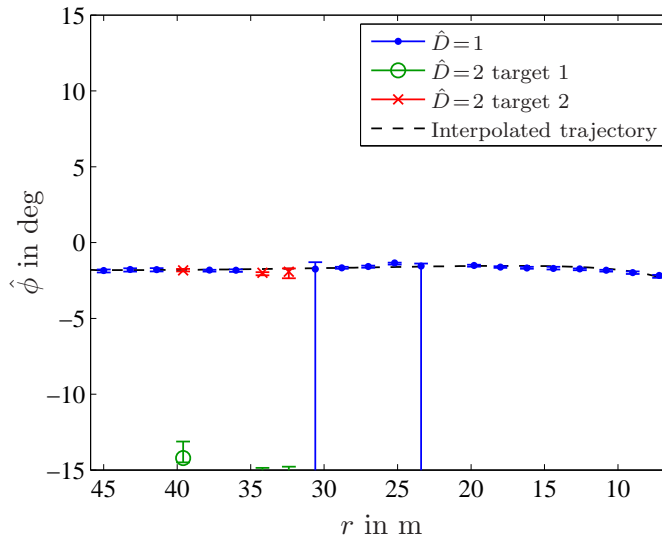


Figure 3.7. Experimental data analysis for $D = 1$ target. Error bars of DOA estimates of each range bin with at least 6 coincident detection, and interpolated trajectory.

for one and two targets, respectively. The error bars of DOA estimates of each range bin with at least 6 coincident detections is shown in Figure 3.7. For the detected situation with one target, we use blue error bars with a point marker, whereas for the detected situations with two targets, we use green and red error bars, with a circle and cross marker, respectively. Each error bar element displays the 0.1-, 0.5-, and 0.9-quantile of the respective measurement set. Also, we overlay an interpolated trajectory, which has been determined by fitting a cubic polynomial to the estimated x/y -coordinates. It can be observed from Figure 3.7 that the obtained estimates are reasonably accurate. At ranges around 24 m and 33 m, the signal energy is reduced, possibly due to multipath interference with the ground, as described e.g. in [BY07]. At these ranges, a weak secondary target causes estimation outliers, and several erroneous decisions for the two-target case.

Second, we present the results when approaching two corner reflectors spaced by Δx . For $\Delta x = 4$ m, and for the same ranges as above, we obtain 28 presumably incorrect and 191 correct decisions for one and two targets, respectively. Analogously, for $\Delta x = 1.7$ m, we obtain 91 presumably incorrect and 194 correct decisions. The corresponding error bar results are shown in Figure 3.8. Also indicated are the range cuts at which the angular separation $\phi_2 - \phi_1$ corresponds to BW_ϕ and 1.5BW_ϕ , such that the two targets are theoretically and reliably resolved in the BF spectrum and high-resolution DOA estimation is not strictly necessary. It can be observed from Figure 3.8 that the obtained results are reasonably accurate. Again, at ranges around 24 m and 33 m, the estimation and detection performance is poor due to a reduced signal energy. We note

that the chosen representation with error bars is meaningful to analyze the estimation accuracy when the true DOA is almost constant within a range bin. This holds for distant ranges, where the variation of the true DOA trajectory is slow. However, for closer ranges, this variation becomes quicker, resulting in wider error bars although the results are still accurate. This effect is only due to the chosen representation.

3.4 Discussion

In this chapter, we have considered the problem of high-resolution DOA estimation and detection for a typical automotive radar system. We have described a pulsed radar system with an array of receive antennas. A possible radar pre-processing consists of two DFTs with respect to the fast sample time and the pulses, respectively. This results in processing cells according to range and relative velocity, each represented by a single snapshot. In most cases, multiple targets can be distinguished by their range and/or relative velocity, so that each processing cell only contains a single target. However, there are situations, in which several targets are superposed in a processing cell. We have identified the situation with two targets as practically relevant, and have described several use cases. An optimal approach for DOA estimation and detection has been presented, which is based on ML estimation and a GLRT. The limitations in terms of accuracy and resolution have been analyzed specifically for the single-snapshot case.

Results with real data from experiments with a single and two corner reflectors have been presented to demonstrate the practical value of high-resolution DOA estimation for automotive radar. The described optimal approach provides reasonably good results with an enhanced resolution. However, this is achieved at a high computational cost, since for every detected processing cell a two-dimensional ML grid search is performed. In the next chapter, we aim at reducing the computational cost.

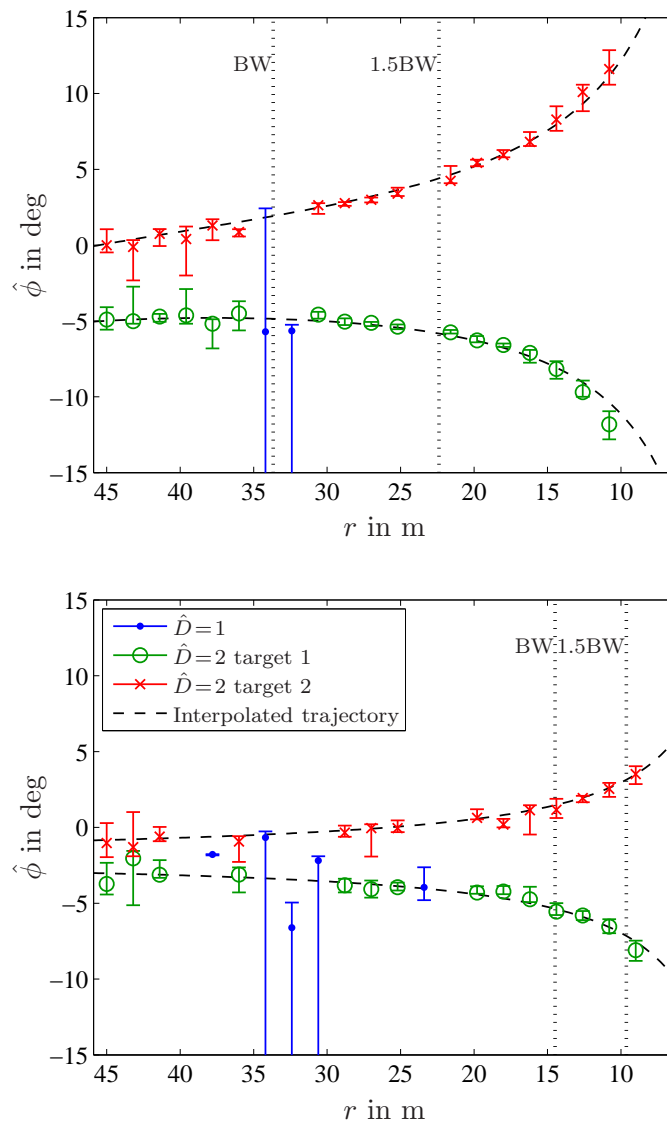


Figure 3.8. Experimental data analysis for $D = 2$ targets, spaced by $\Delta x = 4$ m (top) and 1.7 m (bottom). Error bars of DOA estimates of each range bin with at least 6 coincident detections, and interpolated trajectory.

3.A Appendix

3.A.1 Interpolation of maximum likelihood objective function

Let $c(\psi_1, \psi_2)$ be the ML objective function, as defined in (3.16), which has been evaluated on a uniform discrete grid with step size $\Delta\psi$. Let the global maximum occur at index (m, n) with corresponding locations $\psi_{1,m}$ and $\psi_{2,n}$. Refined estimates of the peak locations can be obtained via a quadratic interpolation strategy [TF09, Ch. 1]. Towards this end, let a two-dimensional elliptic paraboloid function be given by

$$\tilde{c}(\psi_1, \psi_2) = \alpha_1(\psi_1 - \hat{\psi}_1)^2 + \alpha_2(\psi_2 - \hat{\psi}_2)^2 + \hat{c}$$

where α_1 and α_2 are the paraboloid width parameters, $\hat{\psi}_1$ and $\hat{\psi}_2$ are the desired refined peak locations, and \hat{c} is a refined peak value. We can set up a system of equations by evaluating the paraboloid function at peak index (m, n) and its direct neighbors $(m \pm 1, n)$ and $(m, n \pm 1)$, where the corresponding values of the objective function are denoted by $c_{m,n}$, $c_{m\pm 1,n}$ and $c_{m,n\pm 1}$. Solving for unknown parameters, we obtain

$$\begin{aligned}\hat{\psi}_1 &= \psi_{1,m} + 0.5\Delta\psi \frac{c_{m-1,n} - c_{m+1,n}}{c_{m-1,n} - 2c_{m,n} + c_{m+1,n}} \\ \hat{\psi}_2 &= \psi_{2,n} + 0.5\Delta\psi \frac{c_{m,n-1} - c_{m,n+1}}{c_{m,n-1} - 2c_{m,n} + c_{m,n+1}}\end{aligned}$$

Note that estimates for $\hat{\psi}_1$ and $\hat{\psi}_2$ are decoupled, and correspond to one-dimensional quadratic interpolations in each dimension. We remark that when the targets are well separated, the two-dimensional elliptic paraboloid well approximates the ML objective function around its global maximum, and this strategy is able to improve the estimation accuracy.

3.A.2 Interpolation of beamformer spectrum

Likewise, a quadratic interpolation strategy can be used to obtain refined DOA estimates from the BF spectrum $P_{\text{BF}}(\psi)$, as defined in (3.18), which has been evaluated on a uniform discrete grid with step size $\Delta\psi$. Let the maximum occur at index n with corresponding location ψ_n . Around its maximum, the BF spectrum is well approximated by quadratic function

$$\tilde{P}(\psi) = \alpha_0(\psi - \hat{\psi})^2 + \hat{P}$$

where α_0 is the parabola width parameter, $\hat{\psi}$ is the desired refined peak location, and \hat{P} is a refined peak value. By evaluating the quadratic function at peak index n and

its direct neighbors, where the corresponding values of the BF spectrum are denoted by P_n , P_{n-1} and P_{n+1} , we can set up a system of equations, which can be solved for

$$\hat{\psi} = \psi_n + 0.5\Delta\psi \frac{P_{n-1} - P_{n+1}}{P_{n-1} - 2P_n + P_{n+1}}.$$

Chapter 4

Array processing for automotive radar with reduced complexity

In the previous chapter, we have presented an optimal approach for array processing in the considered potential two-target case with a single snapshot. This approach provides reasonably good results with real data in controlled experiments with one and two corner reflectors. However, in the considered GLRT framework, computationally intensive ML estimation of two targets is performed for all detected processing cells, which may become intractable in real-time. This is particularly unfortunate since in many practical cases, each detected processing cell only contains a single target.

In this chapter, we present a practicable approach for array processing for automotive radar, which is expected to perform similarly as the optimal approach, but with reduced computational complexity. The general idea is to pre-select the processing cells, in which only a single target is present or two targets are well separated. Thus, the computationally intensive ML estimation of two targets is carried out only if its high-resolution performance is required. In Section 4.1, we analyze the performance of the BF for DOA estimation of two targets with a single snapshot, in terms of resolution and accuracy, and propose a simple resolution criterion. In Section 4.2, we present the array processing chain of the proposed practicable approach, which takes into account the identified shortcomings of the BF. When two targets are resolved in the BF spectrum, the resulting DOA estimates are generally biased due to leakage. For this case, we propose a strategy for bias correction with low computational complexity in Section 4.3. When the BF spectrum shows only a single significant peak, either a single target is present or two targets are unresolved. For this case, in Section 4.4, we present a test with low computational complexity to decide whether the model with a single target is appropriate. The performance of the developed approaches is analyzed in simulations and with real data.

4.1 Preliminaries

For convenience, we briefly restate the array processing problem in the considered potential two-target case from Section 3.2.3: given snapshot \mathbf{x} from a detected processing

cell, decide between

$$\begin{aligned} D = 1 : \mathbf{x} &= s_0 \mathbf{a}(\psi_0) + \mathbf{e} \\ D = 2 : \mathbf{x} &= s_1 \mathbf{a}(\psi_1) + s_2 \mathbf{a}(\psi_2) + \mathbf{e} \end{aligned}$$

where

$$\mathbf{a}(\psi) = e^{-j(M-1)\psi/2} [1, e^{j\psi}, \dots, e^{j(M-1)\psi}]^T, \quad \psi = \kappa d \sin(\phi) \quad (4.1)$$

is the steering vector of a ULA in x -direction, centered at the origin, variable ψ represents electrical angle, and ϕ is the physical azimuth angle, as defined in Figure 2.1.

We consider the situation with similar target magnitudes $|s_1|^2 \approx |s_2|^2 \gg \sigma^2$ as practically relevant in the two-target case. Note that when the target magnitudes are differing strongly, e.g. by more than 10 dB, DOA estimation is generally more challenging. One can imagine the task of resolving a slowly driving truck from a pedestrian. However, for the described application, these situations are of minor importance.

4.1.1 Beamformer for two targets

DOA estimation with the BF is considered as a standard approach for several reasons. It constitutes the optimal nonlinear LS or ML solution for a single target, as described e.g. in Section 3.3.1.1, and can serve as a good approximation for multiple targets, depending on whether the targets are well separated and the number of snapshots is large [SM97]. Moreover, the BF spectrum can be efficiently calculated using an FFT. For the considered situation with a single snapshot and two targets, however, the performance may be limited. Formally, two targets cannot be resolved in the BF spectrum if separated by less than the Rayleigh BW, as defined in (3.22). In the following, we present numerical examples to give a general idea of the behavior of the BF spectrum in the two-target case with a single snapshot.

We consider an 8-element ULA, two targets of equal magnitude and the noise-free case. We vary angular separation δ and relative phase φ , as defined in (3.11). For several combinations, the BF spectrum from (3.18) is calculated. The result is shown in Figure 4.1 for cases (a)-(i), where solid green lines correspond to the determined local maxima, and dashed gray lines correspond to the true DOA parameters. In contrast to expectations, the BF spectrum shows two resolved peaks in (a), whereas it shows a single peak in (h). Moreover, when the targets are well separated, the DOA estimation error is negligible in (f), whereas it is large in (c) and (i). Hence, the BF spectrum behaves unfavorably when the relative phase is around 0 or π , which is similar to the observation in Figure 3.4.

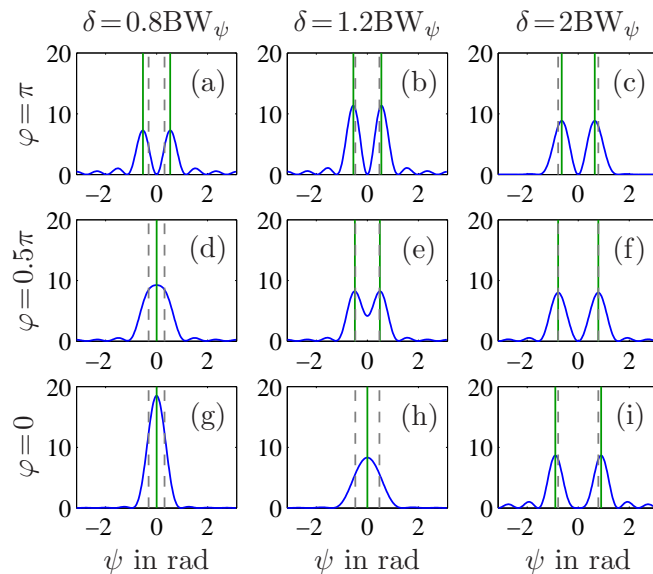


Figure 4.1. BF spectra $P_{\text{BF}}(\psi)$ of two targets in the noise-free case with an 8-element ULA for various angular separation δ and relative phase φ , solid green lines indicate the determined local maxima, dashed gray lines indicate the true DOA parameters.

To quantitatively study the actual resolution ability and DOA estimation error of the BF with a single snapshot, we vary δ and φ on a fine grid. In each situation, the BF spectrum is calculated and the two largest local maxima $\psi_{\text{BF},1} < \psi_{\text{BF},2}$ are determined. The targets are considered as resolved if the determined peaks are close to the true DOA parameters, i.e.

$$|\psi_{\text{BF},1} - \psi_1| < \frac{\delta}{2} \quad \cap \quad |\psi_{\text{BF},2} - \psi_2| < \frac{\delta}{2}.$$

In this case, the DOA estimation error of the first target $\psi_{\text{BF},1} - \psi_1$ is determined. The result is displayed in Figure 4.2, where the white area corresponds to the unresolved cases. One can observe that the BF is able to resolve the targets even below the Rayleigh BW for relative phases close to π , whereas for relative phases close to 0, the targets are resolved only for larger angular separations. Also, one can observe for the resolved cases, that DOA estimation is biased, where the bias depends on the angular separation and the relative phase. Note that the bias can be very large when the BF is just able to resolve the targets.

In conclusion, the resolution ability and DOA estimation error of the BF critically depend on the angular separation and the relative phase. Since the results have been obtained in the noise-free case, Figure 4.2 represents a fundamental limitation for DOA estimation of two targets with the BF. We note that the DOA estimation bias shows a regular structure, similar to the sidelobes in the beampattern. This is analyzed in more detail in Section 4.3.

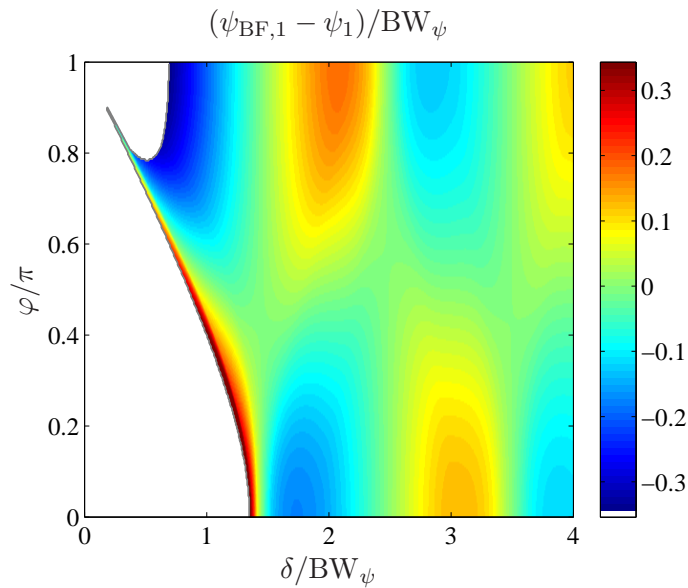


Figure 4.2. DOA estimation of two targets in the noise-free case with an 8-element ULA. Normalized estimation error of the first target versus angular separation δ and relative phase φ , the white area corresponds to unresolved cases.

4.1.2 Beamformer resolution criterion

In the numerical example from Figure 4.2, a simple criterion is used to determine if the two targets are resolved, based on the knowledge of the true DOA parameters. However, in practice these are not available and another resolution criterion is required, solely based only on the characteristics of the estimated BF spectrum. This resolution criterion should take into account the BF resolution ability, as discussed above, and the SLL in the beampattern of the employed window function. Note that it is undesirable to declare a sidelobe, possibly increased by noise effects, as a weak second target. Hence, the second target should only be detected when its power is significantly above the sidelobes of the primary target.

Exemplarily, Figure 4.3 shows a BF spectrum with possibly two targets. Let $\hat{\psi}_1 < \hat{\psi}_2$ be the locations of the two largest local maxima, with magnitudes \hat{p}_1 and \hat{p}_2 , respectively. When the power ratio between the targets, ρ , as defined in (3.11), is smaller than SLL or larger than $1/\text{SLL}$, the weaker target will be masked by the sidelobes of the stronger target. Therefore, it is advisable to detect a second target only if

$$\frac{\hat{p}_2}{\hat{p}_1} \in \left[\rho_{\min}, \frac{1}{\rho_{\min}} \right] \quad (4.2)$$

where $\rho_{\min} < \text{SLL}$ is the smallest allowed power ratio, taking into account the effect of sidelobes and noise. For instance, when employing a Chebyshev window with a sidelobe

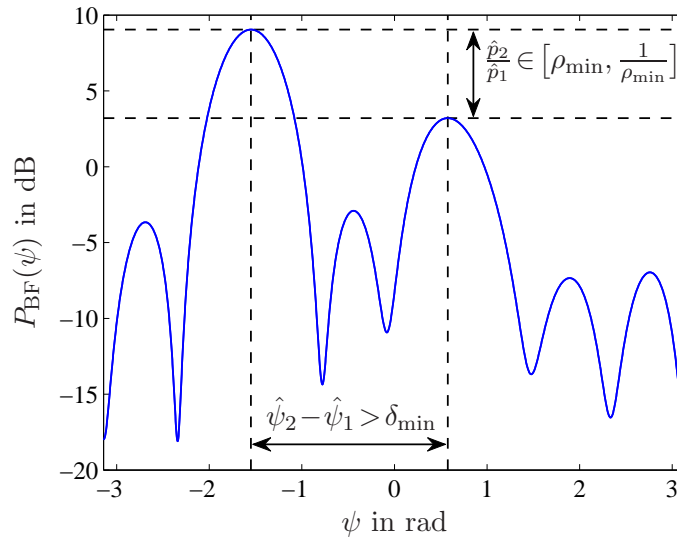


Figure 4.3. BF spectrum of possibly two targets. Conditions of the proposed resolution criterion are indicated, δ_{\min} is the smallest allowed angular separation, ρ_{\min} is the smallest allowed power ratio.

attenuation of 20 dB, this can be $\rho_{\min} = 0.1$. Moreover, we know from Figure 4.2, that the DOA estimation error can be very large when the BF is just able to resolve the targets. Therefore, it appears reasonable to consider two targets as resolved and reliably localized if

$$\hat{\psi}_2 - \hat{\psi}_1 > \delta_{\min} \quad (4.3)$$

where δ_{\min} is the smallest allowed angular separation. From Figure 4.2, a conservative choice would be $\delta_{\min} = 1.5BW_{\psi}$. In conclusion, a suitable resolution criterion based on the BF spectrum can be obtained by combining (4.2) and (4.3).

4.2 Proposed array processing

An optimal approach for array processing in the considered potential two-target case with a single snapshot has been presented in Section 3.3. This involves computationally intensive ML estimation of two targets for all detected processing cells, although it is not required for processing cells, in which only a single target is present or two targets are well separated. A pre-selection of these cases allows to save computations, so that the more complicated ML estimation of two targets is carried out only if its high-resolution performance is required. The proposed array processing chain, similar to Figure 3.5 but with reduced computational cost, is shown in Figure 4.4.

After calculating the BF spectrum, the BF resolution criterion is applied, as described in Section 4.1.2. When two targets are resolved, their DOA estimates are biased and can be enhanced by a bias correction. A strategy for bias correction with low computational complexity is proposed in Section 4.3. When the BF spectrum shows only a single significant peak, a test is used to decide whether the model with a single target is appropriate, or one should consider a model with multiple targets. A computationally simple approach for this multiple target detection is presented in Section 4.4. Only when the BF cannot resolve two targets and the single-target model is rejected, the computationally intensive ML estimation of two targets is carried out. A practicable implementation for this task is proposed in Chapter 5. Finally, a GLRT is used as a consistency check of the two-target model.

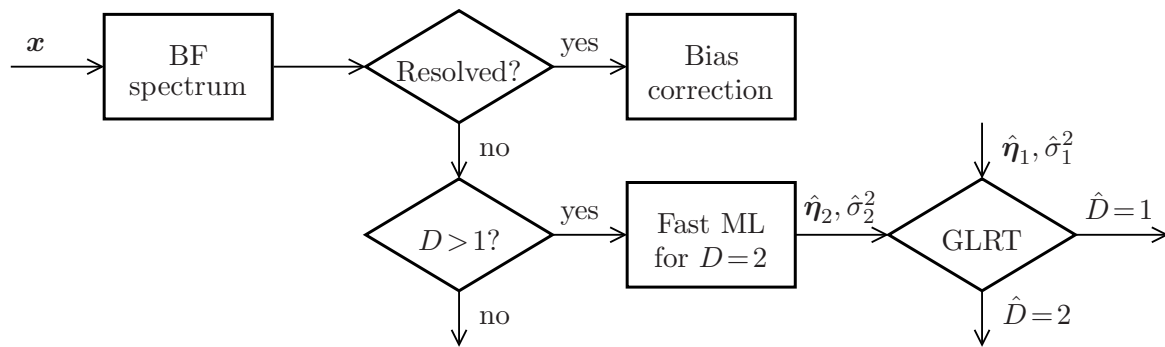


Figure 4.4. Proposed array processing chain for DOA estimation and target detection in the potential two-target case with reduced computational cost.

4.3 Bias correction for DOA estimation of two resolved targets

We have seen in Section 4.1.1, that when two targets are well separated, so that they are resolved in the BF spectrum, the corresponding DOA estimates are generally biased due to leakage. In the case with a single snapshot, this bias critically depends on the angular separation and the relative phase. We propose a novel strategy for bias correction with low computational complexity, which is based on the analysis of the noise-free BF spectrum and local approximations. This approach has been reported in [HZ12]. Moreover, we consider the RELAX algorithm, which represents a popular iterative ML implementation, and is also based on the BF spectrum.

The problem formulation is stated as follows. Consider a resolved two-target situation,

i.e. with $\delta > \text{BW}_\psi$, and the windowed BF spectrum, given by

$$P_{\text{BF}}(\psi) = \frac{1}{M} \underbrace{|\mathbf{a}(\psi)^H \text{diag}\{\mathbf{w}\} \mathbf{x}|^2}_{S(\psi)} \quad (4.4)$$

where $S(\psi)$ denotes the windowed spatial Fourier transform, and \mathbf{w} contains the coefficients of a window function, normalized such that $\|\mathbf{w}\|^2 = M$. Provided the SNR is sufficiently high, the two largest local maxima of the BF spectrum, denoted $\hat{\psi}_{\text{BF},1} < \hat{\psi}_{\text{BF},2}$, are close to the true DOA parameters, but biased due to leakage. We aim at correcting this bias.

4.3.1 Proposed approach

Before introducing the proposed algorithm for bias correction, we analyze the noise-free BF spectrum and the resulting bias of DOA estimation.

4.3.1.1 Noise-free beamformer spectrum

In the noise-free case, the spatial Fourier transform is

$$S(\psi) = s_1 W(\psi - \psi_1) + s_2 W(\psi - \psi_2) \quad (4.5)$$

where

$$W(\psi - \psi_i) = \mathbf{a}(\psi)^H \text{diag}\{\mathbf{w}\} \mathbf{a}(\psi_i) = \mathbf{a}(\psi - \psi_i)^H \mathbf{w}, \quad i = 1, 2$$

is a shifted beampattern. We assume the centered steering vector from (4.1) and \mathbf{w} to be symmetric. In this case, the beampattern is easily shown to be real-valued [vT02]. Note that the same analysis has been reported in [HZ12] for a non-centered steering vector. Using (4.4) and (4.5), the noise-free BF spectrum can be expressed as

$$P_{\text{BF}}(\psi) = \frac{|s_1|^2}{M} W(\psi - \psi_1)^2 + \frac{|s_2|^2}{M} W(\psi - \psi_2)^2 + \frac{2|s_1||s_2|\cos(\varphi)}{M} \underbrace{W(\psi - \psi_1)W(\psi - \psi_2)}_{Q(\psi)}. \quad (4.6)$$

The first and second term are auto-terms and show peaks at exactly ψ_1 and ψ_2 , respectively. However, when superimposed, the sidelobes of the respective other squared beampattern may shift the peak location. The third term is a cross-term and also affects the peak locations. In the single-snapshot case, we have observed that the influence of the cross-term on the peak locations overshadows the effect of the sidelobes of the respective other squared beampattern. To analyze the resulting bias, let us have a

closer look at the squared beampattern $W(\psi - \psi_i)^2$, $i = 1, 2$ and the cross beampattern $Q(\psi)$.

For simplicity, we first consider the rectangular window, i.e. $\mathbf{w} = \mathbf{1}_M$. Plugging in the definition of the auto-terms in (4.6), and after some simplifications, we obtain

$$W(\psi - \psi_i)^2 = \frac{\sin[(\psi - \psi_i)M/2]^2}{\sin[(\psi - \psi_i)/2]^2}$$

which is the well-known squared periodic sinc function, centered around ψ_i . The shape of this function only depends on M . It can be approximated locally around ψ_i as a quadratic function, $w_0 + \alpha_w(\psi - \psi_i)^2$, where w_0 is the maximum of the squared beampattern and α_w is a parabola width parameter. In order to determine α_w , the Taylor series expansion of $\sin(x)$ can be used to obtain

$$\frac{1}{x^2} \sin(x)^2 = \frac{1}{x^2} \sum_{m=0}^{\infty} \sum_{n=0}^{\infty} \frac{(-1)^m x^{2m+1}}{(2m+1)!} \frac{(-1)^n x^{2n+1}}{(2n+1)!} = 1 - \frac{1}{3}x^2 + \dots$$

Furthermore, when approximating the periodic sinc function by the standard sinc function, the above identity can be used to obtain

$$\frac{\sin[(\psi - \psi_i)M/2]^2}{\sin[(\psi - \psi_i)/2]^2} \approx M^2 \frac{\sin[(\psi - \psi_i)M/2]^2}{[(\psi - \psi_i)M/2]^2} \approx M^2 \left[1 - \frac{M^2}{12} (\psi - \psi_i)^2 \right]$$

and therewith $\alpha_w = -M^4/12$.

Likewise, plugging in the definition of the cross beampattern in (4.6), and after some simplifications, we obtain

$$Q(\psi) = \frac{\cos(\delta M/2) - \cos[(\psi - \psi_M)M]}{\cos(\delta/2) - \cos(\psi - \psi_M)}$$

centered around ψ_M , which denotes the midpoint between ψ_1 and ψ_2 . The shape of this function depends on M and δ . It can be approximated locally around ψ_i as a linear function, $q_{0,i} + \beta_i(\psi - \psi_i)$, where $q_{0,i}$ is value of the cross beampattern at ψ_i and

$$\beta_i = \lim_{\psi \rightarrow \psi_i} \frac{\partial Q(\psi)}{\partial \psi}$$

is the respective slope. The limit does not exist. However, after applying l'Hôpital's rule twice, we obtain

$$\beta_1 = \frac{M \cos(\delta/2) \sin(\delta M/2) - M^2 \sin(\delta/2) \cos(\delta M/2)}{2 \sin(\delta/2)^2}$$

$$\beta_2 = -\beta_1.$$

For window functions, other than the rectangular window, the local approximations are still valid, but expressions for α_w and β_1 are more complicated and require numerical computation. α_w can be determined by means of LS fitting, β_1 can be determined by employing the central first-order finite difference, for small Δ

$$\beta_1 \approx \frac{1}{2\Delta}[Q(\psi_1 + \Delta) - Q(\psi_1 - \Delta)].$$

For computational reasons, the values for β_1 can be stored in a one-dimensional lookup table as a function of δ .

The suggested local approximations can be used to derive a simple approximation of the noise-free BF spectrum from (4.6). Neglecting the sidelobes of the respective other squared beampattern, $P_{\text{BF}}(\psi)$ is approximated locally around ψ_i as

$$\tilde{P}_i(\psi) = \frac{|s_i|^2}{M}[w_0 + \alpha_w(\psi - \psi_i)^2] + \frac{2|s_1||s_2|\cos(\varphi)}{M}[q_{0,i} + \beta_i(\psi - \psi_i)]. \quad (4.7)$$

The locations of the peaks of this function around ψ_i , $i = 1, 2$ approximate those of the noise-free BF spectrum, denoted $\psi_{\text{BF},1}$ and $\psi_{\text{BF},2}$, and can be determined by equating the first derivative to zero

$$\frac{\partial \tilde{P}_i(\psi)}{\partial \psi} = \frac{|s_i|^2}{M}2\alpha_w(\psi - \psi_i) + \frac{2|s_1||s_2|\cos(\varphi)}{M}\beta_i = 0$$

which yields

$$\psi_{\text{BF},1} \approx \psi_1 - \frac{1}{\alpha_w} \frac{|s_2|}{|s_1|} \cos(\varphi) \beta_1(\delta) \quad (4.8)$$

$$\psi_{\text{BF},2} \approx \psi_2 - \frac{1}{\alpha_w} \frac{|s_1|}{|s_2|} \cos(\varphi) \beta_2(\delta). \quad (4.9)$$

Consequently, the location of the peaks of the noise-free BF spectrum is approximately equal to the true parameter plus a bias term, which depends on signal parameters $|s_1|$, $|s_2|$, φ and δ . Note that the bias term depends on a ratio between signal magnitudes, where the bias will be larger for the weaker target.

An example is used to demonstrate the local approximations of the noise-free BF spectrum. We consider an 8-element ULA with a rectangular window, and two targets with angular separation $\delta = 2\text{BW}_\psi$, relative phase $\varphi = 7\pi/8$ and power ratio $\rho = 0.5$, as defined in (3.11). Figure 4.5 (left) shows the corresponding noise-free BF spectrum. Around the DOA of the first target, we calculate the auto- and cross-term in (4.6), the local approximation of the BF spectrum in (4.7), and corresponding approximations of the auto- and cross-term. The result is shown in Figure 4.5 (right). One can observe that the local approximations represent a good match in this case, although we have neglected the sidelobes from the respective other auto-term.

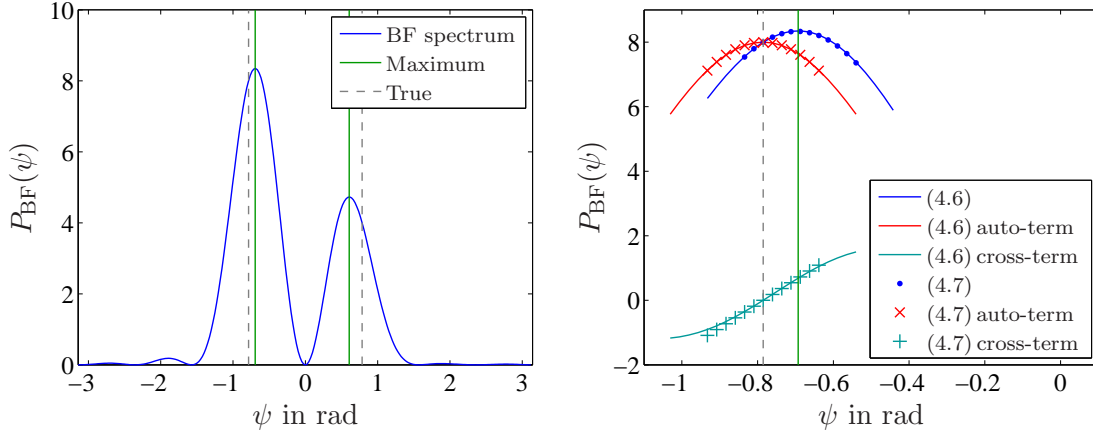


Figure 4.5. Local approximations for the noise-free BF spectrum of two targets with angular separation $\delta = 2BW_\psi$, relative phase $\varphi = 7\pi/8$ and power ratio $\rho = 0.5$. BF spectrum with DOA estimation errors (left). Suggested local approximations for the first target (right).

4.3.1.2 Algorithm for bias correction

We propose to obtain enhanced DOA estimates from the BF by subtracting the bias terms in (4.8) and (4.9). The proposed algorithm for bias reduction can be summarized as follows:

1. Evaluate the BF spectrum in (4.4) and determine the two largest local maxima, $\hat{\psi}_{BF,1} < \hat{\psi}_{BF,2}$, and corresponding target response parameter estimates

$$\hat{\mathbf{s}}_i = \frac{1}{M} \mathbf{a}(\hat{\psi}_{BF,i})^H \mathbf{x}$$

2. Calculate $\hat{\delta}$ and $\hat{\varphi}$ from $\hat{\psi}_{BF,1}$, $\hat{\psi}_{BF,2}$, $\hat{\mathbf{s}}_1$ and $\hat{\mathbf{s}}_2$.
3. Determine $\beta_1(\hat{\delta})$ from a lookup table.
4. Estimate the corrected DOA parameters as

$$\hat{\psi}_1 = \hat{\psi}_{BF,1} + \frac{1}{\alpha_w} \frac{|\hat{\mathbf{s}}_2|}{|\hat{\mathbf{s}}_1|} \cos(\hat{\varphi}) \beta_1(\hat{\delta})$$

$$\hat{\psi}_2 = \hat{\psi}_{BF,2} - \frac{1}{\alpha_w} \frac{|\hat{\mathbf{s}}_1|}{|\hat{\mathbf{s}}_2|} \cos(\hat{\varphi}) \beta_1(\hat{\delta}).$$

The main part of the computational cost constitutes the evaluation of the BF spectrum in step 1, which can be efficiently computed using an FFT with zeropadding. The DOA

estimates can be obtained using a quadratic interpolation in the neighborhood of the determined local maxima, as described in Appendix 3.A.2. The calculations required in steps 2-4, which involve simple scalar multiply-add operations and finding an entry from a lookup table, can be implemented efficiently and do not significantly contribute to the overall cost.

4.3.2 RELAX for two targets

The RELAX algorithm is an iterative approach for DOA estimation of multiple targets [LS96, LZS97]. It aims at finding the nonlinear LS or ML solution. In the case with two targets, parameters ψ_1 , ψ_2 , s_1 and s_2 are determined by minimizing

$$\|\mathbf{x} - s_1 \mathbf{a}(\psi_1) - s_2 \mathbf{a}(\psi_2)\|^2 \quad (4.10)$$

The principle of the RELAX algorithm is to iteratively subtract the present targets to perform approximately single-target DOA estimation with the BF, which corresponds to the ML estimate and does not suffer from leakage. Towards this end, let

$$\hat{\mathbf{x}}_1 = \mathbf{x} - \hat{s}_2 \mathbf{a}(\hat{\psi}_2) \quad (4.11)$$

$$\hat{\mathbf{x}}_2 = \mathbf{x} - \hat{s}_1 \mathbf{a}(\hat{\psi}_1) \quad (4.12)$$

where the respective estimates are assumed to be given. In this case, the minimization of (4.10) with respect to ψ_i and s_i can be simplified to

$$\hat{\psi}_i = \arg \max_{\psi} \frac{1}{M} |\mathbf{a}(\psi)^H \hat{\mathbf{x}}_i|^2, \quad \hat{s}_i = \frac{1}{M} \mathbf{a}(\hat{\psi}_i)^H \hat{\mathbf{x}}_i, \quad i = 1, 2. \quad (4.13)$$

Note that (4.13) only requires the evaluation a BF spectrum, which can be efficiently calculated using an FFT with zeropadding. In the two-target case, the RELAX algorithm can be summarized as follows [LS96]:

1. Assume a single target present, and estimate $\hat{\psi}_1$ and \hat{s}_1 from \mathbf{x} , as in (4.13), but where $\hat{\mathbf{x}}_i$ is replaced by \mathbf{x} .
2. Assume two targets present. Compute $\hat{\mathbf{x}}_2$ in (4.12) using previous estimates, and determine $\hat{\psi}_2$ and \hat{s}_2 from $\hat{\mathbf{x}}_2$, as in (4.13).
Next, compute $\hat{\mathbf{x}}_1$ in (4.11) using previous estimates, and redetermine $\hat{\psi}_1$ and \hat{s}_1 from $\hat{\mathbf{x}}_1$.
3. Convergence check; if the relative change of the cost function in (4.10) between two iterations is smaller than a predefined threshold, stop. Otherwise, continue with step 2.

Regarding computational complexity, roughly $2J + 1$ standard DOA estimation with the BF is required, where J is the number of iterations until convergence. Note that RELAX does not require the targets to be resolved. However, when not resolved, many iterations are required until convergence.

We remark that the RELAX algorithm can also be implemented in the spatial Fourier domain [Eng11]. Instead of repeatedly computing $\hat{\mathbf{x}}_1$ and $\hat{\mathbf{x}}_2$, and their corresponding BF spectra in step 2, let

$$\begin{aligned}\hat{S}_1(\psi) &= S(\psi) - \hat{s}_2 W(\psi - \hat{\psi}_2) \\ \hat{S}_2(\psi) &= S(\psi) - \hat{s}_1 W(\psi - \hat{\psi}_1)\end{aligned}$$

where $S(\psi)$ is calculated only once in step 1. Function $W(\psi) = \mathbf{a}(\psi)^H \mathbf{1}_M$ corresponds to the beampattern and can be stored in a lookup table. The calculation of one grid point of $\hat{S}_i(\psi)$ then only requires one multiply-add operation, where $W(\psi)$ is scaled by a complex scalar and shifted cyclically.

4.3.3 Simulation results

Simulations are used to assess the performance of the proposed methods for bias correction with low complexity. We consider an 8-element ULA, a Chebyshev window with a sidelobe attenuation of 20 dB, and two resolved targets with power ratio $\rho = 0.5$, and relative phase φ , which is uniformly distributed between 0 and 2π . In two simulations, we vary angular separation δ and the SNR. For the calculation of the BF spectra, we use an FFT with $4M$ grid points. The DOA estimates are obtained using a quadratic interpolation, as described in Appendix 3.A.2. For a fair assessment of grid search DOA estimation, in each simulation run, we add a random jitter, uniformly distributed between $\pm\Delta\psi/2$, to the DOA parameters.

We compare the performance of the proposed algorithm for bias correction with the CRB from (3.19). As performance metric for DOA estimation, we consider the RMSE of the first target, defined by

$$\text{RMSE}_1^2 = \frac{1}{\text{MC}} \sum_{k=1}^{\text{MC}} (\hat{\psi}_{1,k} - \psi_1)^2$$

where $\hat{\psi}_{1,k}$ is the DOA estimate of the first target in run k , and $\text{MC} = 10^4$. Also, we consider the corresponding estimates from the BF spectrum without bias correction, and from the RELAX algorithm for a single iteration and until convergence.

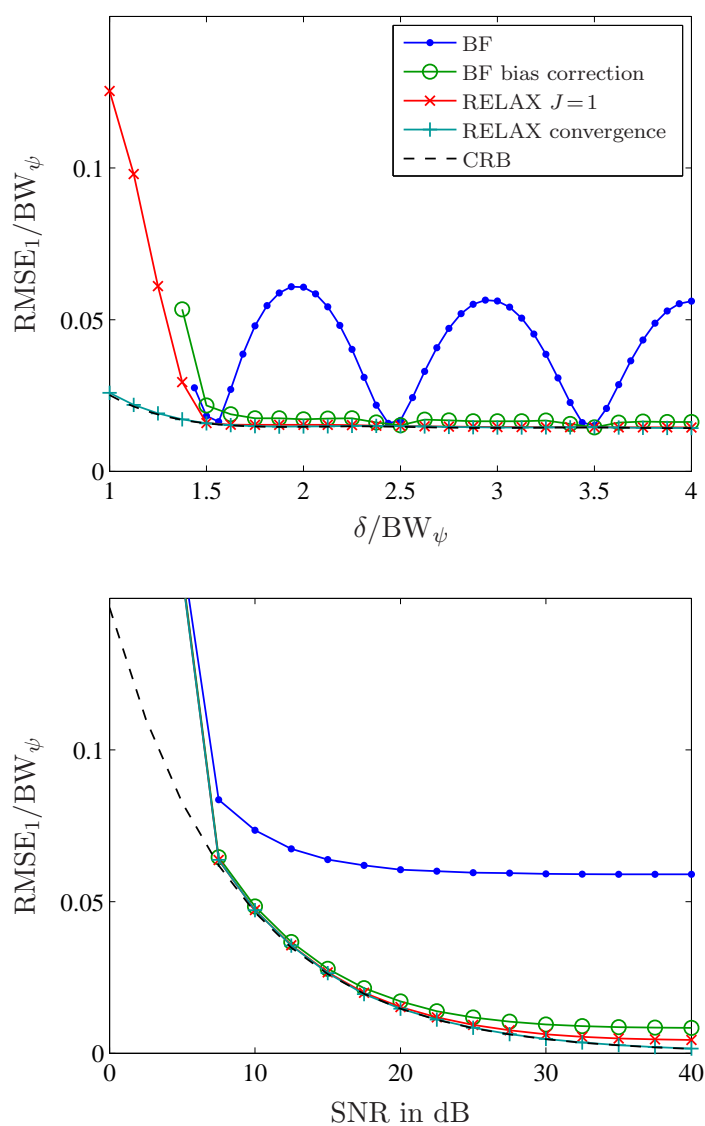


Figure 4.6. Simulation results and performance comparison for DOA estimation of two resolved targets. RMSE versus angular separation δ at SNR = 20 dB (top) and versus SNR for angular separation $\delta = 2BW_\psi$ (bottom).

First, we vary angular separation δ at $\text{SNR} = 20$ dB. The results are shown in Figure 4.6 (top). Note that we only show simulation points, for which more than 95% of trials are successfully resolved. The conventional BF can produce an average error of more than 5% of the Rayleigh BW. Using the proposed algorithm for bias correction, we are able to reduce the average error below 2% without significantly more computations. Note also that the performance of a single iteration of RELAX is very close to convergence for angular separation above 1.5BW_ψ . The corresponding computational cost is roughly three times the computational cost of a standard DOA estimation from the BF spectrum. Second, we vary the SNR for angular separation $\delta = 2\text{BW}_\psi$. The results are shown in Figure 4.6 (bottom). One can observe that the performance of the proposed approach is close to the CRB at moderate SNR. For high SNR, the proposed approach converges to a finite accuracy due to remaining errors of the local approximations.

4.3.4 Experimental data example

The experimental data example from Section 3.3.3 is revisited to demonstrate the practical applicability of the proposed bias correction. Since the true DOA parameters are unknown, we use the outcome of the ML estimate as a reference. We consider the experiment when approaching two corner reflectors spaced by $\Delta x = 4$ m. When the angular separation is greater than 1.5BW_ϕ , the BF is able to reliably resolve two targets in 67 snapshots. For these cases, we compute the differences between the DOA estimates obtained with the BF and ML, and also apply the proposed bias correction algorithm. The resulting scatter plots are shown in Figure 4.7. One can observe that the DOA estimation errors of the BF are up to 1° , whereas the bias correction is able to reduce most of the DOA estimation errors below 0.25° .

4.3.5 Conclusion

When two targets are resolved in the BF spectrum, the resulting DOA estimates are biased due to leakage. We have analyzed the noise-free BF spectrum for this case, and suggested local approximations around the true DOA parameters. A novel strategy for bias correction with low computational complexity has been proposed, which exploits the made local approximation. Moreover, we have considered the RELAX algorithm, which was found to achieve satisfactory results after a single iteration in the resolved case. The performance of the developed approach is analyzed in simulations and with real data. The results obtained from real data show that the performance of the developed algorithm is close to the ML estimate in the resolved case, but at a significantly lower computational cost.

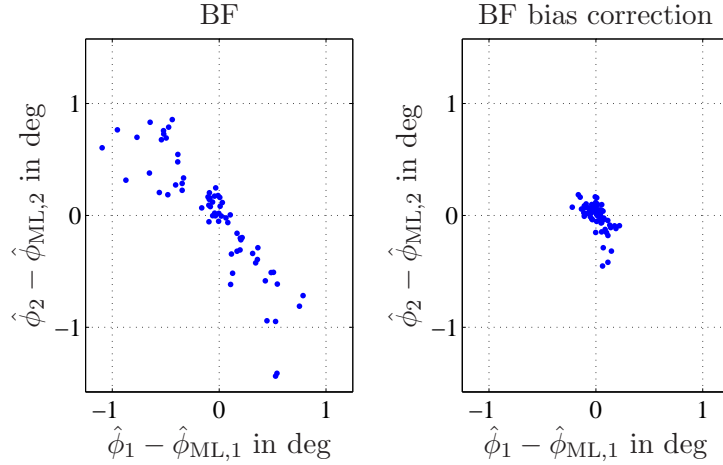


Figure 4.7. Experimental data example when approaching two corner reflectors for the resolved cases with $\phi_2 - \phi_1 > 1.5\text{BW}_\phi$, from Section 3.3.3. Scatter plot of DOA estimation errors of the BF and with bias correction, where the ML estimates are used as a reference.

4.4 Multiple target detection

When the BF spectrum shows only a single significant peak according to the presented BF resolution criterion, either a single target is present or two targets are unresolved. Instead of directly carrying out the computationally intensive ML for two targets, a test can be used to decide whether the model with a single target is appropriate. In this case, the ML for two targets is carried out only if the single-target model is rejected. This strategy can substantially save computations, when situations with more than one target are unlikely.

As an alternative to the single-target model we consider a more general situation with D targets. The proposed test aims at distinguishing

$$\begin{aligned} D = 1 : \mathbf{x} &= s_0 \mathbf{a}(\psi_0) + \mathbf{e} \\ D > 1 : \mathbf{x} &= s_1 \mathbf{a}(\psi_1) + \dots + s_D \mathbf{a}(\psi_D) + \mathbf{e} \end{aligned}$$

where \mathbf{e} is assumed to be circular complex Gaussian distributed with zero mean and covariance $\sigma^2 \mathbf{I}_M$. Towards this end, the following hypothesis for a single-target model and an unspecified alternative are considered as

$$\begin{aligned} H_0 : E\{\mathbf{x}\} &\propto \mathbf{a}(\psi) \\ H_1 : \mathbf{x} &\text{ arbitrary.} \end{aligned}$$

Initial work has been reported in [HSZ10], where H_0 has been characterized by a planar wavefront behavior, i.e. constant magnitude and linear phase among the sensor

outputs, and criteria based on the separate consideration of magnitude and phase of the array output have been proposed. To determine a suitable test statistic, we follow a more direct approach here, which is based on the ML residual. To the best of our knowledge the approach described in this section is novel and has not been presented elsewhere.

4.4.1 Proposed test statistic

When a single target is present, the measured snapshot is well represented by $s_0 \mathbf{a}(\psi_0)$ provided the SNR is sufficiently high. It appears natural to consider the fitting residual to decide whether the model with a single target is appropriate. A suitable test with low computational complexity is

$$T_D = \|\mathbf{x} - \hat{s}_0 \mathbf{a}(\hat{\psi}_0)\|^2 > \gamma_D \quad (4.14)$$

where $\hat{\psi}_0$ and \hat{s}_0 are ML estimates, which are obtained, respectively, from the global maximum of the BF spectrum and using $\hat{s}_0 = M^{-1} \mathbf{a}(\hat{\psi}_0)^H \mathbf{x}$. When test statistic T_D exceeds threshold γ_D , the single-target model is rejected. We note that a similar test can be devised where the model fitting is applied in the spatial Fourier domain, and a corresponding test statistic is found by integrating the fitting residual in the vicinity of $\hat{\psi}_0$. This approach achieves equivalent results and is not presented here.

Let the false alarm probability and detection probability

$$\begin{aligned} P_{\text{FA}} &= \Pr\{T_D > \gamma_D | \mathbf{H}_0\} \\ P_D &= \Pr\{T_D > \gamma_D | \mathbf{H}_1\} \end{aligned} \quad (4.15)$$

where $\Pr\{\cdot\}$ denotes the probability of an event, be the probabilities of incorrectly and correctly rejecting \mathbf{H}_0 , respectively. A suitable threshold can be determined by fixing the false alarm probability to a certain level. This can be done empirically with the help of simulations, or using the distribution of the test statistic under \mathbf{H}_0 . An approximated version is determined next.

4.4.1.1 Approximate distribution

The test statistic in (4.14) can be rewritten as

$$T_D = \|\mathbf{P}_{\mathbf{a}}^\perp(\hat{\psi}_0) \mathbf{x}\|^2$$

where

$$\mathbf{P}_a^\perp(\psi_0) = \mathbf{I}_M - \frac{1}{M} \mathbf{a}(\psi_0) \mathbf{a}(\psi_0)^H$$

is the projection matrix onto the orthogonal subspace spanned by $\mathbf{a}(\psi_0)$, with rank $M - 1$ [GvL96]. The distribution of (4.14) appears difficult to evaluate, since it is a function of the distribution of $\hat{\psi}_0$. However, an approximation is possible for sufficiently high SNR, by assuming that the single-target DOA estimate is reasonably accurate so that $\hat{\psi}_0 \approx \psi_0$. For $\mathbf{x} = s_0 \mathbf{a}(\psi_0) + \mathbf{e}$, we have

$$\begin{aligned} T_D &= \|\mathbf{P}_a^\perp(\hat{\psi}_0) \mathbf{x}\|^2 \\ &\approx \|\mathbf{P}_a^\perp(\psi_0) \mathbf{x}\|^2 = \|\mathbf{P}_a^\perp(\psi_0) \mathbf{e}\|^2 = \mathbf{e}^H \mathbf{P}_a^\perp(\psi_0) \mathbf{e} \end{aligned} \quad (4.16)$$

where we have used the fact that $\mathbf{P}_a^\perp(\psi_0) \mathbf{a}(\psi_0) = \mathbf{0}$, and also that projection matrices are Hermitian-symmetric and idempotent [GvL96] in the last equality. The distribution of $\mathbf{e}^H \mathbf{P}_a^\perp(\psi_0) \mathbf{e}$ is stated next.

Proposition: If \mathbf{e} is circular complex Gaussian distributed with zero mean and covariance $\sigma^2 \mathbf{I}_M$, and $\mathbf{P}_a^\perp(\psi_0)$ is a projection matrix with rank $M - 1$, $2\mathbf{e}^H \mathbf{P}_a^\perp(\psi_0) \mathbf{e} / \sigma^2$ is χ^2 distributed with $2M - 2$ degrees of freedom.

Proof: Consider eigendecomposition $\mathbf{P}_a^\perp(\psi_0) = \mathbf{U} \mathbf{I}_{M-1} \mathbf{U}^H$ where \mathbf{U} is a unitary matrix. Note that the eigenvalues of projection matrices are either one or zero [GvL96]. This allows to rewrite

$$\mathbf{e}^H \mathbf{P}_a^\perp(\psi_0) \mathbf{e} = \mathbf{y}^H \mathbf{y} = \sum_{m=1}^{M-1} |y_m|^2$$

where $\mathbf{y} = [y_1, \dots, y_{M-1}]^T = \mathbf{U}^H \mathbf{e}$ is a linear combination of \mathbf{e} . Hence, \mathbf{y} is also circular complex Gaussian distributed with zero mean and covariance $\sigma^2 \mathbf{U} \mathbf{U}^H = \sigma^2 \mathbf{I}_{M-1}$. Since $\mathbf{e}^H \mathbf{P}_a^\perp(\psi_0) \mathbf{e}$ can be expressed as the sum of $M - 1$ squared magnitudes of i.i.d. circular complex Gaussian distributed random variables, $2\mathbf{e}^H \mathbf{P}_a^\perp(\psi_0) \mathbf{e} / \sigma^2$ is χ^2 distributed with $2M - 2$ degrees of freedom [Rao73]. \square

4.4.1.2 Practical threshold setting

Using the above proposition and (4.16), $2T_D / \sigma^2$ is approximately χ^2 distributed with $2M - 2$ degrees of freedom. For a predefined value of P_{FA} , an approximate threshold can be obtained from (4.15) as

$$\gamma_D = \frac{\sigma^2}{2} F^{-1}(1 - P_{\text{FA}}, 2M - 2) \quad (4.17)$$

where $F^{-1}(\cdot, n)$ is the inverse cumulative distribution function of a χ^2 distribution with n degrees of freedom. This threshold depends on the noise variance, which is generally unknown. However, it can be estimated from neighboring processing cells without targets. For instance, in the considered radar system, the noise variance is determined in the rank order filtering for target detection [Win06].

In some practical two-target cases, one target may be significantly weaker than the other. If so, the weaker target will have a large error variance and does not strongly interfere with the primary target. In these situations, the detection of a multiple-target model and associated high-resolution DOA estimation may not lead to an enhanced target localization. To avoid unnecessary computational cost, one may want to decide for a single-target model. This can be achieved by a modified threshold, which takes into account noise effects and a weak second target. Towards this end, let $|s_1|^2 \gg |s_2|^2$ and assume that the second target does not disturb the DOA estimate of the first target. For $\mathbf{x} = s_1 \mathbf{a}(\psi_1) + s_2 \mathbf{a}(\psi_2) + \mathbf{e}$ and $\hat{\psi}_1 \approx \psi_1$, we can use the following simplistic approximation

$$\begin{aligned} T_D &= \|\mathbf{P}_a^\perp(\hat{\psi}_1) \mathbf{x}\|^2 \\ &\approx \|\mathbf{P}_a^\perp(\psi_1) \mathbf{x}\|^2 = \|\mathbf{P}_a^\perp(\psi_1)[s_2 \mathbf{a}(\psi_2) + \mathbf{e}]\|^2 \\ &\approx \underbrace{\mathbf{a}(\psi_2) \mathbf{a}(\psi_2)^H}_M |s_2|^2 + \mathbf{e}^H \mathbf{P}_a^\perp \mathbf{e} + \underbrace{2\text{Re}\{s_2 \mathbf{e}^H \mathbf{a}(\psi_2)\}}_{\mathbb{E}\{\cdot\}=0} \end{aligned}$$

where we have assumed $\mathbf{P}_a^\perp(\psi_1) \mathbf{a}(\psi_2) \approx \mathbf{a}(\psi_2)$ for convenience. The latter term has zero mean and thus can be neglected. The first and second term correspond to the influence of the weaker target and noise effects, respectively. For $|s_2|^2 < \sigma^2$, the test statistic is dominated by noise effects, and the threshold does not need to be modified. However, for $|s_2|^2 > \sigma^2$, the test statistic is dominated by the weaker second target, and the threshold should be increased. As a consequence, one can use a clipped threshold value

$$\gamma_{\text{clip}} = \max\{\gamma_D, M\mu\rho_{\min}\hat{p}_1\} \quad (4.18)$$

where μ is a scaling parameter such that ρ_{\min} is the smallest allowed power ratio, as defined in Section 4.1.2, and \hat{p}_1 is an estimate of the power of the stronger target, e.g. obtained from the instantaneous power at the first sensor $|\mathbf{x}_1|^2$. We remark that the presented approach for multiple target detection is based on the assumption of a perfectly calibrated array. In the presence of array errors, the threshold should be modified in a similar way.

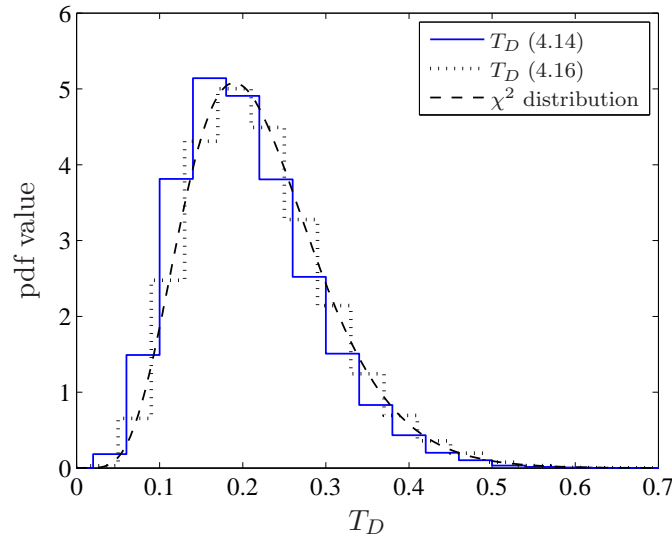


Figure 4.8. Simulation result for multiple target detection. Empirical distribution of the test statistic in the single-target case at SNR = 15 dB, approximate χ^2 distribution is overlaid.

4.4.2 Simulation results

Simulations are used to assess the performance of the proposed test for multiple target detection. We consider an 8-element ULA, a Chebyshev window with a sidelobe attenuation of 20 dB, target magnitudes $s_0 = s_1 = 1$, and define the SNR as $1/\sigma^2$.

First, in the single-target case, we demonstrate that the approximate χ^2 distribution is appropriate. 10^5 realizations of test statistic T_D , as in (4.14), and using the approximation in (4.16), are generated with an SNR of 15 dB. The histogram results are shown in Figure 4.8, where also the analytically found χ^2 distribution is overlaid. One can observe that our approximation represents a good match with empirical data.

Second, for the two-target case, we consider a signal model, parameterized by power ratio ρ and angular separation δ , as defined in (3.11). Relative phase φ is uniformly distributed between 0 and 2π . For each simulation point, 10^4 realizations are generated and test statistic T_D is calculated. The threshold is obtained from (4.17) with a preset value of $P_{FA} = 0.05$, where we assume the noise variance to be perfectly known. As performance metric, we consider the empirical detection probability P_D . Figure 4.9 shows the obtained results for P_D versus δ for fixed $\rho = 0.5$ and various SNR values. One can observe that the proposed test allows reliable detection of multiple-target situations, even for closely spaced targets, provided the SNR is sufficiently high.

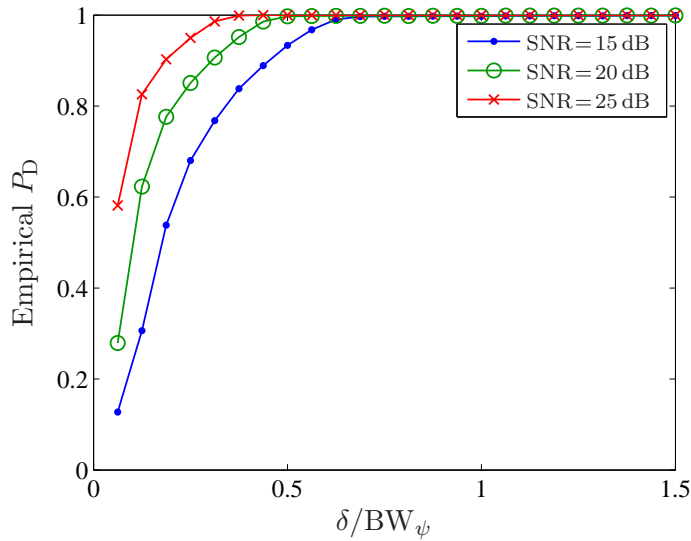


Figure 4.9. Simulation result for multiple target detection. Empirical probability of correctly detecting a multiple-target situation versus angular separation δ for various SNR values and power ratio $\rho = 0.5$.

In another simulation, the case with strongly differing target magnitudes is considered, so that the modified thresholds from (4.18) with $\mu = 0.25$ for two different values of ρ_{\min} are also applied. Figure 4.10 shows the empirical detection probability versus ρ for fixed $\delta = 0.5BW_\psi$ at an SNR of 20 dB. One can observe that when the second target is significantly weaker than the first target and the noise, all methods decide in favor of the single-target model. Multiple targets are detected when the target magnitudes are similar. When the second target is significantly larger than the first target and the noise, the method with no clipping detects two targets, whereas the methods with a clipped threshold are able to decide in favor of the single-target model, which may be desirable in practice.

4.4.3 Experimental data example

The experimental data example from Section 3.3.3 is revisited to demonstrate the practical value of the proposed test. We use the outcome of the GLRT as a reference. Hence, from the experiment when approaching a single corner reflector, we use the 221 snapshot, for which the GLRT decides in favor of the single-target model. Likewise, from the experiment when approaching two corner reflectors, spaced by $\Delta x = 4$ m, we use the 191 snapshots, for which the GLRT decides in favor of the two-target model. The proposed test statistic in (4.14) is evaluated for all snapshots. Figure 4.11 shows the histograms of the results for the considered single- and two-target situations. One

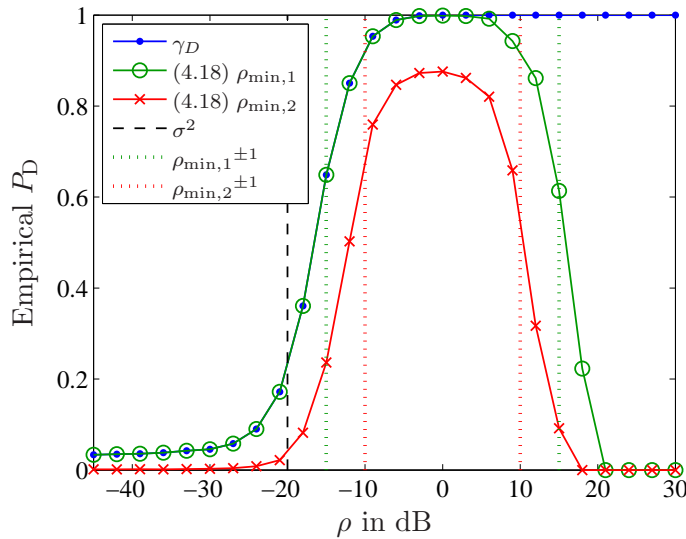


Figure 4.10. Simulation result for multiple target detection. Empirical probability of correctly detecting a multiple-target situation versus power ratio ρ , with angular separation $\delta = 0.5BW_\psi$ and SNR = 20 dB.

can observe that the two populations have distinct values and overlap only slightly. Also indicated is a possible threshold value which has been found empirically such that $P_{FA} = 0.05$. In this case, we have an empirical value of $P_D \approx 0.975$.

4.4.4 Conclusion

In some radar applications, including the described one, there are situations with multiple targets per processing cell, so that high-resolution DOA estimation is required. These approaches are considered as computationally intensive, and a general usage seems unfortunate since in many practical cases, each detected processing cell only contains a single target. To adequately handle this situation, we have proposed a test with low computational complexity to decide whether the model with a single target is appropriate. Consequently, the more complicated high-resolution DOA estimation of multiple targets is carried out only if the single-target model is rejected. We have derived an approximate distribution of the proposed test statistic, which is required to determine a suitable threshold. Also, practical aspects for threshold setting have been addressed. The performance of the developed approach has been analyzed in simulations and with real data. The developed strategy is able to substantially save computations, when situations with more than one target per processing cell are unlikely.

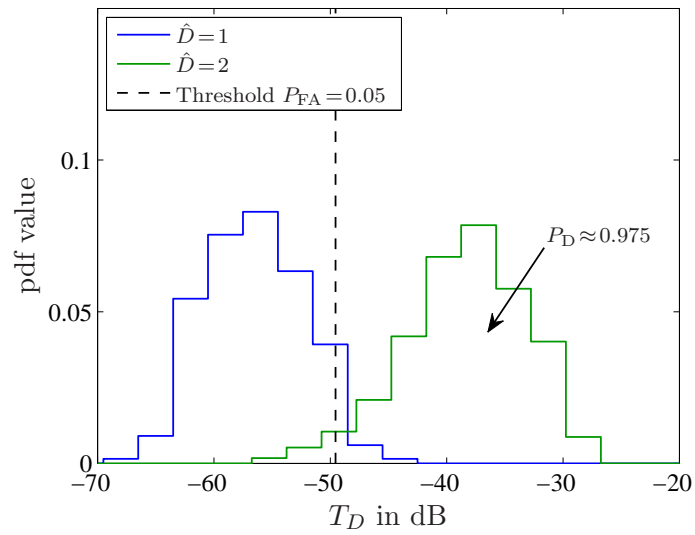


Figure 4.11. Experimental data example when approaching a single corner reflector and two corner reflectors, from Section 3.3.3. Histogram of test statistic values of processing cells, correctly detected by the GLRT, and possible empirical threshold with 5% false alarm probability.

Chapter 5

Fast maximum likelihood DOA estimation of two targets

In this chapter, we develop a practicable implementation of the deterministic ML DOA estimator of two targets. A brief background of the particular model with two targets in radar applications is given in Section 5.1. In Section 5.2, we restate the signal model and ML estimator, and describe computational aspects of the required optimization of the two-dimensional ML objective function. The proposed implementation is presented in Section 5.3, which involves a simplified calculation of the objective function and a delimited search range by using information from the BF spectrum. An example is presented to demonstrate the developed approach. In Section 5.4, the performance is analyzed in simulations, and compared with selected computationally efficient algorithms. Results with real data from a typical situation of an ACC application are presented in Section 5.5. Finally, conclusions are drawn in Section 5.6.

5.1 Background

The particular model with two targets often appears in radar applications, e.g. low angle radar tracking [Bar74,ZL91,Hay07]. Here, the goal is to localize and track an object flying at low altitude over a smooth reflecting surface such as calm sea. In this case, the radar returns from the target consist of a direct path and an indirect specular path, which gives rise to a ghost target. Typically, a vertical array is used for elevation angle estimation. At low angles, the situation becomes difficult because the direct and specular components may be closely spaced, so that they cannot be resolved in the BF spectrum, and also fall into the same range bin. The target localization is likely to be erroneous and high-resolution DOA estimation becomes necessary. A popular dataset with real-life multipath measurements was recorded on a site located at Lake Huron, Canada in 1987, using the multi-parameter adaptive radar system (MARS), consisting of a 32-element ULA of horn antennas, and developed at McMaster university. The experimental setup is such that two closely spaced components, due to the direct path and indirect path, are reflected at the sea surface. The MARS data has been analyzed in many instances, e.g. [LL91,Zol92,LZS97,Hay07]. A detailed description can be found in [Hay07, Ch. 2], where also the deterministic ML has been used as a benchmark. We

note that the described problem represents a popular application of early phased array technology and high-resolution DOA estimation.

A similar situation has been described in Chapter 3 for automotive radar. Here, the multipath is horizontal, due to a reflecting guardrail, and the array measures azimuth angles. Using the considered radar pre-processing, the received sensor data is divided into processing cells according to range and relative velocity, each represented by a single snapshot. In most practical situations, multiple targets can be distinguished by their range and/or relative velocity, so that each processing cell contains at most one target. However, there are situations, in which two targets are superposed in a processing cell. In ACC and LCA applications, this may occur when there is specular multipath with a close guardrail. If the two propagation paths are not resolved in the BF spectrum, this generally results in a false localization of the observed car, which seems to be pulled towards the guardrail. To correctly identify this situation, high-resolution DOA estimation is required. Note that the guardrail can be localized from stationary target detections. High-resolution DOA estimation of two closely spaced targets has been considered in a similar context in [WSG⁺07, Sch10, HY11a].

5.2 Preliminaries

We aim at developing a practicable implementation of the ML estimator for two targets, which can also be used in other applications. Hence, we consider a two-target model, similar as in Section 3.2.3, but with multiple snapshots

$$\mathbf{x}(i) = s_1(i)\mathbf{a}(\psi_1) + s_2(i)\mathbf{a}(\psi_2) + \mathbf{e}(i), \quad i = 1, \dots, N$$

Note that for the considered radar system multiple snapshots of the same processing cell, can be collected at different cycles. We emphasize that for the considered radar system, the single snapshot case is of primary importance. However, to enhance DOA estimation accuracy, it may be desirable to combine multiple snapshots, which have been associated in a tracking procedure. Therefore, we consider the general case with N snapshots and comment on the special case with $N = 1$. We assume closely spaced targets, which are not reliably resolved in the BF spectrum. Note that when the two targets are well separated, DOA estimation can be also done with the BF.

Since we exploit properties of the centered ULA steering vector, it is restated here

$$\mathbf{a}(\psi) = e^{-j(M-1)\psi/2} [1, e^{j\psi}, \dots, e^{j(M-1)\psi}]^T, \quad \psi = \kappa d \sin(\phi)$$

where ψ represents electrical angle, and ϕ is the physical azimuth angle, as defined in Figure 2.1.

The nonlinear LS approach has been described in Section 2.2.2, and the ML estimate of two targets has been introduced in Section 3.3.1.1. For the case with two targets and multiple snapshots, the ML objective function is restated here

$$c(\psi_1, \psi_2) = \frac{1}{N} \sum_{i=1}^N \|\mathbf{P}_{\mathbf{A}}(\psi_1, \psi_2) \mathbf{x}(i)\|^2 = \text{Tr}\{\mathbf{P}_{\mathbf{A}}(\psi_1, \psi_2) \hat{\mathbf{R}}\} \quad (5.1)$$

where

$$\mathbf{P}_{\mathbf{A}}(\psi_1, \psi_2) = \mathbf{A}(\mathbf{A}^H \mathbf{A})^{-1} \mathbf{A}^H, \quad \mathbf{A} = [\mathbf{a}(\psi_1), \mathbf{a}(\psi_2)]$$

is the projection matrix, and

$$\hat{\mathbf{R}} = \frac{1}{N} \sum_{i=1}^N \mathbf{x}(i) \mathbf{x}(i)^H$$

is the sample covariance matrix.

Subspace methods represent a popular alternative to the ML approach. A comparison of statistical properties has been outlined in Section 2.2.4, where it was found that the ML approach should be preferred when the number of snapshots is small. Despite its good properties, ML estimation has not enjoyed much practical application, as it is based on a computationally intensive optimization of a generally multi-dimensional objective function. In the two-target case, however, a brute-force evaluation $c(\psi_1, \psi_2)$ appears to be feasible on a selected grid, and is considered in the following.

Regarding implementation complexity, we note that the calculation of the ML objective function in (5.1) involves independent matrix vector products with data-independent projection operators, which can be pre-calculated off-line and stored. This is particularly suited for an efficient hardware realization, and can be easily parallelized. In contrast, subspace methods are based on an eigendecomposition, whose implementation on a practical system is numerically complex. In particular, eigendecomposition is iterative in nature, and therefore hard to parallelize [GvL96].

5.2.1 Direct objective function calculation

To calculate the projection matrix, one requires the matrix inverse of $\mathbf{A}^H \mathbf{A}$. In the two-target case, using the inversion formula for a matrix of dimension 2, and notation

$\mathbf{a}_1 = \mathbf{a}(\psi_1)$ and $\mathbf{a}_2 = \mathbf{a}(\psi_2)$ for convenience, we have

$$(\mathbf{A}^H \mathbf{A})^{-1} = \begin{bmatrix} \mathbf{a}_1^H \mathbf{a}_1 & \mathbf{a}_1^H \mathbf{a}_2 \\ \mathbf{a}_2^H \mathbf{a}_1 & \mathbf{a}_2^H \mathbf{a}_2 \end{bmatrix}^{-1} = \frac{1}{M^2 - \beta^2} \begin{bmatrix} M & -\beta \\ -\beta & M \end{bmatrix}$$

where $\beta = \mathbf{a}_1^H \mathbf{a}_2$, and we have used $\mathbf{a}_1^H \mathbf{a}_1 = \mathbf{a}_2^H \mathbf{a}_2 = M$. Note that we use the centered steering vector in (3.8) so that β is real-valued. Hence, the projection matrix can be expressed as

$$\mathbf{P}_A(\psi_1, \psi_2) = \frac{1}{M^2 - \beta^2} (M \mathbf{a}_1 \mathbf{a}_1^H - \beta \mathbf{a}_1 \mathbf{a}_2^H - \beta \mathbf{a}_2 \mathbf{a}_1^H + M \mathbf{a}_2 \mathbf{a}_2^H) \quad (5.2)$$

Using (5.2), it is possible to directly calculate (5.1) using

$$\begin{aligned} c(\psi_1, \psi_2) &= \frac{1}{N} \sum_{i=1}^N \mathbf{x}(i)^H \mathbf{P}_A(\psi_1, \psi_2) \mathbf{x}(i) \\ &= \frac{1}{N(M^2 - \beta^2)} \sum_{i=1}^N M |y_1(i)|^2 - 2\beta \operatorname{Re}\{y_1(i)^* y_2(i)\} + M |y_2(i)|^2 \end{aligned} \quad (5.3)$$

where $y_1(i) = \mathbf{a}_1^H \mathbf{x}(i)$ and $y_2(i) = \mathbf{a}_2^H \mathbf{x}(i)$, $i = 1, \dots, N$. Provided all steering vectors are available on the discrete grid, a significant part of the computational cost, required to evaluate a single point of (5.3), constitutes the calculation of $y_1(i)$, $y_2(i)$, and β , which corresponds to $C_1 = 8MN + 2M$ real-valued multiply-add operations. When the number of snapshots is small, the remaining operations do not significantly contribute to the overall cost. Note that, generally in the case with multiple snapshots, one has to trade off between the evaluation of the quadratic term above and the trace notation in (5.1).

5.2.2 Global search

Due to the complicated multimodal shape of objective function $c(\psi_1, \psi_2)$, a numerical search procedure, e.g. using a damped Newton method, critically depends on the initialization [OVS93]. A reliable initialization without eigendecomposition appears difficult to find, especially when the targets are not resolved in the BF spectrum. In the two-target case, a heuristic search procedure has been presented in [Sch10], which shows good simulative results. However, we consider a different approach here, namely a brute-force evaluation of the two-dimensional objective function on a selected grid. Unlike numerical search procedures, this allows a non-iterative implementation.

A global evaluation of the objective function is required for $\psi_1 < \psi_2$ only, because we have $c(\psi_1, \psi_2) = c(\psi_2, \psi_1)$. Figure 5.1 (top right) shows the resulting triangular search

range. The corresponding computational cost is

$$C = C_1 N_2, \quad N_2 = \frac{N_\psi(N_\psi - 1)}{2}$$

where C_1 represents the computational cost, required to evaluate a single point of the objective function, N_2 is the number of points in the two-dimensional search range, and N_ψ is the number of grid points in the field-of-view. When the global search is done on a discrete grid, the estimation accuracy is limited by step size $\Delta\psi$. The final estimate can be improved by an interpolation in the neighborhood of the optimum, as described in Section 3.A.1.

5.3 Proposed approach

In the following, we aim at reducing the computational cost of the described global search [HZ11a]. A simplified calculation of the objective function is proposed in Section 5.3.1, where the required projection operators are pre-calculated off-line and stored. For saving storage space and computations, in Section 5.3.2, we consider a delimited search range, based on a circular shift of the field-of-view. In Section 5.3.3, an example is presented to demonstrate the proposed approach.

5.3.1 Simplified objective function calculation

Since the projection matrix has a great deal of structure to exploit, we aim at simplifying the calculation of the objective function.

Proposition 1: Projection matrices of ULA steering vectors are centro-Hermitian, i.e. they remain unchanged after complex conjugation and interchanging the columns and rows. For exchange matrix \mathbf{J}_M of dimension M , we have

$$\mathbf{J}_M \mathbf{P}_A^* \mathbf{J}_M = \mathbf{P}_A.$$

Proof: The centered steering vector from (3.8) satisfies $\mathbf{J}_M \mathbf{a}(\psi)^* = \mathbf{a}(\psi)$ by definition. Consequently, we also have $\mathbf{J}_M \mathbf{A}^* = \mathbf{A}$, $\mathbf{A}^T \mathbf{J}_M = \mathbf{A}^H$, and it is easy to see that using $\mathbf{J}_M \mathbf{J}_M = \mathbf{I}_M$, we have

$$\mathbf{J}_M [\mathbf{A}(\mathbf{A}^H \mathbf{A})^{-1} \mathbf{A}^H]^* \mathbf{J}_M = \mathbf{J}_M \mathbf{A}^* (\mathbf{A}^T \mathbf{J}_M \mathbf{J}_M \mathbf{A}^*)^{-1} \mathbf{A}^T \mathbf{J}_M = \mathbf{A} (\mathbf{A}^H \mathbf{A})^{-1} \mathbf{A}^H$$

which concludes the proof. We note that, as reported in [HZ11a], the centro-Hermitian property also holds for non-centered ULA steering vectors. \square

As a consequence, the ML objective function in (5.1) remains unchanged when snapshot \mathbf{x} is replaced by $\mathbf{J}_M \mathbf{x}^*$, since

$$(\mathbf{J}_M \mathbf{x}^*)^H \mathbf{P}_A(\psi_1, \psi_2) \mathbf{J}_M \mathbf{x}^* = [\mathbf{x}^H \mathbf{J}_M \mathbf{P}_A(\psi_1, \psi_2)^* \mathbf{J}_M \mathbf{x}]^* = \mathbf{x}^H \mathbf{P}_A(\psi_1, \psi_2) \mathbf{x}$$

where we have used the fact that $c(\psi_1, \psi_2)$ is real-valued by definition. Therefore, ML estimation cannot benefit when FB averaging is employed.

5.3.1.1 Unitary transformation

The computation of (5.1) can be simplified using the idea in [Lee80,HN95]. We consider the trace notation, as it is based on the sample covariance and can be directly applied in the case with multiple snapshots.

Let \mathbf{Q}_M be a column conjugate symmetric matrix, satisfying $\mathbf{J}_M \mathbf{Q}_M^* = \mathbf{Q}_M$. A sparse choice for a unitary column conjugate symmetric matrix is

$$\mathbf{Q}_{2m+1} = \frac{1}{\sqrt{2}} \begin{bmatrix} \mathbf{I}_m & \mathbf{0} & j\mathbf{I}_m \\ \mathbf{0}^T & \sqrt{2} & \mathbf{0}^T \\ \mathbf{J}_m & \mathbf{0} & -j\mathbf{J}_m \end{bmatrix}.$$

An equivalent matrix of dimension $2m$ can be obtained by deleting the center row and center column of \mathbf{Q}_{2m+1} . The main result of [Lee80] is summarized in the following proposition, which states that any square centro-Hermitian matrix is equivalently expressed by a real-valued matrix of the same dimension.

Proposition 2: Let $\mathbf{A} \in \mathbb{C}^{M \times M}$ be centro-Hermitian, so that we have $\mathbf{J}_M \mathbf{A}^* \mathbf{J}_M = \mathbf{A}$, and let \mathbf{Q}_M be a unitary column conjugate symmetric matrix, as defined above. Then

$$\mathbf{B} = \mathbf{Q}_M^H \mathbf{A} \mathbf{Q}_M$$

is real-valued. This similarity transformation with a unitary matrix is referred to as unitary transformation.

Proof: From the column conjugate symmetric property it is easy to see that we also have $\mathbf{Q}_M^T \mathbf{J}_M = \mathbf{Q}_M^H$. Therefore, using $\mathbf{J}_M \mathbf{J}_M = \mathbf{I}_M$ and the centro-Hermitian property of \mathbf{A} , we have

$$\mathbf{B}^* = \mathbf{Q}_M^T \mathbf{A}^* \mathbf{Q}_M^* = \mathbf{Q}_M^T \mathbf{J}_M \mathbf{J}_M \mathbf{A}^* \mathbf{J}_M \mathbf{J}_M \mathbf{Q}_M^* = \mathbf{Q}_M^H \mathbf{A} \mathbf{Q}_M = \mathbf{B}$$

which concludes the proof. □

Since the ML objective function remains unchanged when $\mathbf{x}(i)$ is replaced by $\mathbf{J}_M \mathbf{x}(i)^*$, we can replace $\hat{\mathbf{R}}$ by the FB averaged covariance matrix

$$\hat{\mathbf{R}}_{\text{FB}} = \frac{1}{2}(\hat{\mathbf{R}} + \mathbf{J}_M \hat{\mathbf{R}}^* \mathbf{J}_M)$$

which is centro-Hermitian by definition. Using the result from the above propositions, we can use a unitary transformation to obtain the real-valued sample covariance and real-valued projection operators, respectively, as

$$\hat{\mathbf{C}} = \mathbf{Q}_M^H \hat{\mathbf{R}}_{\text{FB}} \mathbf{Q}_M \quad (5.4)$$

$$\mathbf{V}(\psi_1, \psi_2) = \mathbf{Q}_M^H \mathbf{P}_A(\psi_1, \psi_2) \mathbf{Q}_M. \quad (5.5)$$

This approach has been used in [HN95] and [PGH00], respectively, to derive the unitary ESPRIT and unitary root-MUSIC algorithm. Here, the computational cost is reduced by replacing a complex-valued by a real-valued eigendecomposition.

Using expressions (5.4) and (5.5), and the fact that $\mathbf{Q}_M \mathbf{Q}_M^H = \mathbf{I}_M$, the objective function in (5.1) can be rewritten as

$$\begin{aligned} c(\psi_1, \psi_2) &= \text{Tr}\{\mathbf{P}_A(\psi_1, \psi_2) \hat{\mathbf{R}}\} = \text{Tr}\{\mathbf{P}_A(\psi_1, \psi_2) \hat{\mathbf{R}}_{\text{FB}}\} \\ &= \text{Tr}\{\mathbf{P}_A(\psi_1, \psi_2) \mathbf{Q}_M \mathbf{Q}_M^H \hat{\mathbf{R}}_{\text{FB}} \mathbf{Q}_M \mathbf{Q}_M^H\} \\ &= \text{Tr}\{\mathbf{Q}_M^H \mathbf{P}_A(\psi_1, \psi_2) \mathbf{Q}_M \mathbf{Q}_M^H \hat{\mathbf{R}}_{\text{FB}} \mathbf{Q}_M\} \\ &= \text{Tr}\{\mathbf{V}(\psi_1, \psi_2) \hat{\mathbf{C}}\} \end{aligned} \quad (5.6)$$

Furthermore, for the computation of the trace in (5.1) and (5.6), only the diagonal entries of the matrix product need to be evaluated. Thus, introducing the vectorization operator $\text{vec}\{\cdot\}$, we can use the identity

$$\text{Tr}\{\mathbf{A}\mathbf{B}\} = \text{vec}\{\mathbf{A}^T\}^T \text{vec}\{\mathbf{B}\}$$

for arbitrary square matrices $\mathbf{A}, \mathbf{B} \in \mathbb{C}^{M \times M}$. Also, we exploit that real-valued matrices $\mathbf{V}(\psi_1, \psi_2)$ and $\hat{\mathbf{C}}$ are symmetric so that the computational complexity required for the evaluation of the trace in (5.6) can further be reduced. Towards this end, let

$$\text{sym}\{\mathbf{A}\} = [a_{11}, a_{12}, a_{22}, a_{13}, a_{23}, a_{33}, a_{14}, \dots, a_{MM}]^T$$

which selects matrix elements $a_{mn} = [\mathbf{A}]_{m,n}$ with $m \leq n$ from symmetric $\mathbf{A} \in \mathbb{R}^{M \times M}$, and stacks them into a vector of dimension $M_2 = M(M+1)/2$. In other words, this operator removes redundant matrix entries. Further, let $\mathbf{l} = [1, 2, 1, 2, 2, 1, 2, \dots, 1]^T$

be a scaling vector of the same dimension, being 2 for off-diagonal entries and 1 for diagonal entries of $\text{sym}\{\mathbf{A}\}$. Now, we can rewrite

$$c(\psi_1, \psi_2) = \text{Tr}\{\mathbf{V}(\psi_1, \psi_2)\hat{\mathbf{C}}\} = \mathbf{v}(\psi_1, \psi_2)^T \hat{\mathbf{c}} \quad (5.7)$$

with

$$\begin{aligned} \mathbf{v}(\psi_1, \psi_2) &= \text{sym}\{\mathbf{V}(\psi_1, \psi_2)\} \odot \mathbf{l} \\ \hat{\mathbf{c}} &= \text{sym}\{\hat{\mathbf{C}}\} \end{aligned}$$

Note that $\hat{\mathbf{c}}$ has to be calculated only once. The key idea for a fast implementation is that projection operators $\mathbf{v}(\psi_1, \psi_2)$ are pre-calculated for every point, $\psi_1 < \psi_2$, in the search range. The required storage space is $M_2 N_2$ real-valued numbers. In this case, the simplified computation using (5.7) requires only $C_1 = M_2$ real-valued multiply-add operations. The speed-up, when compared to (5.1), is roughly factor 8.

5.3.1.2 Single-snapshot alternative

In the case with a single snapshot, an alternative is to employ an eigendecomposition of the real-valued projection operator in (5.5),

$$\mathbf{V}(\psi_1, \psi_2) = \mathbf{v}_1 \mathbf{v}_1^T + \mathbf{v}_2 \mathbf{v}_2^T$$

with eigenvectors $\mathbf{v}_1, \mathbf{v}_2 \in \mathbb{R}^{M \times 1}$. Note that \mathbf{v}_1 and \mathbf{v}_2 are both functions of ψ_1 and ψ_2 . Using $\mathbf{y} = \mathbf{Q}_M^H \mathbf{x}$, the objective function can be rewritten as

$$c(\psi_1, \psi_2) = \mathbf{y}^H \mathbf{V}(\psi_1, \psi_2) \mathbf{y} = \mathbf{y}^H (\mathbf{v}_1 \mathbf{v}_1^T + \mathbf{v}_2 \mathbf{v}_2^T) \mathbf{y} = |z_1|^2 + |z_2|^2 \quad (5.8)$$

with scalars $z_1 = \mathbf{y}^H \mathbf{v}_1$ and $z_2 = \mathbf{y}^H \mathbf{v}_2$.

Note that \mathbf{y} has to be calculated only once. The key idea is again that the eigenvectors of the real-valued projection matrix are pre-calculated for every point, $\psi_1 < \psi_2$ in the search range. The required storage space then is $2MN_2$ real-valued numbers. The main part of the computational cost, required to evaluate a single point of (5.8), constitutes the calculation of z_1 and z_2 , which corresponds to $C_1 = 4M$ real-valued multiply-add operations.

5.3.1.3 Comparison

The overall cost of a global search has been described in Section 5.2.2. A trade-off between the computations, required for evaluating a single point of the objective

Table 5.1. Computations, required for evaluating a single point of the objective function, C_1 , and storage space, for the single-snapshot case, using $N_2 = N_\psi(N_\psi - 1)/2$.

	C_1	Storage space
Direct (5.3)	$10M$	$N_\psi 2M$
Simplified (5.7)	$M(M + 1)/2$	$N_2 M(M + 1)/2$
Simplified (5.8)	$4M$	$N_2 2M$

function, C_1 (in real-valued multiply-add operations), and the required storage space (in real-valued numbers) is given in Table 5.1 for the single-snapshot case. Note that the calculation of projection operators is done off-line and does not contribute to the overall cost. Also, the pre-processing, such as the formation of the covariance matrix, has no significant effect, as it is performed only once.

For an 8-element ULA and a single snapshot, the simplified objective function in (5.8) slightly outperforms (5.7), both in terms of required computations and storage space. However, when multiple snapshots are available, we prefer the simplified objective function in (5.7). In conclusion, the presented methods allow a trade-off between computational cost and storage space, which is achieved by a pre-calculation of data-independent projection operators.

We have seen in Table 5.1 that the storage space grows with N_2 . Also the DOA estimation performance in terms of accuracy and resolution is directly influenced by the step size $\Delta\psi$, and thus N_2 . Since on a practical system, the storage space may be limited, we propose to save storage space and computations in the next section.

5.3.2 Delimited search range

In the previous section, we have reduced the computational cost by proposing simplified objective functions. Next, we consider a delimiting search range, so that the number of points to evaluate and the storage space for the projection operators is reduced.

5.3.2.1 Circular shift

As mentioned above, we only consider the more difficult case of closely spaced targets, which cannot be reliably resolved. Let $\hat{\psi}_M \in [\psi_1, \psi_2]$ be an estimate of the midpoint

of the possibly unresolved targets. Consider the shifted array output model, which is obtained by a rotational shift of the field-of-view

$$\mathbf{x}' = \mathbf{a}(\hat{\psi}_M)^* \odot \mathbf{x} = s_1 \underbrace{\mathbf{a}(\hat{\psi}_M)^* \odot \mathbf{a}(\psi_1)}_{\mathbf{a}(\psi'_1)} + s_2 \underbrace{\mathbf{a}(\hat{\psi}_M)^* \odot \mathbf{a}(\psi_2)}_{\mathbf{a}(\psi'_2)} + \underbrace{\mathbf{a}(\hat{\psi}_M)^* \odot \mathbf{e}}_{\mathbf{e}'} \quad (5.9)$$

where $\psi'_1 = \psi_1 - \hat{\psi}_M$ and $\psi'_2 = \psi_2 - \hat{\psi}_M$ are the shifted DOA parameters, which are centered around broadside. The random characteristics of the circular shifted noise vector remain unchanged.

This rotational shift allows to evaluate $c(\psi'_1, \psi'_2)$ only on a delimited search range, e.g. $\psi' \in [-1.5\text{BW}_\psi, 1.5\text{BW}_\psi]$, which very likely contains the centered DOA parameters. Thus, the number of grid points to evaluate, as well as the amount of projection operators to store, can be reduced significantly. This strategy is demonstrated in an example in Section 5.3.3.

5.3.2.2 Midpoint estimation

The proposed strategy for delimiting the search range does not critically depend on the accuracy of the midpoint estimate. However, $\hat{\psi}_M$ should not be too far away from the true midpoint. A simple approach would be to take the location of the maximum of the BF spectrum, which represents a good choice, when the target are not resolved, and is calculated anyway in the proposed array processing. Hence, $\hat{\psi}_M = \hat{\psi}_0$.

However, we have seen in Section 4.1.1 that in the case with a single snapshot, there are some relative phases, for which the targets are resolved in the BF spectrum, even when their angular separation is below BW_ψ . In this case, there is a large bias, and one may want to use ML estimation to guarantee accurate DOA estimation. Note also, that the proposed method for bias correction does not work reliably in this case. Consequently, $\hat{\psi}_0$ may not lie between ψ_1 and ψ_2 , and therefore, when used as a midpoint estimate, the target parameters may not lie in the delimited search range. An alternative is to use a center-of-mass (COM) estimate, defined by

$$\hat{\psi}_M = \frac{\sum_{\psi_k \in \Omega} \psi_k P_{\text{BF}}(\psi_k)^{0.5}}{\sum_{\psi_k \in \Omega} P_{\text{BF}}(\psi_k)^{0.5}}$$

where Ω is a local neighborhood around $\hat{\psi}_0$, e.g. all grid points between $\hat{\psi}_0 \pm 1.5\text{BW}_\psi$. This estimate is generally not sensitive to situations when the target are resolved in the BF spectrum for some relative phases. The COM estimate has to be calculated additionally, however, at a moderate cost.

5.3.3 Example

Before demonstrating this strategy with an example, we briefly summarize the approach. Let $\psi'_1 < \psi'_2 \in [-1.5\text{BW}_\psi, 1.5\text{BW}_\psi]$ be the two-dimensional delimited search range, for which the real-valued projection operators $\mathbf{v}(\psi'_1, \psi'_2)$ are available on a discrete grid with step size $\Delta\psi$. The developed practicable implementation is summarized as follows:

1. Estimate the midpoint, $\hat{\psi}_M$, from the BF spectrum, and circularly shift the data using $\mathbf{x}(i)' = \mathbf{a}(\hat{\psi}_M)^* \odot \mathbf{x}(i)$, so that parameters ψ'_1 and ψ'_2 lie in the delimited search range.
2. Calculate the real-valued covariance vector $\hat{\mathbf{c}}$ from $\hat{\mathbf{x}}(i)'$, $i = 1, \dots, N$.
3. Evaluate $c(\psi'_1, \psi'_2)$ on the selected grid using (5.7).
4. Determine the location of the global maximum (optionally, one can evaluate a few more grid points around the global maximum, with a refined step size, e.g. using the direct calculation in Section 5.2.1). Note that if the global maximum appears at the borders of the search range, the single-target model with $\hat{\psi}_0$ should be preferred.
5. Calculate the final DOA estimates using a quadratic interpolation in the neighborhood of the global maximum, as described in Section 3.A.1. Finally, perform the inverse circular shift operation $\hat{\psi}_i = \hat{\psi}'_i + \hat{\psi}_M$.

The main part of the computational cost constitutes the evaluation of ML objective function in step 3. This involves a simple matrix vector product, which is easy to parallelize. The calculations required in steps 4-5, which involve a global maximum search and simple scalar multiply-add operations, do not significantly contribute to the overall cost.

Regarding the example, we consider an 8-element ULA, the noise-free case, and two targets with angular separation $\delta = 0.75\text{BW}_\psi$, relative phase $\varphi = \pi/4$ and power ratio $\rho = 0.5$, as defined in (3.11). Figure 5.1 shows the BF spectrum of the original (top left) and shifted snapshot (bottom left). The two targets are not resolved, but the position of the midpoint can be used to identify the relevant sector for the delimited search range, indicated by the black dotted lines. For simplicity, the midpoint has been determined as the grid location of the maximum. Also shown in Figure 5.1 is

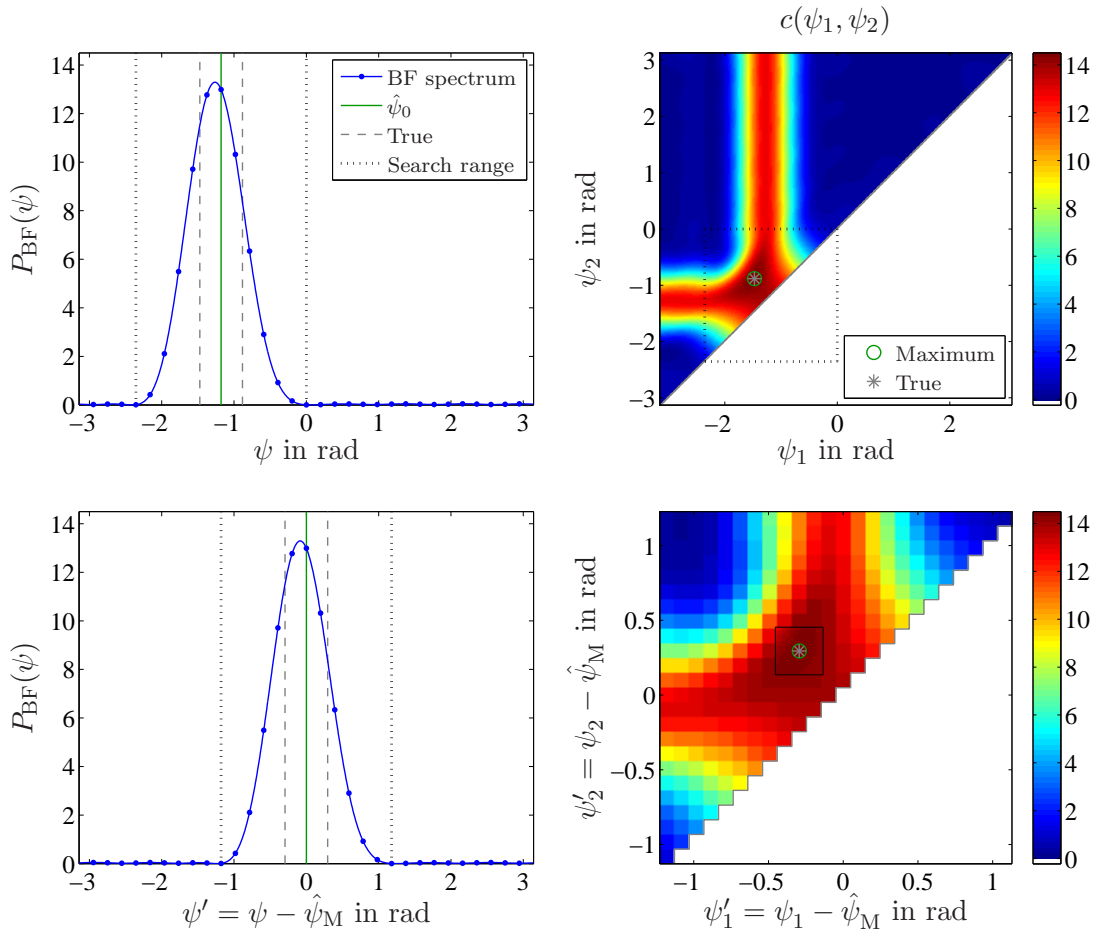


Figure 5.1. Example of the proposed ML search. Two targets with angular separation $\delta = 0.75BW_\psi$, relative phase $\varphi = \pi/4$ and power ratio $\rho = 0.5$. BF spectrum to identify relevant angular sector (top left), ML objective function for full search range (top right), shifted BF spectrum (bottom left), and ML objective function for shifted and delimited search range with coarse and refined search (bottom right).

the ML objective function for the full search range on a grid with $\Delta\psi = \pi/128$ (top right), and for the delimited search range with $\Delta\psi = \pi/32$ (bottom right). For the proposed delimited search, a refined search has been carried out in the vicinity of the global maximum, to achieve the same accuracy as the full search, but with significantly reduced points to evaluate.

5.4 Simulation results

Simulations are used to assess the performance of the proposed approach. We consider an 8-element ULA, the single-snapshot case, and two targets with power ratio $\rho = 0.5$ and relative phase φ , which is uniformly distributed between 0 and 2π . In simulations,

we vary angular separation δ and SNR. For a fair assessment of grid search DOA estimation, in each simulation run, we add a random jitter, uniformly distributed between $\pm\Delta\psi/2$, to the DOA parameters.

We compare the performance of the proposed implementation with the CRB from (3.19). As performance metric for DOA estimation, we consider the RMSE of the first target, defined by

$$\text{RMSE}_1^2 = \frac{1}{\text{MC}} \sum_{k=1}^{\text{MC}} (\hat{\psi}_{1,k} - \psi_1)^2$$

where $\hat{\psi}_{1,k}$ is the DOA estimate of the first target in run k and $\text{MC} = 10^4$. First, we present results for the midpoint estimation approach. Second, the performance of the proposed ML implementation is simulated versus angular separation for several SNR values. Third, we investigate the effect of the step size $\Delta\psi$. Finally, the proposed implementation is compared with selected computationally efficient algorithms.

5.4.1 Midpoint estimation

For estimating the midpoint, we consider the location of the maximum of the BF spectrum, and the COM, as defined in Section 5.3.2.2. For a delimited search on $\psi_1 < \psi_2 \in [-1.5\text{BW}_\psi, 1.5\text{BW}_\psi]$, we require the midpoint estimation error to be less than 0.75BW_ψ , so that the shifted parameters are in the delimited search range. Consequently, we are more interested in a maximum error than an average error, and consider the 0.95-quantile of $|\hat{\psi}_M - \psi_M|$ as a suitable performance metric. For the calculation of the BF spectra, we use an FFT with $4M$ grid points and a Chebyshev window with a sidelobe attenuation of 20 dB. We vary angular separation δ at $\text{SNR} = 20$ dB. The results are shown in Figure 5.2. One can observe that both the maximum of the BF spectrum and the COM are able to produce midpoint estimates within the desired range. However, when the angular separation is larger, the COM produces more reliable results and seems to be more appropriate.

5.4.2 Angular separation

We simulate DOA estimation accuracy of the proposed approach versus angular separation for various SNR values. We consider the same search principle as in Section 5.3.3, i.e. a coarse search with $\Delta\psi = \pi/32$ on the delimited search range, and a refined search in the vicinity of the global maximum with $\Delta\psi = \pi/128$ to achieve a good accuracy.

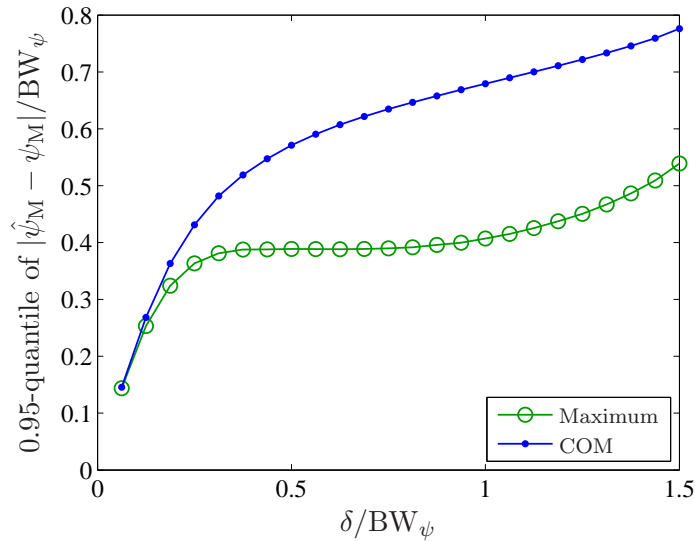


Figure 5.2. Simulation results for midpoint estimation between two targets. Empirical 0.95-quantile of $|\hat{\psi}_M - \psi_M|$ versus angular separation δ at SNR = 20 dB.

The results are shown in Figure 5.3. Note that we only show simulation points, for which more than 95% of trials are successfully resolved. One can observe that the results are close to the respective CRB. At the onset point, the super-efficient behavior can be explained by the delimited search range, since we provide the information of the relevant sector, and thereby reduce the error magnitude.

There is an interesting connection to Figure 4.9, which represents a similar simulation setup. Consider e.g. the cases with SNR = 15 dB and 20 dB, for which the multiple target detection approach is able to detect 95% of the two-target cases for angular separations above roughly $0.6BW_\psi$ and $0.4BW_\psi$. This approximately coincides with the onset points in Figure 5.3. Hence, the detection method has detected only those cases, for which ML estimation is able to work reliably.

5.4.3 Effect of step size

We first simulate the performance of the proposed method, calculated via (5.7), for step sizes $\Delta\psi = \pi/32$ and $\pi/64$. We additionally consider a refined search by $\Delta\psi/4$ around the global maximum, with effective step sizes $\pi/128$ and $\pi/256$. We vary the SNR for angular separation $\delta = 0.5BW_\psi$. Figure 5.4 shows the obtained results. One can observe that for moderate SNR the proposed method can achieve the CRB. For high SNR values, the average error converges to a finite accuracy, which depends on the step size.

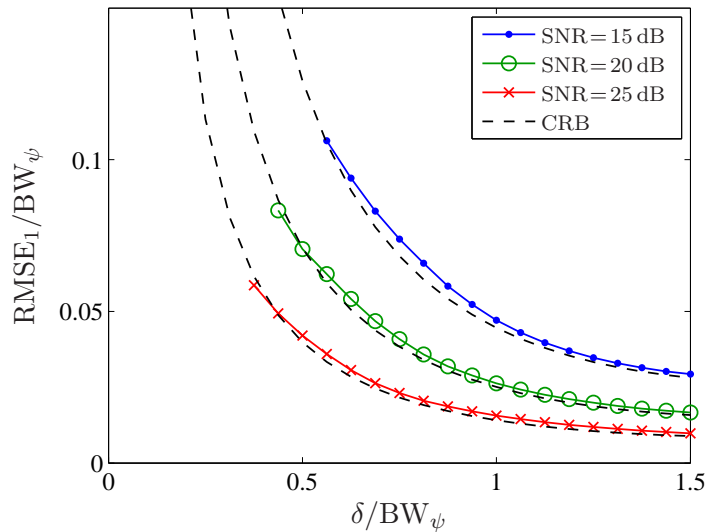


Figure 5.3. Simulation results for the developed ML DOA estimate of two targets. RMSE versus angular separation δ for various SNR.

We note that in practice, an SNR of significantly more than 30 dB can be considered as unrealistic. Moreover, often an accuracy of less 5% of the Rayleigh BW is sufficient for certain applications. In that case, the simplest approach with step size $\Delta\psi = \pi/32$ without refinement is adequate.

5.4.4 Comparison with selected algorithms

Finally, the proposed ML implementation is compared with selected computationally efficient algorithms in terms of performance and computation time. For this, we consider the IQML algorithm, unitary ESPRIT and a fast ML method for two target in beamspace (BS). IQML [BM86] is based on a polynomial representation of the projection matrix, whose order corresponds to the number of targets. In each iteration, a symmetric banded Toeplitz matrix has to be inverted, and a polynomial update results from normal equations of a whitened covariance matrix. After convergence, DOA estimates are obtained by the polynomial roots. The convergence condition is set to 10^{-4} . Unitary ESPRIT [HN95] is a subspace method and requires an eigendecomposition of the real-valued sample covariance matrix $\hat{\mathbf{C}}$ in Section 5.3.1.1. The DOA estimates are obtained analytically, by solving an LS problem and eigendecomposition of dimension two. We generate multiple snapshots using three overlapping subarrays. The considered ML method for two target in BS [ZL91] uses a BS transformation with three orthogonal beams. In this case, for $N \geq 3$, the DOA estimates can be obtained analytically by solving a second order polynomial, which results from an eigendecomposition

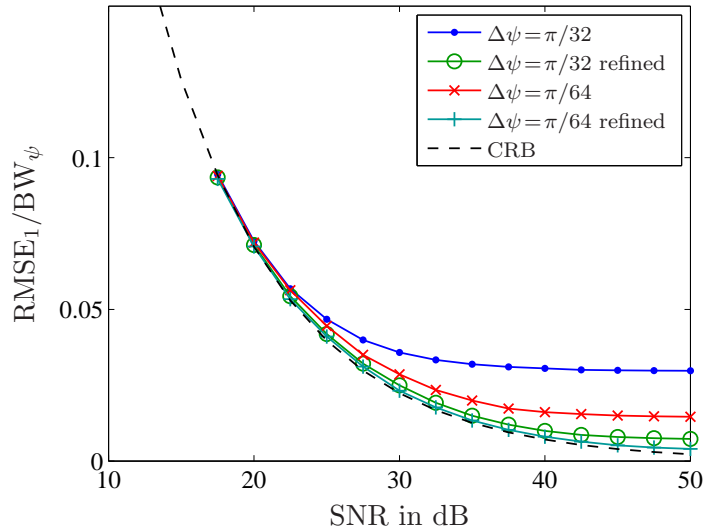


Figure 5.4. Simulation results for the developed ML DOA estimate of two targets. RMSE versus SNR for angular separation $\delta = 0.5BW_\psi$ and various step sizes $\Delta\psi$.

of a BS sample covariance matrix. Again, we generate multiple BS snapshots by using three overlapping subarrays. The considered algorithms are described in detail in the appendix of this chapter.

The performance comparison with the described methods is given in Figure 5.5 (top), in which we show the RMSE versus SNR with angular separations $\delta = 0.5BW_\psi$. It can be observed that all methods perform similarly well, close to the CRB. However, for small SNR, the proposed implementation of the brute-force search slightly outperforms the other approaches. Also, unitary ESPRIT provides 95% successful trials only above 20 dB. For high SNR, the proposed implementation converges to a finite accuracy due to the grid search.

Regarding computational cost, the simulations have been conducted on a Windows PC with an Intel Core i7 processor at 2.67 GHz and 4 GB RAM. The MATLAB version is R2010a. Average CPU times have been computed using functions tic and toc. Figure 5.5 (bottom) shows the average CPU time versus SNR, which correspond to Figure 5.5 (top). Clearly, the ML method in BS is the fastest method, followed by unitary ESPRIT and the proposed implementation. IQML is the slowest method, due to an average number of ≈ 10 iterations. We note that this results is not representative, but gives a general idea. The performance of the developed approach in terms of DOA estimation and computational cost is roughly comparable with selected computationally efficient algorithms. However, it allows a straightforward and non-iterative implementation.

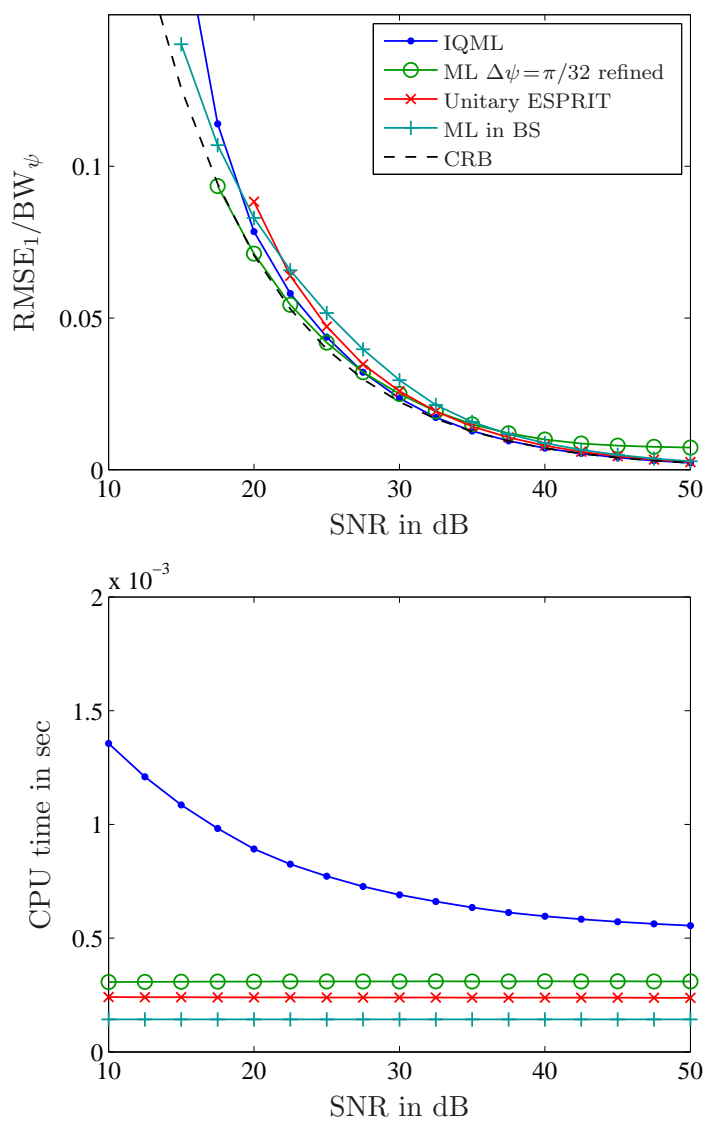


Figure 5.5. Simulation results and performance comparison for DOA estimation of two targets. RMSE versus SNR for angular separation $\delta = 0.5BW_\psi$ (top), average CPU time (bottom).

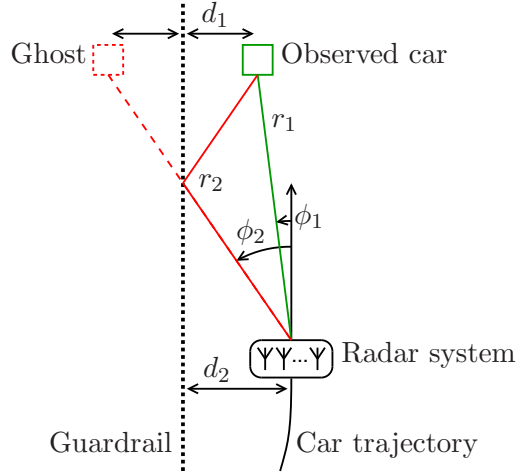


Figure 5.6. Automotive radar situation when there is multipath with the guardrail: geometry setup.

5.5 Experimental data example

We present results obtained with experimental data to demonstrate the practical value of the practicable implementation of the ML estimate for two targets. We consider a typical situation in an ACC application, in which the observed vehicle is driving on an left lane of the motorway, close to a guardrail. The radar echos from the vehicle consist of a direct path and an indirect specular path, which gives rise to a ghost target. The corresponding geometry setup is shown in Figure 5.6.

When the propagation paths are resolved, the observed vehicle can be accurately localized and a ghost target is identified. Otherwise, this can result in a false localization of the observed vehicle, which seems to be pulled towards the guardrail. Clearly, from the geometry in Figure 5.6, the range and angles are ideally related via

$$\begin{aligned} r_1 \sin(\phi_1) &= d_2 - d_1 \\ r_2 \sin(\phi_2) &= d_2 + d_1 \end{aligned}$$

where d_1 and d_2 are the normal distances from the guardrail. Note that the observed car and the ghost target fall into the same processing cell if $r_2 - r_1 < \Delta_r$, where Δ_r is the width of a range cell, and high-resolution becomes necessary when the angular separation $\phi_2 - \phi_1$ is smaller than the Rayleigh BW. To provoke this situation, we use an automotive radar system prototype for SRR applications, whose system parameters are given in Table 3.1. The bandwidth is set such that $\Delta_r = 1.8$ m, the corresponding Rayleigh BW around broadside is roughly 16.4° .

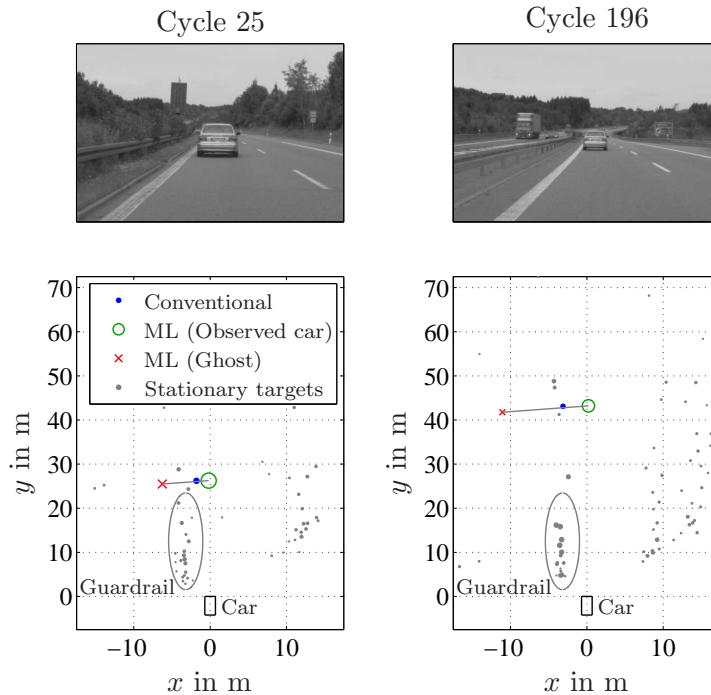


Figure 5.7. Experimental data analysis. Scenario and all detected and clustered targets in bird's eye view for two selected cycles.

In the considered recording, the vehicle with the mounted radar system is following another vehicle on the left lane of the motorway. In roughly 300 cycles, the observed vehicle is moving away, where the the range is increasing from roughly 25 m to 50 m. After the radar pre-processing, as described in Chapter 3, an initial DOA is determined using the location of the maximum of the BF spectrum. A clustering strategy is applied such that cells in neighboring range cells with similar relative velocity and initial DOA are merged. Subsequently, a gating procedure is used to extract relevant processing cells, i.e. whose relative velocity and initial DOA fall into a desired gate. The described ML method is applied to all relevant processing cells. For the detection, we use a GLRT, as described in Section 3.3, with threshold $\log \gamma_{\text{GLRT}} = 1.25M$.

For two selected cycles, a picture of the scene and a bird's eye view representation of the detected and clustered targets is shown in Figure 5.7. Grey dots correspond to stationary targets, while blue dots correspond to moving targets in the relevant gate. For both groups, a single-target DOA has been estimated using the BF. The result of the proposed ML for two targets is indicated with a green circle and red cross, corresponding to the observed car and ghost target, respectively, as in Figure 5.6. On average, the measured power of the ghost target is roughly 6 dB smaller than the power of the observed car. The markersize of all displayed targets is proportional to

the measured SNR. Note that the indicated stationary target detections can be used to localize the guardrail, which is required to identify the multipath situation.

Figure 5.8 shows the DOA estimation results of all cycles versus interpolated range. Note that the two selected cycles, 25 and 196, from Figure 5.7 are also indicated. We show the conventional result with single-target DOA estimation using the BF (top) and an improved result (bottom), where the proposed ML estimate of two targets is employed. Similarly to Figure 5.7, blue dots correspond to single-target DOA estimates using the BF, green circles and red crosses correspond to the observed car and ghost target, respectively, which have been estimated using the proposed ML estimator. One can observe that for the selected scenario the conventional single-target DOA estimation can result in a misleading target localization. This means that the target seems to be pulled towards the guardrail. When the multipath propagation is identified correctly, it is possible to apply the proposed ML estimator for two targets and adequately localize the car of interest and a ghost target.

5.6 Conclusion

In this chapter, the practically relevant problem of DOA estimation of two targets has been considered. For this case, we have developed a practicable implementation of the ML estimator, which is based on a simplified calculation of the objective function. The required projection operators are data-independent and can be pre-calculated, which enables a trade-off between computational complexity and storage space. For saving storage space and computations, we have proposed to use circular shift of the field-of-view such that the relevant angular sector, which has to be evaluated, is delimited and centered around broadside. The performance of the developed approach is analyzed in simulations, where it is shown to perform similarly to selected computationally efficient algorithms. The developed approach allows a straightforward and non-iterative implementation. It represents an interesting candidate for other radar systems, in which processing cells are represented by a single snapshot.

To demonstrate the practical value of the proposed method, we have presented results with real data from a typical situation of an ACC application with horizontal multipath. In this case, the developed approach for high-resolution DOA estimation allows to enhance the localization of the observed car.

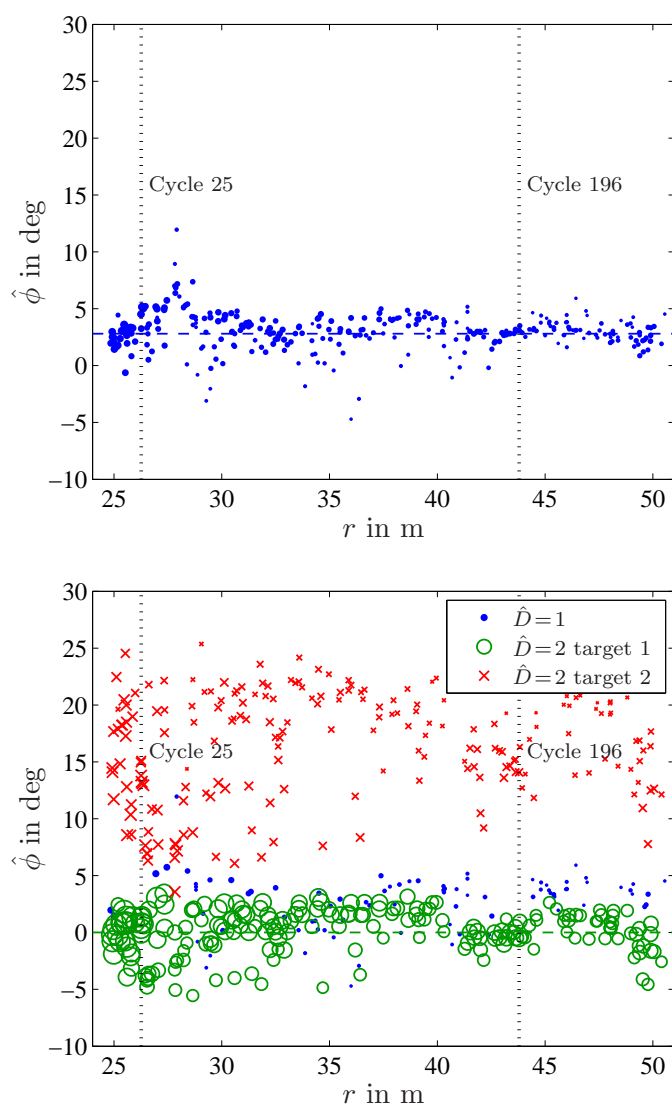


Figure 5.8. Experimental data analysis. DOA estimates versus range, conventional results with single-target DOA estimate from BF (top), improved results with ML estimation of two targets (bottom).

5.A Appendix

The IQML algorithm and unitary ESPRIT are described for an arbitrary number of targets. For the two-target case, we also consider the analytic ML algorithm in beamspace (BS) from [ZL91].

5.A.1 IQML

The IQML algorithm [BM86] is an iterative approach for minimizing the nonlinear LS cost function, as in (2.15). The idea is to exploit the ULA structure and reparameterize the orthogonal projection matrix using a basis for the nullspace of $\mathbf{A} = \mathbf{A}(\boldsymbol{\psi})$ [KV96]. Towards this end, one can define a polynomial with roots at $e^{j\psi_k}$, $k = 1, \dots, D$ as

$$\tilde{b}_0 + \tilde{b}_1 z + \dots + \tilde{b}_D z^D = \prod_{k=1}^D (z - e^{j\psi_k}) \quad (5.10)$$

where $\tilde{b}_D = 1$. By constructing a Toeplitz matrix $\tilde{\mathbf{B}} \in \mathbb{C}^{(M-D) \times M}$ with the polynomial coefficients as elements,

$$[\tilde{\mathbf{B}}]_{m,n} = \begin{cases} \tilde{b}_k^* & m - n = k, \quad k = 0, \dots, D \\ 0 & \text{otherwise} \end{cases}$$

one obtains $\tilde{\mathbf{B}}^H \mathbf{A} = \mathbf{0}$. Consequently, the columns of $\tilde{\mathbf{B}}$ form a basis for the nullspace of \mathbf{A}^H . This allows to reparameterize the orthogonal projection matrix as

$$\mathbf{P}_A^\perp(\boldsymbol{\psi}) = \tilde{\mathbf{B}}(\tilde{\mathbf{B}}^H \tilde{\mathbf{B}})^{-1} \tilde{\mathbf{B}}^H$$

which yields a modified optimization problem

$$\min_{\tilde{\mathbf{b}}} \frac{1}{N} \sum_{i=1}^N \mathbf{x}(i)^H \tilde{\mathbf{B}}(\tilde{\mathbf{B}}^H \tilde{\mathbf{B}})^{-1} \tilde{\mathbf{B}}^H \mathbf{x}(i) \quad (5.11)$$

with coefficient vector $\tilde{\mathbf{b}} = [\tilde{b}_0, \dots, \tilde{b}_D]^T$. Once $\hat{\mathbf{b}}$ is determined, the DOA estimates are found by the angles of the roots of polynomial (5.10). However, (5.11) is still difficult to solve. An iterative procedure with a simpler quadratic optimization can be obtained by fixing $(\tilde{\mathbf{B}}^H \tilde{\mathbf{B}})^{-1}$ in each iteration. Towards this end, let

$$\tilde{\mathbf{B}}^H \mathbf{x} = \mathbf{X} \tilde{\mathbf{b}}, \quad \mathbf{X} = [\mathbf{T}_{M-D,0} \mathbf{x}, \dots, \mathbf{T}_{M-D,D} \mathbf{x}]$$

where $\mathbf{T}_{M-k,l}$, $l = 0, \dots, k$ are subarray selection matrices, which consist of an identity matrix of dimension $M - k$ with l and $k - l$ zero columns arranged from left and right, respectively.

This allows to rewrite (5.10) as

$$\min_{\tilde{\mathbf{b}}} \tilde{\mathbf{b}}^H \hat{\mathbf{R}}_w \tilde{\mathbf{b}} \quad (5.12)$$

where

$$\hat{\mathbf{R}}_w = \frac{1}{N} \sum_{i=1}^N \mathbf{X}(i) \mathbf{X}(i)^H (\tilde{\mathbf{B}}^H \tilde{\mathbf{B}})^{-1} \mathbf{X}(i).$$

Note that (5.12) has a trivial solution and must be constrained such that $\tilde{\mathbf{b}} \neq \mathbf{0}$. An implementation with reduced dimensionality, which constrains the polynomial coefficient to be Hermitian symmetric, is described in [BM86]. An iterative procedure for determining $\hat{\mathbf{b}}$ can be summarized by:

1. Initialize $\hat{\mathbf{b}} = [1, 0, \dots, 0]^T$.
2. Form $\tilde{\mathbf{B}}$ from the recent $\hat{\mathbf{b}}$, and calculate $\hat{\mathbf{R}}_w$ (numerically efficient algorithms for the involved inversion of the banded Toeplitz matrix $\tilde{\mathbf{B}}^H \tilde{\mathbf{B}}$ are available [GvL96]).
3. Obtain an update of $\hat{\mathbf{b}}$ from an analytical solution of (5.12).
4. If the norm of the relative change of $\hat{\mathbf{b}}$ between two iterations is smaller than a predefined threshold, stop; otherwise go to step 2.

5.A.2 Unitary ESPRIT

ESPRIT [RK89] exploits the shift structure of \mathbf{A} . In particular, when considering a ULA with two maximally overlapping subarrays of size $M - 1$, we have

$$\mathbf{T}_{M-1,0} \mathbf{A} \Psi = \mathbf{T}_{M-1,1} \mathbf{A}, \quad \Psi = \text{diag}\{e^{j\psi_1}, \dots, e^{j\psi_D}\} \quad (5.13)$$

where $\mathbf{T}_{M-1,l}$, $l = 0, 1$ have been defined in Section 5.A.1. Since the signal subspace \mathbf{U}_s spans the same subspace as \mathbf{A} , it can be expressed as $\mathbf{U}_s = \mathbf{A} \mathbf{W}$ with non-singular square matrix \mathbf{W} . Hence, analogously to (5.13), we have

$$\mathbf{T}_{M-1,0} \mathbf{U}_s \underbrace{\mathbf{W}^{-1} \Psi \mathbf{W}}_{\Xi} = \mathbf{T}_{M-1,1} \mathbf{U}_s. \quad (5.14)$$

Since Ξ and Ψ are related via a similarity transformation, they share the same eigenvalues, which contain the DOA parameters. Employing the estimated signal subspace, obtained from $\hat{\mathbf{R}}$ in (2.9), Ξ can be estimated based on an LS approach

$$\hat{\Xi} = (\hat{\mathbf{U}}_s^H \mathbf{T}_{M-1,0}^T \mathbf{T}_{M-1,0} \hat{\mathbf{U}}_s)^{-1} \hat{\mathbf{U}}_s^H \mathbf{T}_{M-1,0}^T \mathbf{T}_{M-1,1} \hat{\mathbf{U}}_s$$

or a total LS approach [RK89]. From an eigendecomposition of $\hat{\Xi}$, the DOA estimates are found by the angles of the respective eigenvalues.

The idea of unitary ESPRIT [HN95] is to replace $\hat{\mathbf{R}}$ by the real-valued

$$\hat{\mathbf{C}} = \mathbf{Q}_M^H \hat{\mathbf{R}}_{\text{FB}} \mathbf{Q}_M$$

where unitary matrix \mathbf{Q}_M and FB averaged sample covariance matrix $\hat{\mathbf{R}}_{\text{FB}}$ are defined in Section 5.3.1.1. Thus, only a real-valued eigendecomposition is required, which roughly reduces the computational cost by a factor of four. For search-free DOA estimation using subspace methods, the eigendecomposition is considered as the main part of the computational cost [PGH00]. Let $\hat{\mathbf{E}}_s$ be the estimate of the real-valued signal subspace, obtained from $\hat{\mathbf{C}}$. Analogously to (5.14), we have

$$\mathbf{K}_0 \hat{\mathbf{E}}_s \boldsymbol{\Upsilon} \approx \mathbf{K}_1 \hat{\mathbf{E}}_s$$

where

$$\begin{aligned} \mathbf{K}_0 &= \mathbf{Q}_{M-1}^H (\mathbf{T}_{M-1,0} + \mathbf{T}_{M-1,1}) \mathbf{Q}_M \\ \mathbf{K}_1 &= \mathbf{Q}_{M-1}^H (\mathbf{T}_{M-1,0} - \mathbf{T}_{M-1,1}) \mathbf{Q}_M \end{aligned}$$

are real-valued modified selection matrices. Again, $\boldsymbol{\Upsilon}$ can be estimated based on an LS approach

$$\hat{\boldsymbol{\Upsilon}} = (\hat{\mathbf{E}}_s^T \mathbf{K}_0^T \mathbf{K}_0 \hat{\mathbf{E}}_s)^{-1} \hat{\mathbf{E}}_s^T \mathbf{K}_0^T \mathbf{K}_1 \hat{\mathbf{E}}_s$$

or a total LS approach [HN95]. From an eigendecomposition of this matrix, the DOA estimates are found by

$$\hat{\psi}_k = 2 \tan^{-1}(\hat{\omega}_k), \quad k = 1, \dots, D$$

where $\hat{\omega}_k$ are the eigenvalues of $\hat{\boldsymbol{\Upsilon}}$. It is noted in [HN95] that when the eigenvalues are complex-valued, the DOA estimates are considered as unreliable.

FB averaging is often used to enhance the estimate of the spatial covariance matrix [PK89], especially for small N , as it effectively doubles the number of snapshots. This can be useful since subspace methods require $N > D$ snapshots and non-coherent signals such that the signal subspace is fully represented. Another approach, referred to as spatial smoothing (SS), is to divide the ULA into maximally overlapping subarrays of size L . The corresponding SS sample covariance matrix is

$$\hat{\mathbf{R}}_{\text{SS}} = \frac{1}{M-L+1} \sum_{l=0}^{M-L} \mathbf{T}_{L,l} \hat{\mathbf{R}} \mathbf{T}_{L,l}^T$$

where $\mathbf{T}_{L,l}$, $l = 0, \dots, M-L$ have been defined in Section 5.A.1.

5.A.3 Beamspace maximum likelihood

A computationally efficient approach for DOA estimation of two targets in BS is described in [ZL91]. The solution can be obtained analytically without a numerical search procedure. Towards this end, consider the two-target model in BS

$$\mathbf{x}_{\text{bs}}(i) = \mathbf{S}_M^H \mathbf{x}(i) = s_1(i) \underbrace{\mathbf{S}_M^H \mathbf{a}(\psi_1)}_{\mathbf{b}(\psi_1)} + s_2(i) \underbrace{\mathbf{S}_M^H \mathbf{a}(\psi_2)}_{\mathbf{b}(\psi_2)} + \mathbf{S}_M^H \mathbf{e}(i), \quad i = 1, \dots, N$$

where \mathbf{S}_M is a BS transformation matrix and $\mathbf{b}(\psi)$ is the transformed steering vector. In the two-target case, it is sufficient to use three orthogonal beams in the angular sector of interest,

$$\mathbf{S}_M = [\mathbf{a}(-\text{BW}_\psi), \mathbf{a}(0), \mathbf{a}(\text{BW}_\psi)].$$

Note that when the DOA parameters are not within this angular sector, one can obtain a shifted array output by using the techniques from Section 5.3.2.1. Note that $\mathbf{b}(\psi)$ is real-valued when the centered steering vector from (3.8) is used [ZL91], which is assumed in the sequel. Since $\mathbf{S}_M^H \mathbf{S}_M = \mathbf{I}_3$, the transformed noise vector remains spatially white. The ML optimization problem in BS is [vT02]

$$\min_{\psi_1, \psi_2} \text{Tr}\{\mathbf{P}_B^\perp(\psi_1, \psi_2) \hat{\mathbf{R}}_{\text{bs}}\} \quad (5.15)$$

where

$$\mathbf{P}_B^\perp(\psi_1, \psi_2) = \mathbf{I}_3 - \mathbf{B}(\mathbf{B}^T \mathbf{B})^{-1} \mathbf{B}^T, \quad \mathbf{B} = [\mathbf{b}(\psi_1), \mathbf{b}(\psi_2)]$$

is the real-valued orthogonal projection matrix in BS, and

$$\hat{\mathbf{R}}_{\text{bs}} = \frac{1}{N} \sum_{i=1}^N \mathbf{x}_{\text{bs}}(i) \mathbf{x}_{\text{bs}}(i)^H.$$

is the BS sample covariance matrix of dimension three. Hence, the dimensionality of (5.15) is significantly reduced. Moreover, the orthogonal projection matrix has rank one and can be expressed as $\mathbf{P}_B^\perp(\psi_1, \psi_2) = \mathbf{v}\mathbf{v}^T$ with its principal eigenvector $\mathbf{v} = \mathbf{v}(\psi_1, \psi_2)$. Using this representation, an equivalent optimization problem is

$$\min_{\mathbf{v}} \mathbf{v}^T \text{Re}\{\hat{\mathbf{R}}_{\text{bs}}\} \mathbf{v}, \quad \text{subject to } \|\mathbf{v}\| = 1$$

whose solution corresponds to the eigenvector of $\text{Re}\{\hat{\mathbf{R}}_{\text{bs}}\}$ associated with the smallest eigenvalue. Once $\hat{\mathbf{v}} = [\hat{v}_1, \hat{v}_2, \hat{v}_3]^T$ is determined, one can use relationship $\mathbf{v}^T \mathbf{b}(\psi_k) = 0$, $k = 1, 2$ to determine the DOA estimates. An analytical solution is derived in [ZL91] using a polynomial rooting approach, which exploits the ULA structure and makes use of the fact that the three orthogonal beams in \mathbf{S}_M have several common roots. Hence,

$\hat{\psi}_1$ and $\hat{\psi}_2$ are found by the angles of the roots of polynomial $q_0 + q_1 z + q_0^* z^2$ with coefficients

$$q_0 = -\hat{v}_1 e^{j\pi/M} + \hat{v}_2 - \hat{v}_3 e^{-j\pi/M}, \quad q_1 = 2(\hat{v}_1 + \hat{v}_3) \cos\left(\frac{\pi}{M}\right) - 2\hat{v}_2 \cos\left(\frac{2\pi}{M}\right).$$

We note that this analytic solution requires $N > 2$ snapshots, such that $\text{Re}\{\hat{\mathbf{R}}_{\text{bs}}\}$ has full rank. In the case with a single snapshot or coherent signals, this can be achieved by using subarrays before the BS transformation. In this case, the SS sample covariance matrix in BS is

$$\hat{\mathbf{R}}_{\text{SS,bs}} = \frac{1}{M-L+1} \sum_{l=0}^{M-L} \mathbf{S}_L^H \mathbf{T}_{L,l} \hat{\mathbf{R}} \mathbf{T}_{L,l}^T \mathbf{S}_L$$

where $\mathbf{T}_{L,l}$, $l = 0, \dots, M-L$ have been defined in Section 5.A.1, and \mathbf{S}_L is constructed accordingly with an increased BW.

Chapter 6

Conclusions and outlook

In this thesis, novel techniques for antenna array processing have been developed. This includes a phase autocalibration algorithm for URA geometries, and practicable methods for high-resolution DOA estimation and detection in automotive radar. Conclusions are drawn in Section 6.1, and an outlook to possible future work is provided in Section 6.2.

6.1 Conclusions

First, we have considered the problem of two-dimensional DOA estimation using a URA in the presence of phase errors. For the practically relevant case with a single source, we have developed a simple and robust LS algorithm for phase autocalibration. The rotational ambiguity problem has been studied and a suitable constraint has been proposed. An approximate CRB and an analytical expression for the MSE performance of the proposed estimator have been presented. Simulation results show that the performance of the proposed estimator is close to the approximate CRB for both DOA estimation and phase calibration. Furthermore, we have extended the proposed algorithm for phase autocalibration to the case with multiple sources. Simulation results demonstrate that the proposed algorithm can be effectively used to enhance the resolution performance in the presence of phase errors.

Second, we have considered the problem of high-resolution DOA estimation and detection for a typical automotive radar system, which uses a pulsed radar principle and an array of receive antennas for DOA estimation. Here, we have identified the potential two-target case with a single snapshot to be practically relevant. An optimal approach for high-resolution DOA estimation and detection has been presented, which involves a GLRT and computationally intensive ML estimation of two targets. Since this approach can become intractable in real-time, we have developed a practicable approach with reduced complexity. The general idea is to pre-select the processing cells, in which only a single target is present or two targets are well separated. Thus, the computationally intensive ML estimation of two targets is carried out only if its high-resolution performance is required. When the targets are resolved in the BF spectrum, the resulting DOA estimates are generally biased due to leakage. For this case, we have

proposed a strategy for bias correction with low computational complexity. Results obtained from simulations and real data show that the performance of the developed algorithm is close to the ML estimate, but at a significantly lower computational cost. When the BF spectrum shows only a single significant peak, either a single target is present or two targets are unresolved. For this case, we have developed a computationally simple test to decide whether the model with a single target is appropriate. Consequently, ML estimation of two targets is carried out only if the single-target model is rejected. This strategy can substantially save computations, when situations with more than one target are unlikely. Finally, a practicable implementation for the ML estimator of two targets has been developed, which is based on a simplified objective function and a delimited search range. The required projection operators are data-independent and can be pre-calculated off-line, which enables a trade-off between computational complexity and storage space. In simulations, the developed approach is shown to perform similarly to selected computationally efficient algorithms, but allows a straightforward and non-iterative implementation.

The practical value of the proposed approach has been demonstrated using real data from experiments with a single and two corner reflectors, and from a typical situation of an ACC application. From the presented simulative and experimental results, the proposed processing chain is expected to perform similarly as the optimal approach, but with a significantly reduced computational cost.

6.2 Outlook

A discussion on possible future work is given in the following.

- The developed concepts for high-resolution DOA estimation and detection for automotive radar perform well with real data from selected examples. As a next stage, a real-time implementation and extensive validation with experimental data seems appropriate.
- For practical reasons, the proposed processing chain is limited to the case with two targets. An extension to the case with more than two targets is generally possible at an increased computational complexity. Note that under the assumption that at most two targets are unresolved, a separation of unresolved clusters can be achieved in the spatial Fourier domain. In this case, ML estimation of two targets can be applied in BS sectors, similar to the presented approach. Note that

BS processing generally offers a reduced computational complexity due to the decreased dimensionality. However, this is often achieved at the cost of an inferior DOA estimation performance [WF94].

- We assume that the imperfections after off-line calibration are negligible when compared to the measurement noise. However, when the array model perturbations are dominant, autocalibration becomes necessary. For instance, the considered approach can be applied to the automotive radar application. This involves a study of possible error model parameterizations. Also, criteria for determining suitable data for autocalibration have to be developed, and alignment techniques for resolving the rotational ambiguity, described in Section 2.4, have to be investigated.
- At close distances one can observe multiple scattering centers of typical vehicles [BY06, Eng11]. If these are resolved, orientation and elongation information can be extracted, which in turn can be exploited by recent advances in automotive radar target tracking and clustering [GSDB07]. If multiple scattering centers are within an unresolved cluster, an alternative approach is to model these using a multipole expansion, as proposed in [MWGH98], or similarly using the distributed jammer modeling in [GNB97].

List of Acronyms

ACC	Adaptive cruise control
A/D	Analog-to-digital
BF	Beamformer
BS	Beamspace
BW	Beamwidth
COM	Center-of-mass
CRB	Cramér-Rao bound
DFT	Discrete Fourier transform
DOA	Direction-of-arrival
DSP	Digital signal processing
ESPRIT	Estimation of signal parameters via rotational invariance techniques
FB	Forward/backward
FFT	Fast Fourier transform
FIM	Fisher information matrix
FSRA	Full speed range adaptive cruise control
GLRT	Generalized likelihood ratio test
HPBW	Half-power beamwidth
IF	Intermediate frequency
i.i.d.	Independent and identically distributed
IQML	Iterative quadratic maximum likelihood
LCA	Lane change assistant
LS	Least squares
MAP	Maximum a posteriori
ML	Maximum likelihood

MRR	Mid-range radar
MSE	Mean squared error
MUSIC	Multiple signal classification
NSF	Noise subspace fitting
pdf	Probability density function
RCS	Radar cross section
RELAX	Relaxation algorithm in [LS96]
RMSE	Root mean squared error
SLL	Sidelobe level
SNR	Signal-to-noise ratio
SRR	Short range radar
ULA	Uniform linear array
URA	Uniform rectangular array

List of Symbols

$ \cdot $	Absolute value
$\mathbf{0}$	Column vector of zeros with conformable dimension
$\mathbf{1}_n$	Column vector of n ones
$(\cdot)^*$	Complex conjugate
$\text{diag}\{\cdot\}$	Diagonal matrix operator
\odot, \otimes	Element-wise matrix product, Kronecker product
$E\{\cdot\}$	Ensemble average
$\hat{(\cdot)}$	Estimator
$\ \cdot\ $	Euclidian vector norm
$\mathbf{I}_M, \mathbf{J}_M$	Identity matrix and exchange matrix of dimension M
$\delta_{m,n}$	Kronecker delta function
$[\cdot]_{m,n}$	Matrix element at row m and column n
$(\cdot)^{-1}, (\cdot)^+$	Matrix inverse, Moore-Penrose pseudo inverse
$\text{sym}\{\cdot\}$	Nonredundant symmetric matrix vectorization operator
$\angle(\cdot)$	Phase of complex number
$\text{Re}\{\cdot\}, \text{Im}\{\cdot\}$	Real part and imaginary part
$(\cdot)^T, (\cdot)^H$	Transpose and complex conjugate transpose
$\text{Tr}\{\cdot\}$	Trace of a matrix
\mathbf{a}	Array steering vector
$\tilde{\mathbf{a}}$	Perturbed array steering vector
A, A_k	Amplitude of IF radar signal, parameter of target k
\mathbf{A}	Array steering matrix
\mathbf{ACRB}	Approximate CRB matrix for DOA and phase error estimation
B	Pulse bandwidth

c	Speed-of-light
$c(\cdot)$	ML objective function
$\hat{\mathbf{c}}$	Nonredundantly vectorized real-valued sample covariance matrix
C_1	Computational cost to evaluate a single point of ML objective function
$\hat{\mathbf{C}}$	Real-valued sample covariance matrix
CRB	CRB matrix
d	Element spacing of ULA
d_x, d_y	Element spacing in x - and y -direction of URA
D	Number of sources, number of targets per processing cell
e_{IF}	Noise term of IF radar signal
\mathbf{e}	Noise vector
E_{IF}	Noise term of IF radar signal after two DFTs
f_c	Carrier frequency
F_r, F_v, F_ϕ	Normalized frequencies according to range, relative velocity and azimuth angle
\mathbf{F}, \mathbf{G}	System matrices for URA autocalibration with one and multiple sources
i_r, i_v	DFT index according to range and relative velocity
$i_{r,k}, i_{v,k}$	DFT indices of extracted processing cell with target k
I_r, I_v	Number of DFT indices according to range and relative velocity
\mathbf{k}	Wavenumber vector
K	Number of targets
$\mathbf{L}_1, \mathbf{L}_2$	Selection matrices
M	Number of array elements
M_x, M_y	Number of elements in x - and y -direction of URA

$\mathbf{M}_\varphi, \mathbf{M}_\rho$	Rotational factor transformation matrices
MC	Number of Monte-Carlo runs
N	Number of snapshots
N_2	Number of points in two-dimensional search range
N_F, N_G	Number of equations for URA autocalibration with one and multiple sources
N_P, N_S	Number of pulses and fast time samples
N_ψ	Number of points in field-of-view
$p_k(\mathbf{x} \boldsymbol{\eta}_k, \sigma^2)$	pdf of \mathbf{x} given unknown parameters of k targets and noise
\mathbf{p}_m	Position of sensor element m
P	Source variance
$P_{\text{BF}}(\cdot)$	Beamformer spectrum
$P_{\text{MUSIC}}(\cdot)$	MUSIC pseudo spectrum
P_D	Probability of detection
P_{FA}	Probability of false alarm
\mathbf{P}	Source covariance matrix
\mathbf{P}_A	Projection matrix onto column span of \mathbf{A}
\mathbf{P}_A^\perp	Orthogonal projection matrix
\mathbf{P}_φ	Projection-like operator onto unidentifiable components
$q_{0,i}$	Cross beampattern value at ψ_i
$Q(\cdot)$	Cross beampattern
\mathbf{Q}	Estimator matrix for URA autocalibration with one source
\mathbf{Q}_M	Left \mathbf{J}_M -real unitary matrix
r, r_k	Range, parameter of target k
\mathbf{R}	Spatial array covariance matrix

$\tilde{\mathbf{R}}$	Perturbed covariance matrix
$\hat{\mathbf{R}}$	Sample covariance matrix
$\hat{\mathbf{R}}_{\text{FB}}$	Forward/backward averaged sample covariance matrix
s, s_k	Source waveform, parameter of target k
\mathbf{s}	Vector of source waveforms
$S(\psi)$	Windowed spatial Fourier transform
T	Pulse duration
T_D	Test statistic for multiple target detection
T_{GRLT}	Test statistic for GLRT
T_P, T_S	Pulse repetition interval and fast time sampling interval
\mathbf{u}_m	Eigenvectors of spatial covariance matrix
$\mathbf{U}_s, \mathbf{U}_n$	Signal and noise subspace
v, v_k	Relative radial velocity, parameter of target k
\mathbf{V}	Real-valued projection operator
\mathbf{v}	Nonredundant vectorization of real-valued projection operator
$\mathbf{v}_1, \mathbf{v}_2$	Eigenvectors of real-valued projection operator
w_0	Squared beampattern maximum
\mathbf{w}	Vector of normalized window coefficients
$W(\cdot)$	Beampattern
x_T, x_R, x_{IF}	Transmitted, received and IF radar signal
X_{IF}	IF radar signal after two DFTs
\mathbf{x}	Array output vector or snapshot
$\tilde{\mathbf{x}}$	Perturbed array output vector
$\mathbf{x}_k(\boldsymbol{\eta}_k)$	Signal model with k targets without noise
α	Chirp rate

α_w	Parabola parameter of squared beampattern around maximum
$\hat{\boldsymbol{\alpha}}$	Unstructure estimate of array response
β_i	Slope of cross beampattern at ψ_i
β_x, β_y	Rotational factors in x - and y -direction
$\boldsymbol{\beta}$	Vector of rotational factors
γ_D	Threshold value for multiple target detection
γ_{GLRT}	Threshold value for GLRT
δ	Angular separation parameter, see (3.11)
δ_{min}	Smallest allowed angular separation
$\boldsymbol{\delta}_x, \boldsymbol{\delta}_y$	Ramp vectors of size M_x and M_y
$\Delta\psi$	Step size of grid search
Δ_r, Δ_v	Width of processing cells according to range and relative velocity
ϵ	Phase errors of sample covariance matrix
$\boldsymbol{\epsilon}$	Vector of phase errors
$\boldsymbol{\eta}_k$	Vector of signal parameters for k targets
θ, θ_k	Elevation angle, parameter of target k
$\boldsymbol{\theta}$	Vector of elevation angles
$\hat{\boldsymbol{\vartheta}}$	Vector of phase measurements
$\hat{\boldsymbol{\vartheta}}_{\Delta}$	Vector of phase differences measurement
κ	Wavenumber
λ	Wavelength
λ_m	Eigenvalues of \mathbf{R}
$\boldsymbol{\Lambda}_s$	Diagonal matrix of signal eigenvalues
μ	Scaling parameter
ρ	Power ratio parameter, see (3.11)

ρ_{\min}	Smallest allowed power ratio
$\boldsymbol{\rho}$	Vector of DOA and phase error parameters
σ^2	Noise variance
$\hat{\sigma}_k^2$	Noise variance estimate with k targets
σ_φ^2	Variance of phase errors
τ	Radar two-way propagation delay
τ_m	Delay at sensor element m
ϕ, ϕ_k	Azimuth angle, parameter of target k
$\boldsymbol{\phi}$	Vector of azimuth angles
$\boldsymbol{\Phi}$	Phase error matrix
φ	Relative phase parameter, see (3.11)
φ_m	Phase error at sensor element m
$\boldsymbol{\varphi}$	Vector of phase errors
ψ, ψ_k	Electrical angle for ULA, parameter of target k
ψ'	Circularly shifted electrical angle
ψ_{BF}	Local maxima of BF spectrum
ψ_{M}	Midpoint between two electrical angles
ψ_x, ψ_y	Electrical angles in x - and y -direction for URA

Bibliography

- [AJM07] Y. Abramovich, B. Johnson, and X. Mestre, “Performance breakdown in MUSIC, G-MUSIC and maximum likelihood estimation,” in *Proc. of the 32nd IEEE Int. Conf. on Acoustics, Speech and Sig. Proc. (ICASSP)*, Honolulu, USA, Apr 2007.
- [AN10] N. Arkind and B. Nadler, “Parametric joint detection-estimation of the number of sources in array processing,” in *Proc. of the 6th IEEE Sensor Array and Multichannel Sig. Proc. Workshop (SAM)*, Jerusalem, Israel, Oct 2010.
- [And63] T. Anderson, “Asymptotic theory for principal component analysis,” *Ann. Math. Statist.*, vol. 34, pp. 122–148, 1963.
- [And03] —, *An Introduction to Multivariate Statistical Analysis*. Wiley and Sons, 2003.
- [Bar74] D. Barton, “Low angle radar tracking,” *Proc. of the IEEE*, vol. 62, no. 6, pp. 687–704, Jun 1974.
- [Bar83] A. Barabell, “Improving the resolution performance of eigenstructure-based direction-finding algorithms,” in *Proc. of the 8th IEEE Int. Conf. on Acoustics, Speech and Sig. Proc. (ICASSP)*, Boston, USA, Apr 1983.
- [BM86] Y. Bresler and A. Macovski, “Exact maximum likelihood parameter estimation of superimposed exponential signals in noise,” *IEEE Trans. Acoustics, Speech and Sig. Proc.*, vol. 34, no. 5, pp. 1081–1089, Oct 1986.
- [Büh08] M. Bühren, “Simulation und Verarbeitung von Radarziellisten im Automobil,” Ph.D. dissertation, Universität Stuttgart, 2008.
- [BY06] M. Bühren and B. Yang, “Automotive radar target list simulation based on reflection center representation of objects,” in *Workshop on Intelligent Transportation*, Hamburg, Germany, Mar 2006, pp. 161–166.
- [BY07] —, “Extension of automotive radar target list simulation to consider further physical aspects,” in *Int. Conf. on Telecommunications (ITS)*, Sophia Antipolis, France, Aug 2007, pp. 1–6.
- [CT65] J. Cooley and J. Tukey, “An algorithm for the machine calculation of the complex Fourier series,” *Math. Comp.*, vol. 19, pp. 297–301, 1965.
- [Dem97] J. Demmel, *Applied numerical linear algebra*. SIAM, 1997.
- [DHRD07] J. DaCosta, M. Haardt, F. Roemer, and G. DelGaldo, “Enhanced model order estimation using higher-order arrays,” in *Proc. of the 41st Asimolar Conf. on Signals, Systems and Computers (ACSSC)*, Pacific Grove, Canada, Nov 2007.

- [Eng11] F. Engels, “Target shape estimation using an automotive radar,” in *Proc. of the 5th Biennial on DSP for In-Vehicle Systems*, Kiel, Germany, Sep 2011.
- [Eri01] J. Eriksson, “Multiple signal detection under a specified false alarm constraint,” in *Proc. of the 26th IEEE Int. Conf. on Acoustics, Speech and Sig. Proc. (ICASSP)*, Salt Lake City, USA, May 2001.
- [Fri90] B. Friedlander, “A sensitivity analysis of the MUSIC algorithm,” *IEEE Trans. Acoustics, Speech and Sig. Proc.*, vol. 38, no. 10, pp. 1740–1751, Oct 1990.
- [FW88] B. Friedlander and A. Weiss, “Eigenstructure methods for direction finding with sensor gain and phase uncertainties,” in *Proc. of the 13th IEEE Int. Conf. on Acoustics, Speech and Sig. Proc. (ICASSP)*, New York, USA, Apr 1988.
- [GLC96] J. Grouffaud, P. Larzabal, and H. Clergeot, “Some properties of ordered eigenvalues of a Wishart matrix: Application in detection test and model order selection,” in *Proc. of the 21st IEEE Int. Conf. on Acoustics, Speech and Sig. Proc. (ICASSP)*, Atlanta, USA, May 1996.
- [GM98] J. Goldberg and H. Messer, “Inherent limitations in the localization of a coherently scattered source,” *IEEE Trans. Signal Processing*, vol. 46, no. 12, pp. 3441–3444, Dec 1998.
- [GNB97] A. Gershman, U. Nickel, and J. Böhme, “Adaptive beamforming algorithms with robustness against jammer motion,” *IEEE Trans. Signal Processing*, vol. 45, no. 7, pp. 1878–1885, Jul 1997.
- [God97] L. Godara, “Application of antenna arrays to mobile communications: Part II – Beamforming and direction-of-arrival considerations,” *Proc. of the IEEE*, vol. 85, no. 8, pp. 1195–1245, Aug 1997.
- [GP03] G. Golub and V. Pereyra, “Separable nonlinear least squares: The variable projection method and its applications,” *Inverses Prob.*, vol. 19, no. 2, pp. R1–R26, 2003.
- [GSDB07] J. Gunnarsson, L. Svensson, L. Danielsson, and F. Bengtsson, “Tracking vehicles using radar detections,” in *IEEE Intelligent Vehicles Symposium*, Istanbul, Turkey, Jun 2007, pp. 296–302.
- [Gus09] F. Gustafsson, “Automotive safety systems,” *IEEE Signal Processing Magazine*, vol. 26, no. 4, pp. 32–47, Jul 2009.
- [GvL96] G. Golub and C. van Loan, *Matrix Computations*. The Johns Hopkins University Press, 1996.
- [Har78] F. Harris, “On the use of windows for harmonic analysis with the discrete Fourier transform,” *Proc. of the IEEE*, vol. 66, no. 1, pp. 51–83, Jan 1978.
- [Hay07] S. Haykin, *Adaptive Radar Signal Processing*. Wiley and Sons, 2007.

- [HBTA11] J. Hansen, P. Boyraz, K. Takeda, and H. Abut, *Digital Signal Processing for In-Vehicle Systems and Safety*. Springer, 2011.
- [HN95] M. Haardt and J. Nossék, “Unitary ESPRIT: How to obtain increased estimation accuracy with a reduced computational burden,” *IEEE Trans. Signal Processing*, vol. 43, no. 5, pp. 1232–1242, May 1995.
- [Hof08] J. Hoffmann, “Das Darmstädter Verfahren (EVITA) zum Testen und Bewerten von Frontalkollisionsgegenmaßnahmen,” Ph.D. dissertation, Technische Universität Darmstadt, 2008.
- [How99] R. Howell, “d-MUSIC: A real time algorithm for estimating the DOA of coherent sources using a single array snapshot,” in *Proc. of the 24th IEEE Int. Conf. on Acoustics, Speech and Sig. Proc. (ICASSP)*, Phoenix, USA, Mar 1999.
- [HSZ10] P. Heidenreich, D. Stenmanns, and A. Zoubir, “Computationally simple criteria for detecting a multi-target scenario in automotive radar array processing,” in *Proc. of the European Signal Processing Conf. (EUSIPCO)*, Aalborg, Denmark, Aug 2010.
- [HY10] P. Häcker and B. Yang, “Single snapshot DOA estimation,” *Adv. Radio Sci.*, vol. 8, pp. 251–256, 2010.
- [HY11a] —, “Analytical investigation of two-object DOA estimation,” in *Proc. of the Int. ITG Workshop on Smart Antennas (WSA)*, Aachen, Germany, Feb 2011.
- [HY11b] —, “Mixed-order and higher-order ambiguity functions,” in *Proc. of the IEEE Intelligent Vehicles Symposium*, Baden-Baden, Germany, Jun 2011.
- [HZ11a] P. Heidenreich and A. Zoubir, “Computational aspects of maximum likelihood DOA estimation of two targets with applications to automotive radar,” in *Proc. of the 5th Biennial on DSP for In-Vehicle Systems*, Kiel, Germany, Sep 2011.
- [HZ11b] —, “Gain and phase autocalibration for uniform rectangular arrays,” in *Proc. of the 36th IEEE Int. Conf. on Acoustics, Speech and Sig. Proc. (ICASSP)*, Prague, Czech Republic, May 2011.
- [HZ12] —, “Computationally simple DOA estimation of two resolved targets with a single snapshot,” in *Proc. of the 37th IEEE Int. Conf. on Acoustics, Speech and Sig. Proc. (ICASSP)*, Kyoto, Japan, Mar 2012.
- [ISO09] ISO TC204/WG14, “ISO 22179 Intelligent transport systems – Full speed range adaptive cruise control (FSRA) systems – Performance requirements and test procedures,” 2009.
- [JD93] D. Johnson and D. Dudgeon, *Array Signal Processing: Concepts and Techniques*. Prentice-Hall, 1993.

- [Jon01] W. Jones, "Keeping cars from crashing," *IEEE Spectrum*, vol. 38, no. 9, pp. 40–45, Sep 2001.
- [JSO98] M. Jansson, A. Swindlehurst, and B. Ottersten, "Weighted subspace fitting for general array error model," *IEEE Trans. Signal Processing*, vol. 46, no. 9, pp. 2484–2498, May 1998.
- [KN09] S. Kritchman and B. Nadler, "Non-parametric detection of the number of signals: Hypothesis testing and random matrix theory," *IEEE Trans. Signal Processing*, vol. 57, no. 10, pp. 3930–3941, Oct 2009.
- [KV96] H. Krim and M. Viberg, "Two decades of array signal processing research," *IEEE Signal Processing Magazine*, vol. 13, no. 4, pp. 67–94, Jul 1996.
- [LE06] Y. Li and M. Er, "Theoretical analyses of gain and phase error calibration with optimal implementation for linear equispaced array," *IEEE Trans. Signal Processing*, vol. 54, no. 2, pp. 712–723, Jan 2006.
- [Lee80] A. Lee, "Centrohermitian and skew-centrohermitian matrices," *Linear Algebra and its Applications*, vol. 29, pp. 205–210, 1980.
- [LKK04] M.-S. Lee, V. Katkovnik, and Y.-H. Kim, "System modeling and signal processing for a switch antenna array radar," *IEEE Trans. Signal Processing*, vol. 52, no. 6, pp. 1513–1523, Jun 2004.
- [LL91] T. Lo and J. Litva, "Low-angle tracking using multifrequency sampled aperture radar," *IEEE Trans. Aerospace and Electronic Systems*, vol. 27, no. 5, pp. 797–805, Sep 1991.
- [LLV06] M. Lanne, A. Lundgren, and M. Viberg, "Calibrating an array with scan dependent errors using a sparse grid," in *Proc. of the 40th Asimolar Conf. on Signals, Systems and Computers (ACSSC)*, Pacific Grove, Canada, Nov 2006.
- [LS96] J. Li and P. Stoica, "Efficient mixed-spectrum estimation with applications to target feature extraction," *IEEE Trans. Signal Processing*, vol. 44, no. 2, pp. 281–295, Feb 1996.
- [LZS97] J. Li, D. Zheng, and P. Stoica, "Angle and waveform estimation via RELAX," *IEEE Trans. Aerospace and Electronic Systems*, vol. 33, no. 3, pp. 1077–1087, Jul 1997.
- [MWGH98] C. Mecklenbräuker, A. Waldhorst, P. Gerstoft, and G. Harabalus, "Matched field processing using multipole expansion," in *Proc. of the 4th European Conference on Underwater Acoustics (ECUA)*, Rome, Italy, Sep 1998.
- [NS96] B. Ng and C. See, "Sensor-array calibration using a maximum-likelihood approach," *IEEE Trans. Antennas Propagation*, vol. 44, no. 6, pp. 827–835, Jun 1996.

- [NWAH09] P. Noorishad, S. Wijnholds, A. v. Ardenne, and J. v. d. Hulst, “Applicability of redundancy calibration to dense phased arrays,” in *Proc. of the Conf. on Wide Field Science and Technology for the Square Kilometer Array*, Limelette, Belgium, Nov 2009.
- [OVSN93] B. Ottersten, M. Viberg, P. Stoica, and A. Nehorai, “Exact and large sample ML techniques for parameter estimation and detection in array processing,” in *Radar Array Processing*. Springer-Verlag, 1993.
- [PGH00] M. Pesavento, A. Gershman, and M. Haardt, “Unitary root-MUSIC with a real-valued eigendecomposition: A theoretical and experimental performance study,” *IEEE Trans. Signal Processing*, vol. 49, no. 5, pp. 1306–1314, May 2000.
- [PK85] A. Paulraj and T. Kailath, “Direction of arrival estimation by eigenstructure methods with unknown sensor gain and phase,” in *Proc. of the 10th IEEE Int. Conf. on Acoustics, Speech and Sig. Proc. (ICASSP)*, Tampa, USA, Apr 1985.
- [PK89] S. Pillai and B. Kwon, “Forward/backward spatial smoothing techniques for coherent signal identification,” *IEEE Trans. Acoustics, Speech and Sig. Proc.*, vol. 37, no. 1, pp. 8–15, Jan 1989.
- [PK91] J. Pierre and M. Kaveh, “Experimental performance of calibration and direction-finding algorithms,” in *Proc. of the 16th IEEE Int. Conf. on Acoustics, Speech and Sig. Proc. (ICASSP)*, Toronto, Canada, Apr 1991.
- [Rao73] C. Rao, *Linear Statistical Inference and Its Applications*. Wiley Series in Probability and Statistics, 1973.
- [RB97] B. Radich and K. Buckley, “Single-snapshot DOA estimation and source number detection,” *IEEE Signal Processing Letters*, vol. 4, no. 4, pp. 109–111, Apr 1997.
- [RGB00] J. Ringelstein, A. Gershman, and J. Böhme, “Direction finding in random inhomogeneous media in the presence of multiplicative noise,” *IEEE Signal Processing Letters*, vol. 7, no. 10, pp. 269–272, Oct 2000.
- [Ric05] M. Richards, *Fundamentals of Radar Signal Processing*. McGraw-Hill, 2005.
- [RK89] R. Roy and T. Kailath, “ESPRIT – Estimation of signal parameters via rotational invariance techniques,” *IEEE Trans. Acoustics, Speech and Sig. Proc.*, vol. 37, no. 7, pp. 984–955, Jul 1989.
- [RMS88] Y. Rockah, H. Messer, and P. Schultheiss, “Localization performance of arrays subject to phase errors,” *IEEE Trans. Aerospace and Electronic Systems*, vol. 24, no. 4, pp. 402–410, Jul 1988.
- [Roh83] H. Rohling, “Radar CFAR thresholding in clutter and multiple target situations,” *IEEE Trans. Aerospace and Electronic Systems*, vol. 19, no. 4, pp. 608–621, Jul 1983.

- [RSH10] M. Richards, J. Scheer, and W. Holm, *Principles of Modern Radar: Basic Principles*. SciTech Publishing, Inc., 2010.
- [Sch98] A. Schuster, "On the investigation of hidden periodicities with application to a supposed 26 day period of meteorological phenomena," *Terr. Magn.*, vol. 3, no. 1, pp. 13–41, Mar 1898.
- [Sch86] R. Schmidt, "Multiple emitter location and signal parameter estimation," *IEEE Trans. Antennas Propagation*, vol. 34, no. 3, pp. 276–280, Jan 1986.
- [Sch10] M. Schoor, "Hochauflösende Winkelschätzung für automobile Radarsysteme," Ph.D. dissertation, Universität Stuttgart, 2010.
- [SK92] A. Swindlehurst and T. Kailath, "A performance analysis of subspace-based methods in the presence of model errors: Part I – The MUSIC algorithm," *IEEE Trans. Signal Processing*, vol. 40, no. 7, pp. 1758–1774, Jul 1992.
- [SK93] —, "A performance analysis of subspace-based methods in the presence of model errors: Part II – Multidimensional algorithms," *IEEE Trans. Signal Processing*, vol. 41, no. 9, pp. 2882–2890, Sep 1993.
- [Sko08] M. Skolnik, *Radar Handbook*. McGraw-Hill, 2008.
- [SL00] Y. Sng and Y. Li, "Fast algorithm for gain and phase error calibration of linear equi-spaced (LES) array," in *Proc. of the 5th IEEE Int. Conf. on Signal Processing*, Beijing, China, Aug 2000.
- [SM97] P. Stoica and R. Moses, *Introduction to Spectral Analysis*. Prentice-Hall, 1997.
- [Smi05] S. Smith, "Statistical resolution limits and the complexified Cramér-Rao bound," *IEEE Trans. Signal Processing*, vol. 53, no. 5, pp. 1597–1609, May 2005.
- [SN88] P. Stoica and A. Nehorai, "Statistical analysis of two non-linear least-squares estimators of sine waves parameters in the colored noise case," Apr 1988.
- [SN89] —, "MUSIC, maximum likelihood, and the Cramér-Rao bound," *IEEE Trans. Acoustics, Speech and Sig. Proc.*, vol. 37, no. 5, pp. 720–741, May 1989.
- [Sva99] T. Svantesson, "Modeling and estimation of mutual coupling in a uniform linear array of dipoles," in *Proc. of the 24th IEEE Int. Conf. on Acoustics, Speech and Sig. Proc. (ICASSP)*, Phoenix, USA, Mar 1999.
- [TF09] T. Tuncer and B. Friedlander, *Classical and Modern Direction-of-Arrival Estimation*. Academic Press, 2009.
- [THG09] A. Thakre, M. Haardt, and K. Giridhar, "Single snapshot spatial smoothing with improved effective array aperture," *IEEE Signal Processing Letters*, vol. 16, no. 6, pp. 505–508, Jun 2009.

- [Tre85] S. Treter, “Estimating the frequency of a noisy sinusoid by linear regression,” *IEEE Trans. Information Theory*, vol. 31, no. 6, pp. 832–835, Nov 1985.
- [VS94] M. Viberg and A. Swindlehurst, “A Bayesian approach to auto-calibration for parametric array signal processing,” *IEEE Trans. Signal Processing*, vol. 42, no. 12, pp. 3495–3507, Dec 1994.
- [vT68] H. van Trees, *Detection, Estimation and Modulation Theory – Part I*. Wiley and Sons, 1968.
- [vT02] ———, *Detection, Estimation, and Modulation Theory – Part IV Optimum Array Processing*. Wiley and Sons, 2002.
- [WF94] A. Weiss and B. Friedlander, “Preprocessing for direction finding with minimal variance degradation,” *IEEE Trans. Signal Processing*, vol. 42, no. 6, pp. 1478–1485, Aug 1994.
- [WHW09] H. Winner, S. Hakuli, and G. Wolf, *Advanced Driver Assistance Systems Handbook (in German: Handbuch Fahrerassistenzsysteme: Grundlagen, Komponenten und Systeme für aktive Sicherheit und Komfort)*. Vieweg+Teubner, 2009.
- [Win06] M. Wintermantel, “New approach for an approximate realization of rank order filtering with low complexity,” *Frequenz Journal of RF-Engineering and Telecommunications*, vol. 60, no. 1-2, pp. 24–28, Feb 2006.
- [Win07] V. Winkler, “Range Doppler detection for automotive FMCW radars,” in *Proc. of the 4th European Radar Conf.*, Munich, Germany, Oct 2007.
- [Win10] M. Wintermantel, “Radar system with improved angle formation,” German Patent Application WO 2010/000 252, 2010.
- [WJ90] D. Williams and D. Johnson, “Using the sphericity test for source detection with narrow-band passive arrays,” *IEEE Trans. Acoustics, Speech and Sig. Proc.*, vol. 38, no. 11, pp. 2008–2014, Nov 1990.
- [WK85] M. Wax and T. Kailath, “Detection of signals by information theoretic criteria,” *IEEE Trans. Acoustics, Speech and Sig. Proc.*, vol. 33, no. 2, pp. 387–392, Apr 1985.
- [WLO⁺11] J. Withopf, C. Lüke, H. Özer, G. Schmidt, and A. Theiß, “Signal processing for in-car communication systems,” in *Proc. of the 5th Biennial on DSP for In-Vehicle Systems*, Kiel, Germany, Sep 2011.
- [WOV91] B. Wahlberg, B. Ottersten, and M. Viberg, “Robust signal parameter estimation in the presence of array perturbations,” in *Proc. of the 16th IEEE Int. Conf. on Acoustics, Speech and Sig. Proc. (ICASSP)*, Toronto, Canada, Apr 1991.

- [WRM94] M. Wylie, S. Roy, and H. Messer, "Joint DOA estimation and phase calibration of linear equispaced (LES) arrays," *IEEE Trans. Signal Processing*, vol. 42, no. 12, pp. 3449–3459, Dec 1994.
- [WSG⁺07] P. Wenig, M. Schoor, O. Gunther, B. Yang, and R. Weigel, "System design of a 77 GHz automotive radar sensor with superresolution DOA estimation," in *Proc. of the Int. Symp. on Signals, Systems and Electronics*, Montreal, Canada, Jul 2007.
- [WTNV10] S. Wijnholds, S. v. d. Tol, R. Nijboer, and A.-J. v. d. Veen, "Calibration challenges for future radio telescopes," *IEEE Signal Processing Magazine*, vol. 27, no. 1, pp. 30–42, Jan 2010.
- [XK94] G. Xu and T. Kailath, "Fast subspace decomposition," *IEEE Trans. Signal Processing*, vol. 42, no. 3, pp. 539–551, Mar 1994.
- [XRK94] G. Xu, R. Roy, and T. Kailath, "Detection of number of sources via exploitation of centro-symmetry property," *IEEE Trans. Signal Processing*, vol. 42, no. 1, pp. 102–112, Jan 1994.
- [ZB95] A. Zoubir and J. Böhme, "Bootstrap multiple tests applied to sensor location," *IEEE Trans. Acoustics, Speech and Sig. Proc.*, vol. 43, no. 6, pp. 1386–1396, Jun 1995.
- [ZI07] A. Zoubir and R. Iskander, "Bootstrap methods and applications," *IEEE Signal Processing Magazine*, vol. 24, no. 4, pp. 10–19, Jul 2007.
- [ZL91] M. Zoltowski and T.-S. Lee, "Maximum likelihood based sensor array signal processing in the beamspace domain for low angle radar tracking," *IEEE Trans. Acoustics, Speech and Sig. Proc.*, vol. 39, no. 3, pp. 656–671, Mar 1991.
- [Zol92] M. Zoltowski, "Beamspace ML bearing estimation for adaptive phased array radar," in *Adaptive Radar Detection and Estimation*. Wiley and Sons, 1992.
- [ZW88a] J. Zhu and H. Wang, "Effects of sensor position and pattern perturbations on CRLB for direction finding of multiple narrowband sources," in *Proc. of the 4th ASSP Workshop on Spectrum Estimation and Modeling*, Minneapolis, USA, Aug 1988.
- [ZW88b] I. Ziskind and M. Wax, "Maximum likelihood localization of multiple sources by alternating projection," *IEEE Trans. Acoustics, Speech and Sig. Proc.*, vol. 36, no. 10, pp. 1553–1560, Oct 1988.

Curriculum vitae

Name: Philipp Heidenreich
 Email: ph.heidenreich@web.de
 Date, place of birth: 27.12.1980, Rüsselsheim
 Family status: married

Education

10/2001 – 12/2006 Technische Universität Darmstadt
 Electrical Engineering and Information Technology
 Dipl.-Ing. with grade *sehr gut* (1.6)
 Diploma thesis: “Image processing for time-frequency
 signature extraction with application to direction-finding”

09/2005 – 02/2006 Exchange studies at Heriot-Watt University, Edinburgh, UK
 Study thesis: “Time-frequency analysis of biosonar
 signals of the bottlenose dolphin”

07/1991 – 05/2000 Max-Planck-Gymnasium Rüsselsheim
 Abitur with grade *gut* (1.9)
 Specialized courses in mathematics and physics

Work experience

Since 03/2007 Technische Universität Darmstadt
 Research associate at Signal Processing Group
 Focus on statistical signal processing and array processing

03/2006 – 06/2006 Internship, Panasonic R&D Center Germany, Langen

07/2001 – 09/2001 Internship, Adam Opel AG, Rüsselsheim

08/2000 – 06/2001 Civilian Service (*Zivildienst*), Hospital Rüsselsheim

Erklärung laut §9 der Promotionsordnung

Ich versichere hiermit, dass ich die vorliegende Dissertation allein und nur unter Verwendung der angegebenen Literatur verfasst habe. Die Arbeit hat bisher noch nicht zu Prüfungszwecken gedient.

Darmstadt, 29.02.2012

